

ALMA MATER STUDIORUM - UNIVERSITÀ DI BOLOGNA

DOTTORATO DI RICERCA IN
Meccanica e Scienze Avanzate dell'Ingegneria
Ciclo XXVIII

Settore concorsuale di afferenza: 09/A1 - Ingegneria aeronautica, aerospaziale e navale

Settore scientifico disciplinare: ING-IND/04 - Costruzioni e strutture aerospaziali

TITOLO TESI

**Fatigue and Damage Tolerance
in Primary Composite Aeronautical Structures**

Presentata da: Vjola RISTORI

Coordinatore Dottorato

Prof. Nicolò Cavina

Relatore

Prof. Enrico Troiani

ESAME FINALE ANNO 2017

You know why...

Contents

Contents	iii
List of Figures	vi
List of Tables	x
Acknowledgments	xii
Abstract	xiii
1 Introduction	1
1.1 Research Motivation	2
1.2 State of the art	2
2 Damage Tolerance in Composite Aeronautical Structures	6
2.1 Background	7
2.2 Airworthiness Regulations	10
2.3 Damage Tolerance in composite aeronautical structures	12
2.3.1 Damage Threat Assessment	14
2.3.2 Damage detectability	16
2.3.3 Fatigue Tests and Analyses	17

3	Experimental analysis	19
3.1	First Experimental Campaign - calibration	20
3.1.1	Specimens Preparation	20
3.1.2	Near Edge Impacts	21
3.1.3	Experimental results	23
3.1.4	Accelerometer measurement of impact events	24
3.1.5	Compression After Impact Tests	29
3.2	Second Experimental Campaign	38
3.2.1	Specimens Preparation	38
3.2.2	Near Edge Impacts	40
3.2.3	Compression After Impact Tests	41
3.2.4	Experimental results	41
4	Modelling Failure in Composite Structures	47
4.1	Failure Models of Composite Structures	48
4.1.1	Maximum Stress Failure Model	50
4.1.2	Maximum Strain Failure Model	51
4.1.3	Tsai-Hill Failure Model	52
4.1.4	Tsai-Wu Failure Model	53
4.1.5	Puck Failure Model	53
4.1.6	Hashim-Rotem Failure Model	53
5	Setup of Numerical Analysis using Abaqus Explicit	57
5.1	Model Setup	58
5.1.1	Model Geometry	58
5.1.2	Model Materials and Properties	58
5.1.3	Building of the Laminate	59
5.1.4	Meshing of the Model	60
5.1.5	Boundary Conditions and Loads	61
5.2	Modelling of Composite Laminates	62
5.3	Modelling of Cohesive Elements	66
5.4	Modelling of Damage and Failure of fiber-reinforced materials	75
5.5	Running of the Analysis	82

6 Numerical Results	83
6.1 Numerical output	85
6.1.1 Impact energy level	85
6.1.2 Delamination	88
6.2 Delamination size	90
6.3 Correlation of experimental and numerical delaminations . .	94
6.3.1 Surface Indentation	97
6.3.2 Depth estimation of the surface indentation	101
7 Conclusions	104
Bibliography	106
Publications List	113

List of Figures

1.1	Three types of edge impacts, a) on edge impact, b) oblique impact, c) near-edge impact; adapted from [6]	5
2.1	Evolution of the composite presence on commercial aircraft	7
2.2	B787 materials breakdown per weight, source Boeing	8
2.3	A350 XWB materials breakdown per weight, source Airbus	9
2.4	Fatigue behaviour of composite vs. metallic materials	10
2.5	Residual strength of composite vs. metallic material under fatigue or impact loading	13
2.6	Load Levels versus Damage Sizes, from [15]	15
2.7	Percentage of impacts on different zones of an aircraft, from [16]	16
2.8	Defects Detectability versus Energy Level Probability, from [17]	17
2.9	Typical test pyramid	18
3.1	Introducing near edge impacts in CFRP specimens	20
3.2	Used Charpy pendulum	21
3.3	Charpy Pendulum Impacting Element	22
3.4	Counterweight element used to balance the pendulum staff .	22
3.5	Balanced staff	23

List of Figures

3.6	Goniometer used to determine the spring back angle of the pendulum	24
3.7	Fixing rig used for the impact tests	24
3.8	Specimen after near edge impact, 3J	25
3.9	Specimen after near edge impact, 5J	25
3.10	Specimen after near edge impact, 12J	26
3.11	Specimen after near edge impact, 12J	27
3.12	Schematic representation of a typical impact damage mode for composite laminate [22]	27
3.13	Triaxial accelerometer fixed to the impacting element	28
3.14	Typical acceleration-time diagram in z-axis direction	28
3.15	Acceleration-time diagram in z-axis direction, 4J	29
3.16	Acceleration-time diagram in z-axis direction, 5J	29
3.17	Acceleration-time diagram in z-axis direction, 6J	29
3.18	Acceleration-time diagram in z-axis direction, 7J	30
3.19	Displacement-time diagram in y-axis direction, 4J	30
3.20	Displacement-time diagram in y-axis direction, 5J	30
3.21	Displacement-time diagram in y-axis direction, 6J	31
3.22	Displacement-time diagram in y-axis direction, 7J	31
3.23	CAI testing rig, 3D visualisation	34
3.24	CAI testing rig with specimen mounted inside	35
3.25	Undesired failure mode close to the extremity of the specimen	35
3.26	Specimen mounted in the testing rig, standard [25]	36
3.27	Completely mounted testing rig, standard [25]	36
3.28	Failure of a specimen after the CAI test	38
3.29	CFRP specimens cut from the laminated plate	39
3.30	Impacting element	40
3.31	Fixing mechanism (left) and with the specimen mounted (right)	41
3.32	Specimen mounted in the CLC fixing	42
3.33	Hydraulic press machine, left and with the CLC fixing mounted, right	43
3.34	Visual inspection of the specimens after impact, typical surface condition	45

List of Figures

4.1	Lamina failure criteria by frequency of usage	50
4.2	Ply (left) and laminate (right) coordinate systems	51
4.3	Representation of three different fracture modes: A, B and C, from [39]	54
4.4	Failure envelopes and test data in Compression - Shear plane, for T800/3900-2 composite, from [35] and [42]	55
4.5	Failure modes of unidirectional composite under plane stress, from [43]	56
5.1	Assembly of the laminate in Abaqus	59
5.2	Contact property - tangential behaviour definition in Abaqus	60
5.3	Specimen in impact test rig (left); FEM representation of the specimen (right)	61
5.4	Definition of the elastic properties of the laminate in Abaqus	65
5.5	Spatial representation of a 3D cohesive element, reported from [44]	67
5.6	Deformation modes of a cohesive element, reported from [44]	67
5.7	Typical traction-separation response, reported from [44] . .	70
5.8	Illustration of mixed-mode response in cohesive elements, reported from [44]	72
5.9	Input definition for Quadratic nominal stress damage crite- rion in Abaqus	75
5.10	Definition of damage evolution in cohesive elements in Abaqus using BK criterion	76
5.11	Equivalent stress versus equivalent displacement, reported from [44]	80
5.12	Definition of Hashin damage initiation criterion in Abaqus .	82
6.1	Comparison between Abaqus numerical and experimental results	86
6.2	Maximum contact force between the impactor and the laminate	87
6.3	Impact force vs. time for numerical and experimental analysis	88
6.4	Displacement plot in impacting direction	89

List of Figures

6.5	Delaminations results - top [47]: a) - experimental x-ray radiograph, b) numerical; bottom: obtained using the current model	89
6.6	Delamination area central impact - 5J vs. 3J	91
6.7	Delamination area near edge impact - 5J vs. 3J	92
6.8	Delamination area 3J - near edge vs. central impact	92
6.9	Delamination area 5J - near edge vs. central impact	92
6.10	Delamination area 3J central impact - 4 sides vs. 3 sides blocked	93
6.11	Delamination area 5J central impact - 4 sides vs. 3 sides blocked	93
6.12	3J - RSR reduction versus induced delamination size	96
6.13	5J - RSR reduction versus induced delamination size	97
6.14	Matrix tension damage initiation criterion - 3J near edge impact	98
6.15	Matrix tension damage initiation criterion - 3J central impact	98
6.16	Matrix tension damage initiation criterion - 5J near edge impact	99
6.17	Matrix tension damage initiation criterion - 5J central impact	99
6.18	Numerically predicted damage from [47] in the form of matrix tensile failure, (a, c and e) and non-linear shear damage, (b, d and f) for different impact energies	101

List of Tables

3.1	Accelerometer data for different energy levels	32
3.2	Specimens division - calibration testing campaign	32
3.3	Overview of nominal energies, initial and spring-back angles on different specimen groups	33
3.4	Overview of applied energies on different specimen groups . .	34
3.5	Overview of applied forces at failure for different specimen groups	37
3.6	Specimens division	39
3.7	Overview of applied energies on different specimen groups . .	44
3.8	Maximum applied force at failure for different specimen groups	46
5.1	Overview of defined material and section properties in Abaqus	58
5.2	Mesh attributes overview	61
5.3	Mechanical properties of the modelled laminate, assumed $V_f=50\%$	64
5.4	Mechanical properties of carbon fiber/epoxy laminates from the literature, part 1	64
5.5	Mechanical properties of carbon fiber/epoxy laminates from the literature, part 2	65
5.6	Material parameters of the cohesive elements	74

List of Tables

6.1	Delamination area for 5J impact for each lamina interface, near edge vs. central	90
6.2	Delamination area for 3J impact for each lamina interface, near edge vs. central	91
6.3	Average delamination area for different energy levels and impact positions	91
6.4	Comparison of numerical and experimental results	94
6.5	Comparison of numerical results, 3J impact case	95
6.6	Comparison of numerical results, 5J impact case	96
6.7	Average experimental indentation size	100
6.8	Comparison of numerical and experimental dent size measure- ment	100
6.9	Input data for evaluation of indentation depth	102

Acknowledgments

First of all I want to thank Professor Troiani who has given me the opportunity to continue my education with this PhD project. A special thank to Maria Pia Falaschetti, my colleague for this experience who has given me the support on site I needed and without whom this work would not have been the same.

To my parents, for believing in me no matter what, for raising me the way that I am today and for helping me achieving any goal I set my mind to... thank you!

A special and deep thank to my children who have suffered (more or less) in silence all the sacrificed holidays, weekends and evenings during which I had to work, they have been my strength through this project and I hope that one day when they will be able to appreciate it, they will understand.

Last, but not least, I want to thank my husband! He is the one to whom this thesis is dedicated. My partner in life and at work, he has supported and encouraged me during the whole PhD experience, he has patiently been next to me the entire time during my work and he has shared with me all the joys and despairs that working on this thesis has provided me... thank you!!!

Abstract

The challenging requirements set on new full composite aeronautical structures are mostly related to the demonstration of damage tolerance capability of their primary structures, required by the airworthiness bodies. And while composite-made structures inherently demonstrate exceptional fatigue properties, when put in real life working conditions, a number of external factors can lead to impact damages thus reducing drastically their fatigue resistance due to fiber delamination, disbonding or breaking.

This PhD aims towards contributing to the better understanding of the behavior of the primary composite aeronautical structure after near-edge impacts which are inevitable during the service life of an aircraft. The behavior of CFRP structures after impacts is only one small piece of the big picture which is the certification of CFRP built aircraft, where several other parameters need to be evaluated in order to fulfill the airworthiness requirements. These parameters are also discussed in this PhD thesis in order to give a better understanding of the complex task of CFRP structure certification, in which behaviour of the impacted structure plays an important role.

By the time the current research activity started in 2012/2013, only few papers existed in the open literature that dealt explicitly with this subject and most of them were referring to glass fibers only. One year after the start of the current research program, other papers relative to on-edge impacts in CFRP structures were started to be published. It only confirms that colleagues from other research institutions independently recognized the

necessity of further investigation of edge and near-edge impacts in CFRP structures.

By the time the current research activity started, when it comes to near-edge impacts, no dedicated CFRP related models existed, leaving lots of room for improvements of the models treating the edge impacts in CFRP structures. Besides the results given in the literature that can confirm the importance of a further research in the area of edge impacts in CFRP structures, the author's work for the aerospace industry has allowed her to have an insight on the challenges manufacturers are facing with demonstrating the damage tolerant capabilities of primary composite structure and to confirm that her research efforts are indeed in line with the current needs of the industry.

An experimental and numerical campaign was carried out in order to determine the level of delamination damage in CFRP specimens after near-edge impacts. By calibrating the numerical model with experimental data, it was possible, for different configurations and energy levels, to predict the extension of a delamination in a CFRP structure and to estimate its residual static strength using a very simple but robust technique. The original contribution of this work to the analysis of CFRP structures is the creation of a model which could be applicable to wide range of thicknesses and stacking sequences of CFRP structures, thus potentially being suitable for industrial application, as well.

CHAPTER 1

Introduction

In this chapter, motivations for carrying out a research activity related to damage tolerance in composite aeronautical structures are given, explaining why is there still necessity for better understanding of the behaviour of primary composite aeronautical structures once subjected to edge impacts.

1.1 Research Motivation

The challenging requirements set on new full composite aeronautical structures are mostly related to the demonstration of damage tolerance capability of their primary structures, required by the airworthiness bodies [1], [2]. And while composite-made structures inherently demonstrate exceptional fatigue properties, when put in real life working conditions, a number of external factors can lead to impact damages thus reducing drastically their fatigue resistance due to fibre delamination, disbonding or breaking.

The current work aims towards contributing to the better understanding of the behaviour of the primary composite aeronautical structure after edge impacts which are inevitable during the service life of an aircraft.

Industrial practice has determined that edge impacts in CFRP structures can be particularly critical, presented in [3]. These impacts can occur in the cut-out area of an aircraft structure, such as passenger or cargo doors, as well as windows area. Impact events during single part manufacturing, assembly or in-service operation are simply inevitable and it is extremely important to be able to predict and assess the extent of a damage that such an event introduces in the structure. In fact, airworthiness regulations explicitly prescribe how these events must be addressed, and this is discussed in more detail in Chapter 2.

1.2 State of the art

An extensive literature overview has been carried out in order to determine the state of the art in the CFRP Damage Tolerance, focusing on the edge impact problem. By the time the current research activity started, only few papers existed in the open literature that dealt explicitly with this subject and most of them were referring to glass fibres only.

Though many examples of experimental and numerical analyses of transverse impacts exist in literature, very few can be found regarding edge impacts [4]-[6]. The research presented in these articles has been mostly driven by the arrival of full composite large civil aircraft, which necessitated additional studies of impacts, both in thick as well as thin-walled structures.

In [4], it is shown that edge impacts can indeed be more critical in respect to impacts in lamination plane and therefore deserve further investigation. Thick CFRP specimens were investigated, with specimen thickness of 4, 8 and 12 mm, and the impact energies considered were of order of magnitude of hundreds of Joules. It is reported that this energy level represents a typical accidental impact to the wing skin of a large civil aircraft. Bigger delamination area was measured for the case of near edge impact, as well as reduction of compressive strength in the laminate, in respect to the case of central transversal impact. For general definition of different types of impacts, see Figure 1.1).

Paper [5] investigates the on-edge impacts in CFRP specimens and presents an analytical model for evaluation of these impacts and prediction of static strength of impacted specimens, comparing it with experimental tests. In this work, it is mentioned that Barely Visible Impact Damage (BVID) can occur when laminated composite material is subject to edge impact loads in the plane of the laminate and can result in a significant reduction in compressive strength caused by buckle-driven delamination. It is interesting to observe that, according to airworthiness regulations, the presence of a BVID inside a primary aircraft structure must not cause the reduction of the residual strength of the laminate below ultimate load carrying capability (also discussed in more detail in Chapter 2). The challenge which is present with sizing of composite structures that need to satisfy damage tolerance requirements is also mentioned, specially referring to stiffeners, which are difficult to inspect in the in-service conditions. The authors argue that currently conservative design requirements are prescribed and that with more accurate models and additional experiments, this conservativeness could be relaxed.

In [6], the vulnerability of composite laminates to on-edge impact was confirmed. Besides aeronautical applications, the paper mentions automotive structures, as well, in which impact in the composite structures near the inspection ports or other apertures might be critical. It is dealt with on-edge and near edge impacts in glass fibre composites, presenting results for experimental and FEM evaluations of these impacts. The results presented are relative to the tests carried out for five different incident energy levels: 1,

2, 3, 4 and 5 J and they highlight the potential threat that on-edge impacts can lead to serious composite failure mechanisms. Also, it is mentioned that the development of a physical model that is able to predict the behaviour of composite laminates subject to edge impacts, using damage mechanisms models, would be an important step forward in the analysis of edge impacts in composite structures.

Reference [7] deals with on-edge impacts in CFRP structures, highlighting the importance of further research of this kind of damage, in order to understand better the failure mechanisms and parameters that influence the residual strength of the laminate after an impact event. Also, it is argued that passing from experimental results to the FE model in order to be able to effectively predict the residual strength of an impacted structure is also of importance. To the knowledge of the authors of [7], it is mentioned that papers [5] and [6] are the only ones in the open literature that provide additional insight in the on-edge impact problem. It is also interesting to observe that paper [7] was published one year after the research presented in the current thesis started. It only confirms that colleagues from other research institutions independently recognized the necessity of further investigation of edge impacts in CFRP structures.

The conclusion of the literature overview was that there is a real necessity for a better evaluation of edge impact on CFRP structures, which can occur in areas such as passenger or cargo doors, or any other component during manufacturing and assembly, reducing the damage tolerant properties of the primary structure. The literature overview also indicated that by the time the current research activity started, when it comes to edge impacts, no CFRP related models existed, leaving a lots of room for improvements of the models treating the edge impacts in CFRP structures.

Besides the results given in the literature that can confirm the importance of a further research in the area of edge impacts in CFRP structures, the authors's work for the aerospace industry has allowed her to have an insight on the challenges OEMs are facing with demonstrating the damage tolerant capabilities of primary composite structure and to confirm that her research efforts are indeed in line with the current needs of the industry.

Figure 1.1 illustrates the three common types of edge impacts, with the near-edge impacts being of interest in the research presented in this thesis.

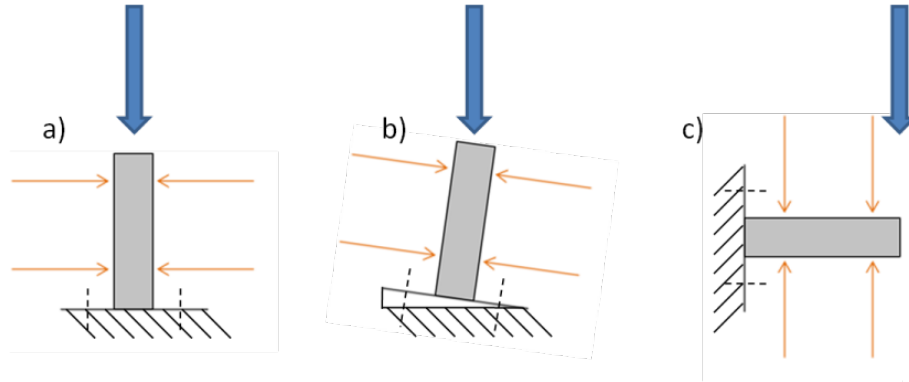


Figure 1.1: Three types of edge impacts, a) on edge impact, b) oblique impact, c) near-edge impact; adapted from [6]

CHAPTER 2

Damage Tolerance in Composite Aeronautical Structures

Federal Aviation Administration (USA) and the European Aviation Safety Agency (EU) prescribe in the Part 25, section 25.571 of their airworthiness regulations, requirements relative to fatigue and damage tolerance in aeronautical structures. Also, additional documents exist that deal explicitly with damage tolerance requirements in composite aeronautical structures. In this chapter it is explained in more detail what these requirements are, what is specific for CFRP structures in particular and how these damage tolerance requirements can be fulfilled.

The contents of this chapter are presented in:

V. Ristori, E. Troiani, G. Ivetic, Fatigue and Damage Tolerance in Composite Primary Aeronautical Structures, AIDAA 2013 - XXII Conference of Italian Aeronautic and Aerospace Association, Naples, Italy, September 2013.

2.1 Background

The arrival of fully composite primary structures of large aircraft in the recent years has been a major challenge to the research community. The increase of the presence of composite components in aeronautical structures has been ongoing for decades and the composite ratio was gradually rising within these structures. This phenomenon is illustrated in Figure 2.1, adapted from [8].

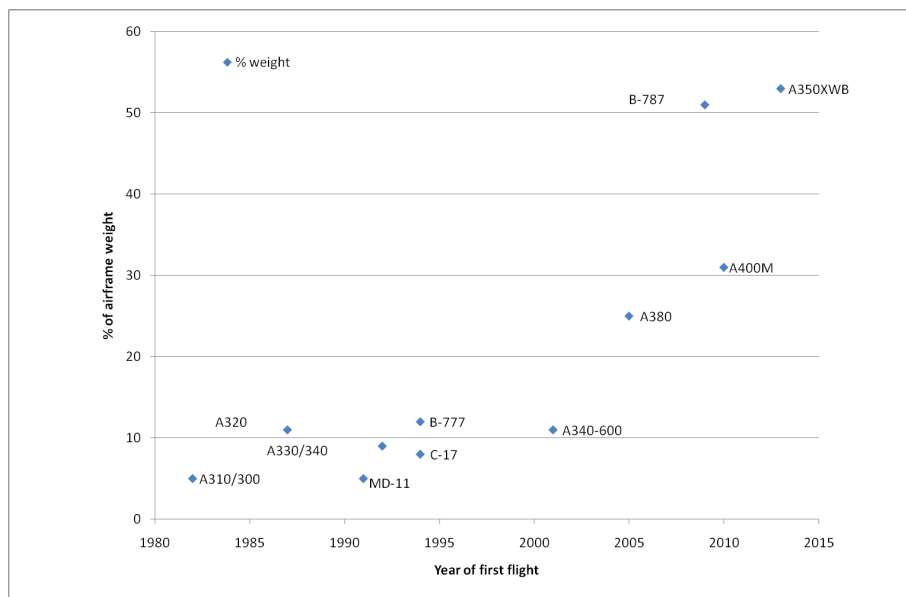


Figure 2.1: Evolution of the composite presence on commercial aircraft

B787 and A350XWB, the CFRP flagships of the major aircraft manufacturers, Boeing and Airbus, respectively, have over 50% of CFRP material in their structure. Even if these two aircraft are commonly referred as CFRP aircraft, it would be more precise to define them as hybrid structure aircraft, since still an important part of their structure is made out of conventional, metallic materials. Figure 2.2 and 2.3 illustrate the weight breakdown of the structure of these two aircraft.

When speaking about the putting into service CFRP made aircraft, the main target is to demonstrate that the use of carbon fibre reinforced plastics can lead to the creation of lighter and greener aircraft while still fulfilling the airworthiness requirements of the certifying bodies.

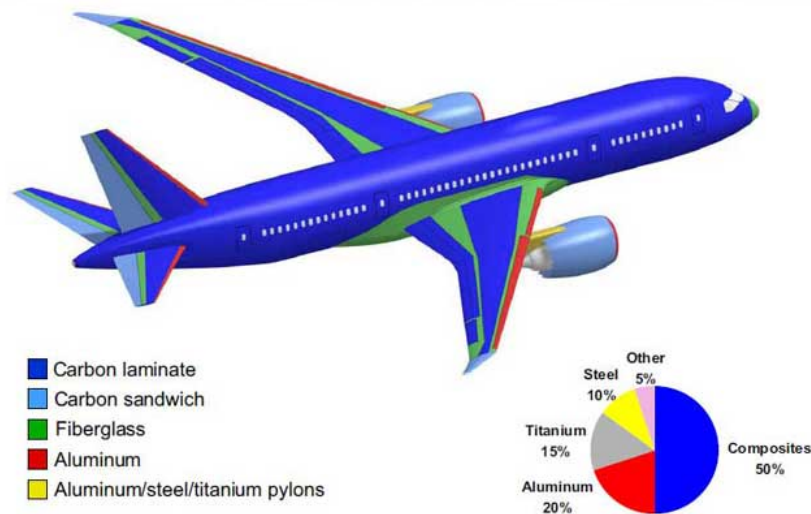


Figure 2.2: B787 materials breakdown per weight, source Boeing

There are comprehensive reports written as far as 25 years ago [9] introducing the problem of damage tolerance in full composite aircraft fuselage. The main issue with composites and damage tolerance philosophy is that the composites are not intrinsically damage tolerant materials since their failure it is often a fragile one, as opposite to that of the metals. For this reason in order to use this kind materials in aircraft's primary structure, a complete new approach to damage tolerance philosophy has become necessary.

Although composite materials are often considered as being fatigue-insensitive, especially when compared to metallic ones, they also suffer from fatigue loads when put in service conditions.

The fatigue behaviour of composite materials is extremely different from that of metallic materials, see Figure 2.4 [10], and for this reason the already developed and validated methods for the fatigue life modelling and prediction of "conventional" materials cannot be directly applied to composite ones due to different responses to fatigue loading. What can be seen from this qualitative figure is that the fatigue resistance of composite materials does not decrease in time as rapidly as it happens with metallic materials.

There are many challenges in trying to create validated methods for the fatigue life prediction of composite materials and one of the main ones is the

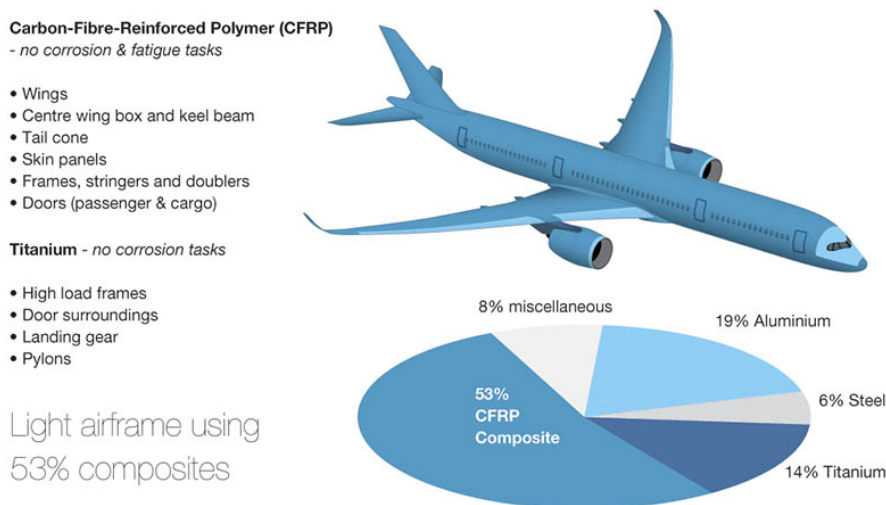


Figure 2.3: A350 XWB materials breakdown per weight, source Airbus

large number of different material configurations resulting from the multitude of fibers, matrices, manufacturing methods, lamination stacking sequences, just to name the most important ones.

That is not the only specific issue which makes the definition of a method to guarantee the damage tolerant capability of a composite material structures an extremely difficult task, among other specific issues it is possible to list:

- environment (moisture and temperature reduce strength)
- poor heat and electrical conduction (lightning strike)
- low out of plane strength and bond quality
- composites can be brittle (vulnerable to load peaks, impact damage)
- engineering property variability (strength and fatigue)
- prediction of failure loads, modes, and locations
- damage detection (delamination, Barely Visible Impact Damage) and evaluation of residual strength
- fire behaviour (toxic fumes, fibre release, post fire strength)

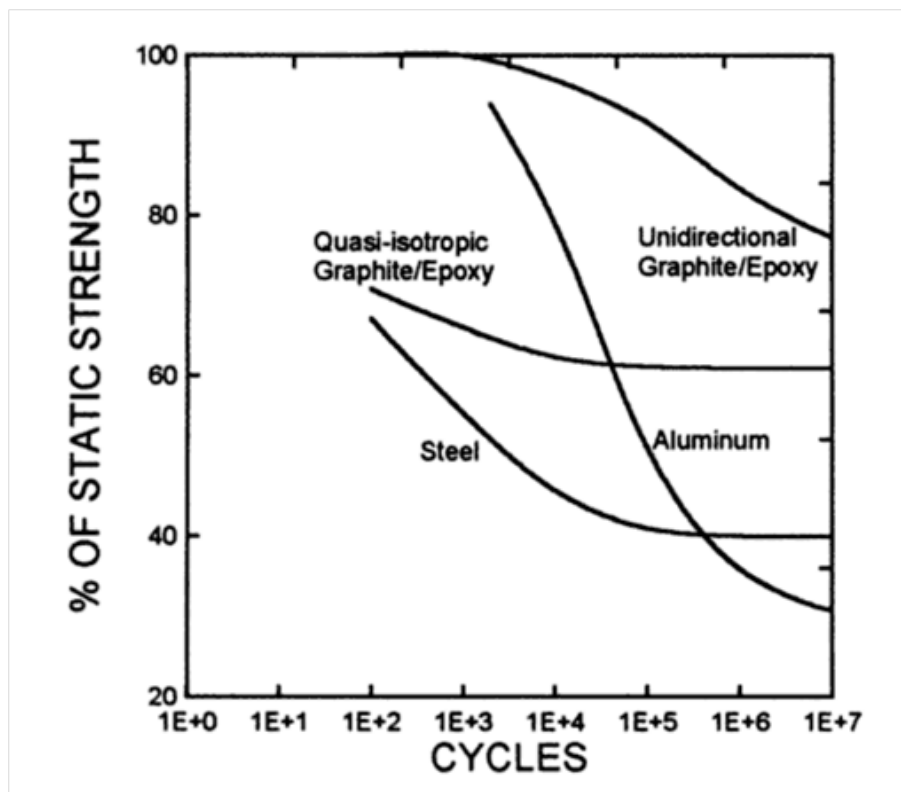


Figure 2.4: Fatigue behaviour of composite vs. metallic materials

All these issues makes the development of a commonly accepted method to cover all these variances difficult.

2.2 Airworthiness Regulations

The Federal Aviation Administration (FAA - USA) and the European Aviation Safety Agency (EASA - EU) prescribe in the Part 25, section 25.571 of their airworthiness regulations, requirements relative to fatigue and damage tolerance in aeronautical structures, whatever their material may be. Also, additional documents exist that deal explicitly with damage tolerance requirements in composite aeronautical structures. In this chapter it is explained in more detail what this requirements are, what is specific for CFRP structures in particular and how these damage tolerance requirements can be fulfilled.

CS 25.571, paragraph a) states that [11]:

An evaluation of the strength, detail design, and fabrication must show that catastrophic failure due to fatigue, corrosion, manufacturing defects, or accidental damage, will be avoided throughout the operational life of the airplane.

The first document that was explicitly covering the certification issues of composite structures was the FAA Advisory Circular 20-107 from 1978, [12].

The circular was updated in 1984 to issue 20-107A [13], while the latest issue of this circular [1] states:

There are factors unique to the specific composite materials and processes used for a given application. For example, the environmental sensitivity, anisotropic properties, and heterogeneous nature of composites can make the determination of structural failure loads, modes, and locations difficult. The reliability of such evaluation depends on repeatable structural details created by scaled manufacturing or repair processes. The extent of testing and/or analysis may differ for a structure depending upon the criticality to flight safety, expected service usage, the material and processes selected, the design margins, the failure criteria, the database and experience with similar structures, and on other factors affecting a particular structure.

It is interesting to observe that the date of the latest issue of the circular 20-107B (08 September 2009) corresponds with the date in which Airbus filed the application with FAA and EASA for the type certification of A350 XWB (both on 15 November 2009).

What is clear when reading the airworthiness regulation is that the certification authorities do not list explicitly how their requirements should be fulfilled, rather they state what is the capability that an aircraft needs to have in order to guarantee a safe flight.

The documents that deal explicitly with damage tolerance requirements in composite aeronautical structures (already mentioned circular [1] and its European counterpart, circular [2]) also state:

Damage tolerance evaluation starts with identification of structure whose failure would reduce the structural integrity of the aircraft. A damage threat assessment must be performed for the structure to determine possible locations, types, and sizes of damage considering fatigue, environmental effects, intrinsic

flaws, and foreign object impact or other accidental damage (including discrete source) that may occur during manufacture, operation or maintenance.

In order to meet these requirements, several factors need to be taken into consideration, which will be discussed in the following sections.

2.3 Damage Tolerance in composite aeronautical structures

In order to understand the issue of Damage Tolerance in composite structure it is necessary to understand the different behaviour between metals and composites.

By definition, to be damage tolerant, a structure needs to be able to maintain Limit Load capability throughout the entire life of the aircraft despite possible damages that can (and will) occur during its operative life. Moreover the damages that will be naturally present on the structure need to evolve in a way for which it is possible to find them and repair them before the structure loses its load carrying capability.

In fact, while metals show gradual degradation of their residual strength when subjected to fatigue loads, this degradation in composite materials is usually caused by an external factor, such as an impact, and it brings to step-wise degradation of residual strength, Figure 2.5, adapted from [14]. As a result, this may cause the composite structure to lose its ultimate load carrying capability for a longer period of time, compared to metals, before the damage could be detected and repaired.

For this reason it is safe to say that the composite material are intrinsically not damage tolerant and all the methodologies valid for the metallic ones cannot be applied in the case of primary composite structures.

This not-damage tolerant behaviour is the main reason for the current design approach to composite aeronautical structures. The only possible approach to having damage tolerant composite structures at the moment is the so called “no-growth” concept of Barely Visible Impact Damage (BVID). This means that a defect which is present but not detectable cannot propagate inside the structure.

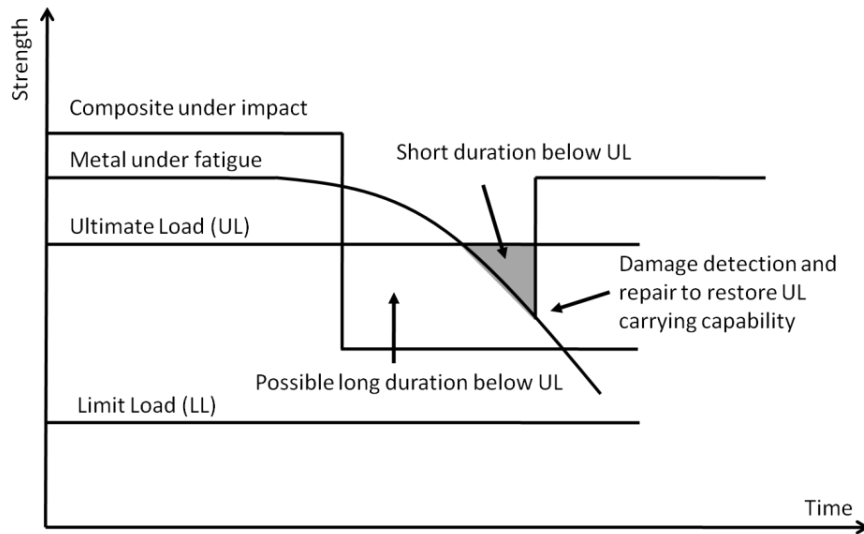


Figure 2.5: Residual strength of composite vs. metallic material under fatigue or impact loading

For this reason when sizing a composite material component for an aircraft it is necessary to assess a maximum defect size (allowable size) which will not propagate under the operative loads and which at the same time will not compromise the Ultimate Load carrying capability of the structure itself.

Per design criteria hence, if a damage is not visible the structural integrity is not affected and the fatigue life and ultimate load are sustained. Moreover (per design) this defect will not propagate to a significant extent during aircraft life (“no-growth” concept). If, instead, a damage is visible, than an inspection must be performed to determine the extent of the damage and establish the repair requirements. The extent of the damage is usually determined by an ultrasonic inspection for monolithic structures.

For a real life application, this is implemented as following :

- Ultrasonic inspections are performed at manufacturing stage on 100 % of the parts in order to detect any manufacturing anomaly which may not be detected with a detailed visual inspection.
- If the recorded defects are allowable, that they will not reduce the structure strength and its ultimate load carrying capability

- If a detected defect is not allowable, the full strength capability has to be restored
- All detected manufacturing anomalies are recorded

This no growth approach needs to be used together with additional factors in order to be able to meet the airworthiness requirements on composite structures. These factors include damage threat assessment, inspection program definition, damage detectability, fatigue tests and analyses [3].

2.3.1 Damage Threat Assessment

The damage threat assessment needs to be performed according to Ref. [1] and [2].

Some factors to consider in development of a damage threat assessment for a particular composite structure include:

- Part function
- Location on the aircraft
- Past service data
- Accidental damage threats
- Environmental exposure
- Impact damage resistance
- Anomalous service or maintenance handling events that can overload or damage the part

In order to perform this assessment thought it is mandatory to categorize the possible damages. Damages can be classified in five categories:

1. Barely Visible Impact Damage (BVID): allowed damages
2. Visible Impact Damage (VID): identifiable with a normal inspection program, it requires a repair

3. Obvious Impact Damage: found within a few flights, it requires repair after finding
4. Discrete Source Damage: obvious to flight crew, it requires repair after flight
5. Anomalous Damage: not covered in design phase, it requires immediate repair

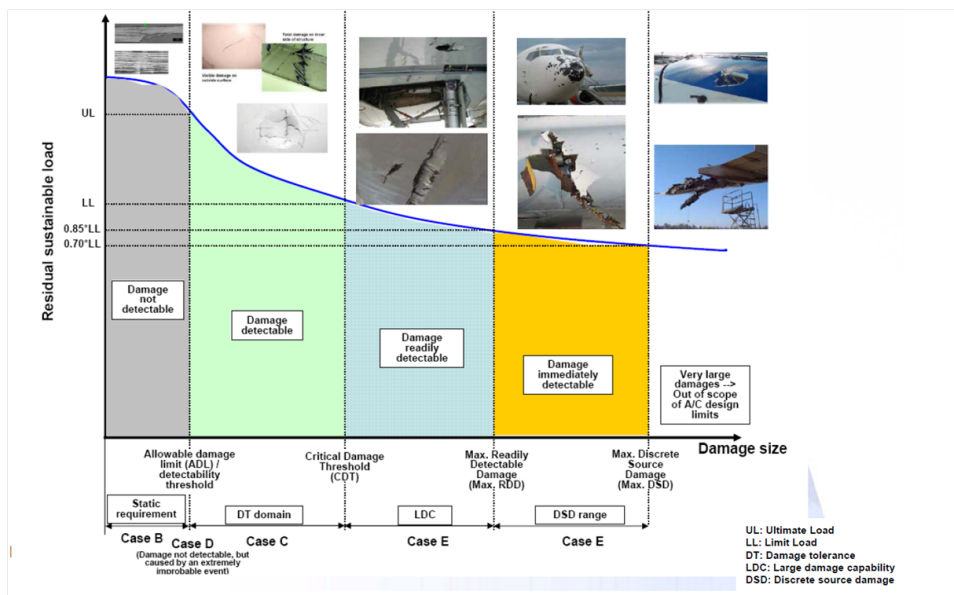


Figure 2.6: Load Levels versus Damage Sizes, from [15]

As it can be seen from Figure 2.6 from [15], the allowed damages are the ones for which the structures must maintain the Limit Load carrying capability. This means that in this case the structure is statically sized, for this type of damage there is no damage tolerance capability of the structure. The area of damage tolerance for composites material is that of the visible impact damages. This damages in fact needs, to be identified and repaired through an inspection program in perfect synchrony with the damage tolerance philosophy. This is the type of damages this work is going to investigate.

As already mentioned, a damage threat assessment is crucial in order to understand in which area of an aircraft the probability of an impact is

higher and of which magnitude this impact can occur and this damage threat assessment helps greatly in the definition of an inspection program. Usually, the inspection program is a design requisite for which the structure needs to be sized. According to Figure 2.7 from [16], more than two thirds of impacts are registered in the door or door surrounding areas, and this is why the investigation of the near edge impacts is of great importance for the aeronautical structures.

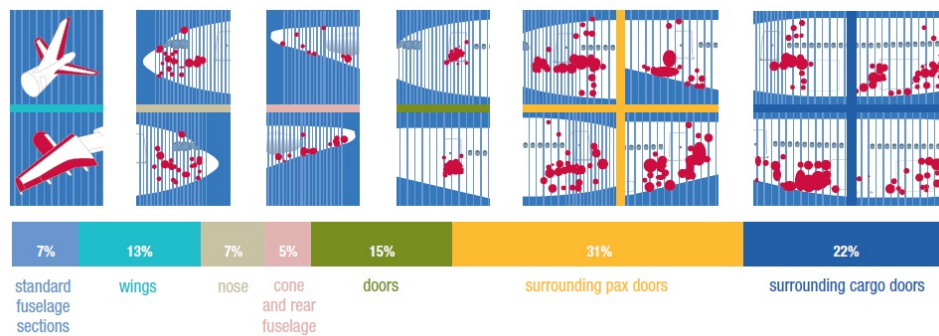


Figure 2.7: Percentage of impacts on different zones of an aircraft, from [16]

2.3.2 Damage detectability

The damage detectability depends obviously on the type of inspection that is being carried out. It is the main parameter in determining the size of the Barely Visible Impact Damage (BVID) and one of the most important information in order to define a correct inspection program. It is possible and necessary in fact to have another type of study: the one correlating Detectability and Energy Levels (Figure 2.8 from [17]).

Analysing the figure, four distinct areas can be identified:

1. non detectable damages - realistic energy levels
2. non detectable damages - non realistic energy levels
3. detectable damages - realistic energy levels
4. detectable damages - non realistic energy levels

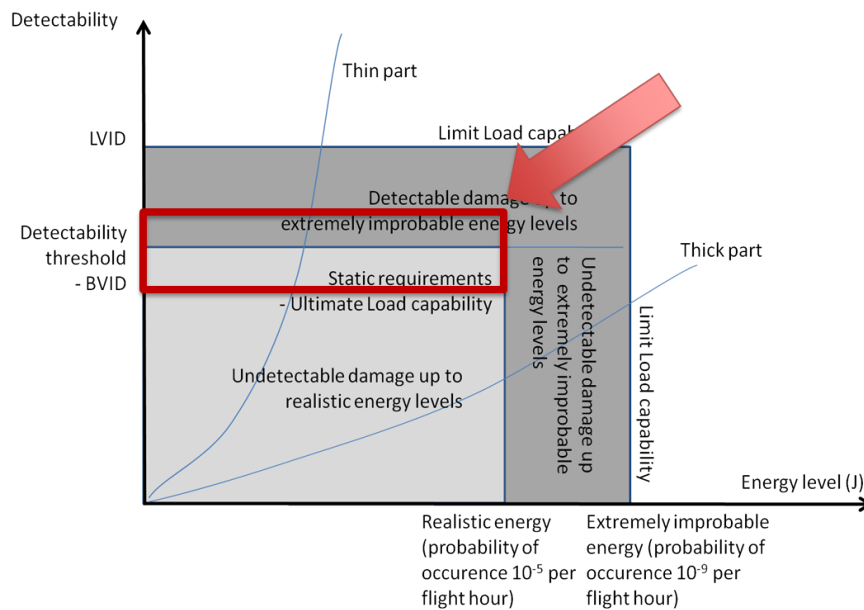


Figure 2.8: Defects Detectability versus Energy Level Probability, from [17]

The current work deals with detectable damages (VID) caused by realistic energy levels and hence fits in the damage tolerance area of structure justification.

2.3.3 Fatigue Tests and Analyses

The fatigue tests and analyses need to show the “no-growth” concept, which requires no initiation of new damage and no growth of existing damages (BVID). Impact tests are carried out in order to establish the behaviour of a composite structure when subjected to these impact loads and to determine the severity of the impact, based on different impact positions and energies. The tests are as of today the only prediction for the fatigue behaviour of composites material, the nature of composites material, the current knowledge on them and their numerical simulation does not permit any other means of prediction or justification.

Typical test pyramids are carried out in order to establish the behaviour of the damaged structure. A typical schematic illustration of a testing pyramid is given in Figure 2.9, reported from [18].

In order to be able to demonstrate the “no-growth” concept, the fatigue

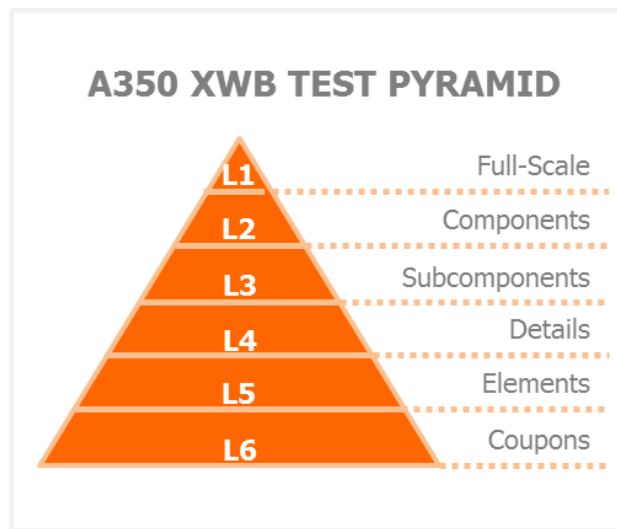


Figure 2.9: Typical test pyramid

tests are carried out, in which is investigated what is the loading level that the structure can be subject to and still satisfy the “no-growth” concept. Usually, this loading level is given as a certain percentage of the strength of the laminate and this loading level, based on tests, guarantees that no defect propagation is present and that nucleation of new defect does not occur.

The results presented in this thesis therefore aim to contribute to better understanding of CFRP structures when subjected to near-edge impacts and to help defining a simple and robust general visual inspection technique that would allow to assess, within engineering accuracy, the damage present inside a composite structure.

CHAPTER 3

Experimental analysis

In this chapter, the experimental campaign carried out on CFRP specimens is described in detail. The specimens were cut from the laminated CFRP plates and subjected to near edge impacts, NDT testing and compression after impact tests.

The content of this chapter is based on data presented in:

V. Ristori, E. Troiani, M.P. Falaschetti, M. Montemurro, A. Baeten, G. Ivetic, G. Molinari, Damage Tolerance assessment of Edge impacts in CFRP structures, 28th Symposium of the International Committee on Aeronautical Fatigue, Helsinki, Finland, June 2015, ISBN: 978-9513874421

In addition, data presented in MSc theses of students who collaborated on this research project, Ref. [19], [20] and [21] are reported in this chapter and their contribution to this PhD work is kindly acknowledged.

3.1 First Experimental Campaign - calibration

The initial experimental campaign was used to build and calibrate the testing equipment and to obtain a baseline for the future tests. Several impact energies were introduced in the specimens and the first results from compression after impact tests were obtained. Accelerometer measurements were also carried out, providing important inputs for successive numerical analyses, such as the duration of the impacting event.

3.1.1 Specimens Preparation

Specimens of nominal size of 100x50 mm were cut from a laminated plate with the size of 500x250 mm. The specimens were produced out of 18 plies of unidirectional prepreg fibres, produced by Hexcell, with ply thickness of 0.131 mm. The used stacking was $[45,90,-45,90,-45,45,0,45,-45]_s$ with the total nominal thickness of the specimens of 2.36 mm.

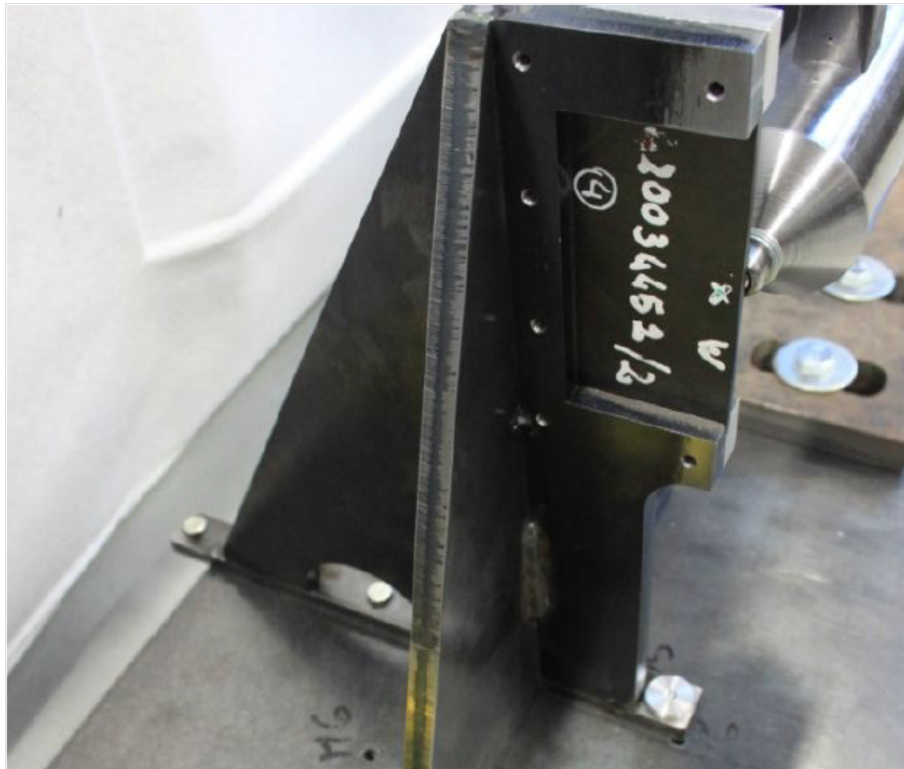


Figure 3.1: Introducing near edge impacts in CFRP specimens

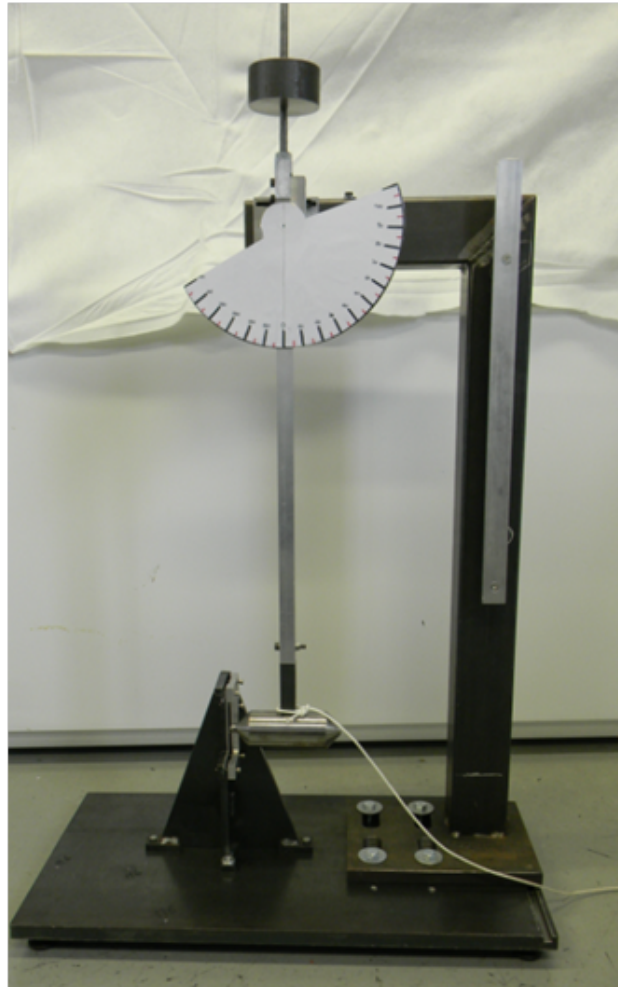


Figure 3.2: Used Charpy pendulum

3.1.2 Near Edge Impacts

A Charpy pendulum was used in order to introduce low energy impacts in the specimens, Figures 3.1 and 3.2. The impacting element of the pendulum was a steel cylinder, Figure 3.3, with a mass of 1817 g, having a semisphere of 7 mm in diameter at its end.

It is important to mention that it was possible to consider only the mass of the impactor element because the pendulum arm has been appropriately calibrated in order to place the center of gravity in the center of the cylinder.

The arm has in fact been equipped with a counterweight (1653 g) po-



Figure 3.3: Charpy Pendulum Impacting Element



Figure 3.4: Counterweight element used to balance the pendulum staff

sitioned at an appropriate distance from the center of rotation (see Figure 3.4), which acts to balance the weight of the arm itself (645 g). The staff is hence completely balanced, Figure 3.5, and the center of gravity of the pendulum is placed in the center of the cylinder.



Figure 3.5: Balanced staff

The impacts were performed by appropriately inclining the pendulum, introducing impact energies from 3 J to 12 J.

A goniometer has also been fixed to the pendulum (Figure 3.6) in order to establish the angle of the spring-back of the pendulum and to determine the amount of energy absorbed by the specimens, by knowing the initial releasing angle of the pendulum.

A fixing rig used to keep the specimens in place during the impacts was produced and is also visible in Figure 3.7.

3.1.3 Experimental results

The external appearance of the impacted specimens, using different impacting energies, is illustrated in Figure 3.8, Figure 3.9 and Figure 3.10. It can be observed that the energy level of 3 J does not introduce visible damage on the surface of the specimen, while the opposite is true for the energy level of 12 J.

The lateral view of the specimen impacted with 12 J energy level is illustrated in Figure 3.11. The damaged shape of the specimen is in line with the typical experimental findings reported in the literature, relative to typical impact damage mode for composite laminate, Figure 3.12, from [22].

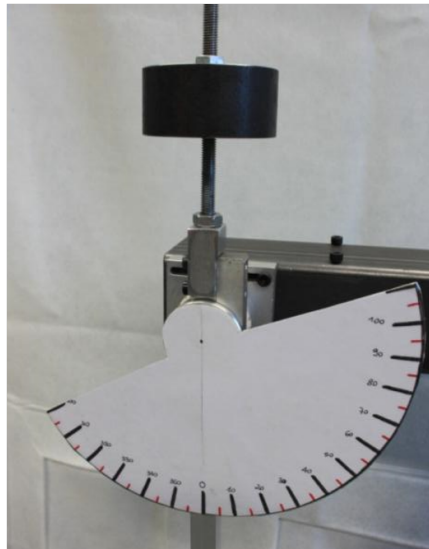


Figure 3.6: Goniometer used to determine the spring back angle of the pendulum

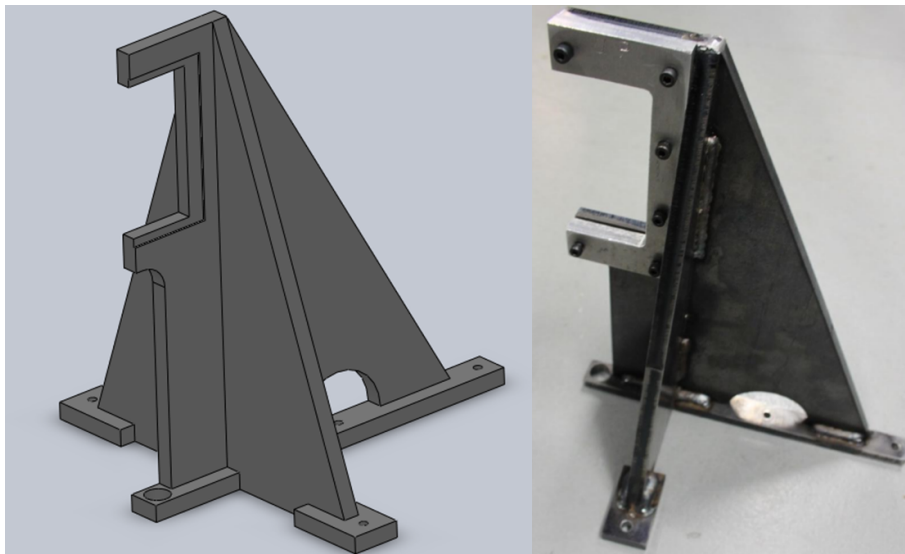


Figure 3.7: Fixing rig used for the impact tests

3.1.4 Accelerometer measurement of impact events

The data relative to acceleration along three axes were registered. The used nomenclature is x-axis for vertical direction, y-axis for transversal direction and z-axis the impact direction (specimen thickness direction), see

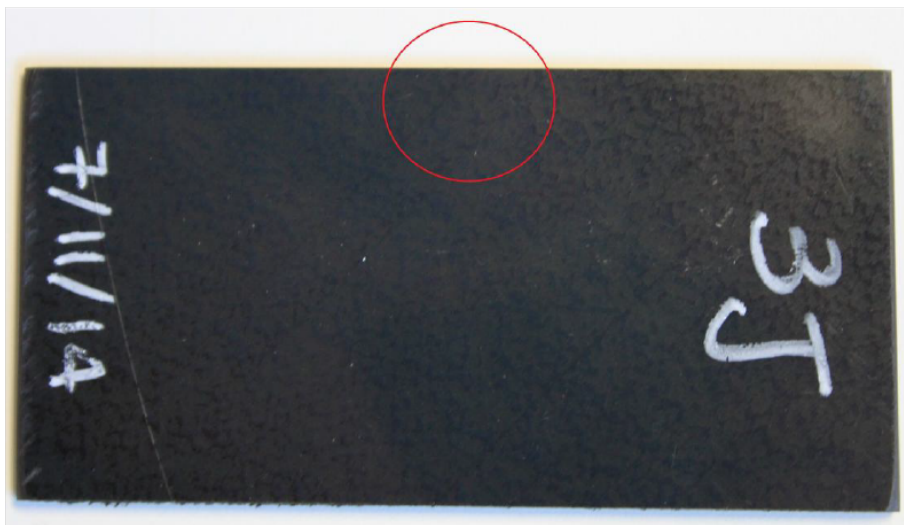


Figure 3.8: Specimen after near edge impact, 3J

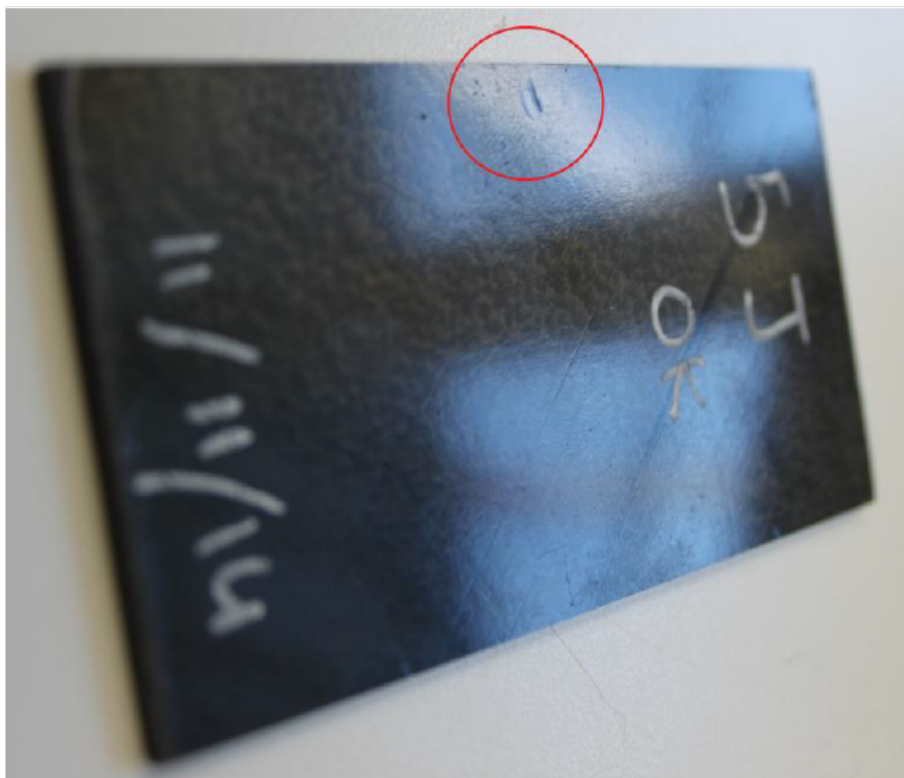


Figure 3.9: Specimen after near edge impact, 5J



Figure 3.10: Specimen after near edge impact, 12J

Figure 3.13. The accelerometer was fixed to the impactor using a magnetic clip. However, the magnetic bond was not enough by itself to keep the accelerometer in place, so this problem was solved by additional taping the accelerometer to the impactor, visible in Figure 3.13.

A triaxial sensor PCB Mod. 356B21 was used. The total length of data acquisition was 5 seconds. In this timeframe, the impact event and successive 5 to 6 spring-back impacts were registered, Figure 3.14. However, only the initial impacting event with the total duration of 0.01 s is of interest. This measurement is later used as a step duration in the numerical analysis of near edge impacts, reported in Chapter 6.

In Figure 3.15 to Figure 3.18, the measured results for acceleration in z-axis direction are given. In Figure 3.19 to Figure 3.22, displacement in y-axis direction are given. For coordinate axes definition, refer to Figure 3.13. The figures are relative to the different impacting energies tested (4, 5, 6 and 7 J).

The data illustrated in the curves relative to accelerometer results are provided in tabular form in Table 3.1, as well, where g is relative to the gravitational acceleration constant. It is interesting to observe that there is a practically linear correlation between lower energy levels (from 4 J to 6

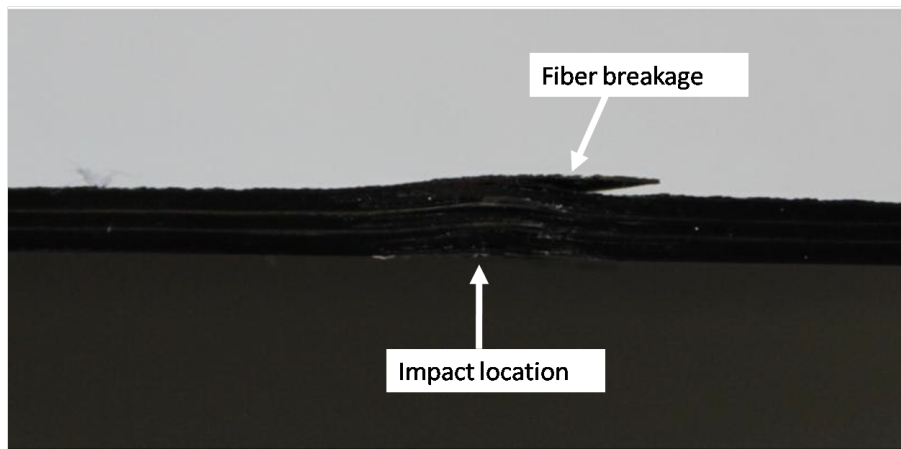


Figure 3.11: Specimen after near edge impact, 12J

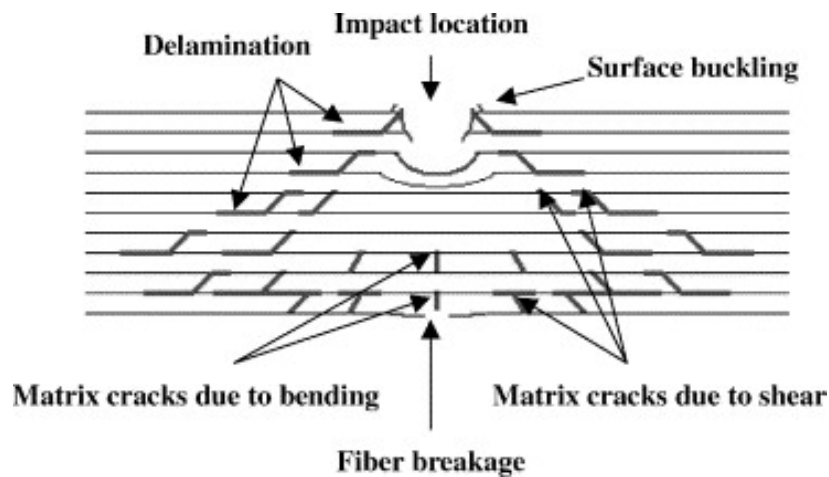


Figure 3.12: Schematic representation of a typical impact damage mode for composite laminate [22]

J) and relative maximum accelerations and displacements. In this case, the energy is absorbed by the fibers in an elastic way, while delaminations still can occur, absorbing the kinetic energy through creation and propagation of delamination fronts (basically, cracks). However, after a certain threshold level, which in this case happened to be between 6 J and 7 J, there is no more elastic linear absorption of the impact energy and the fiber damage mechanism has to take place in order to absorb the inserted energy. This phenomenon can explain why higher deformation levels and lower accelerations were

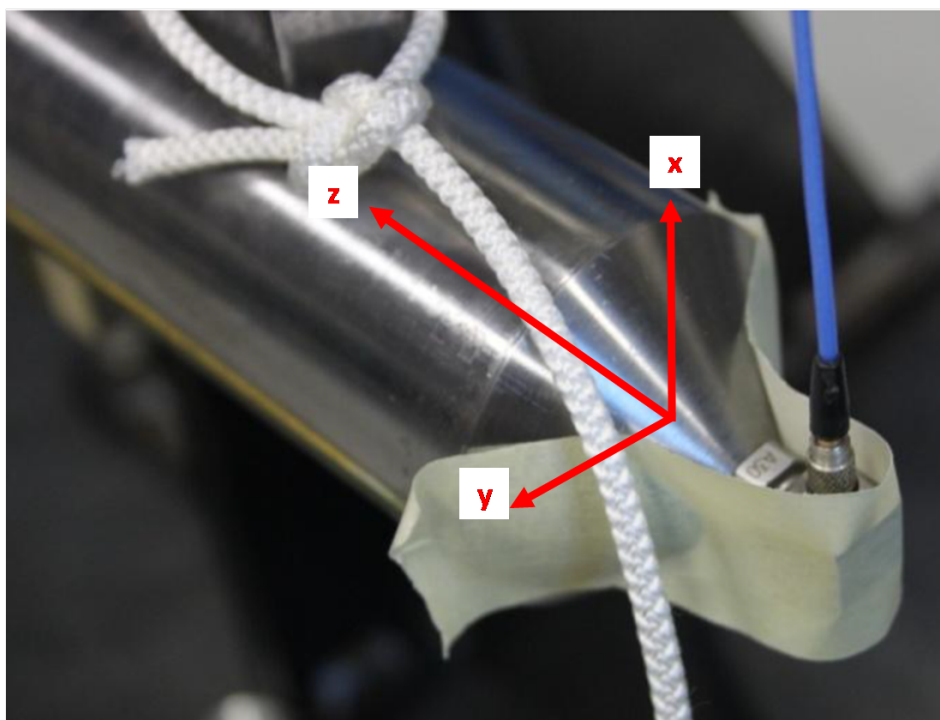


Figure 3.13: Triaxial accelerometer fixed to the impacting element

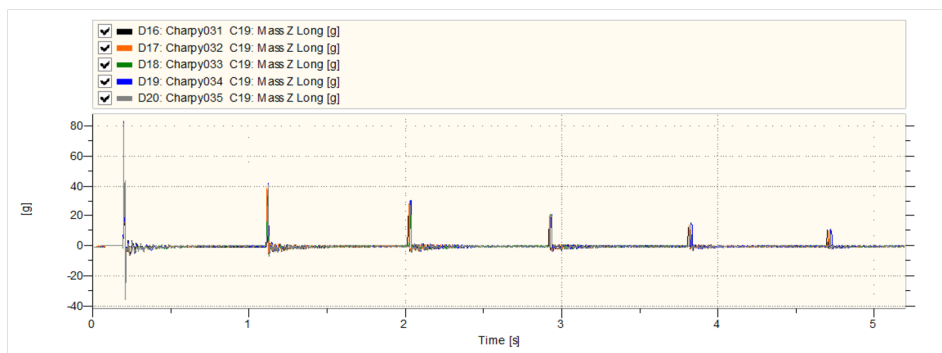


Figure 3.14: Typical acceleration-time diagram in z-axis direction

measured at 7J, in respect to other tested configurations.

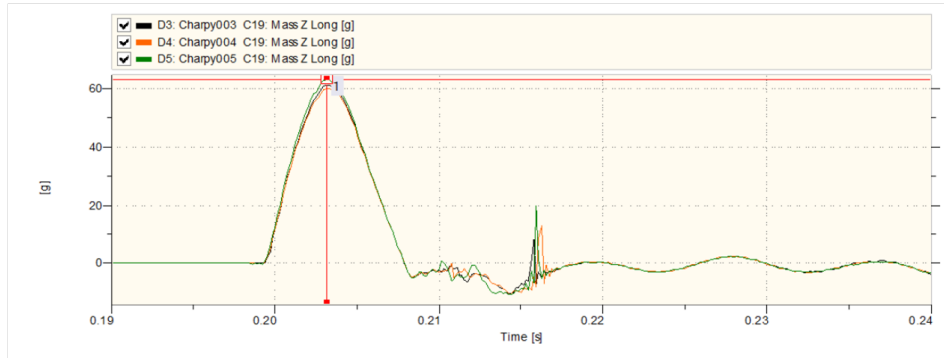


Figure 3.15: Acceleration-time diagram in z-axis direction, 4J

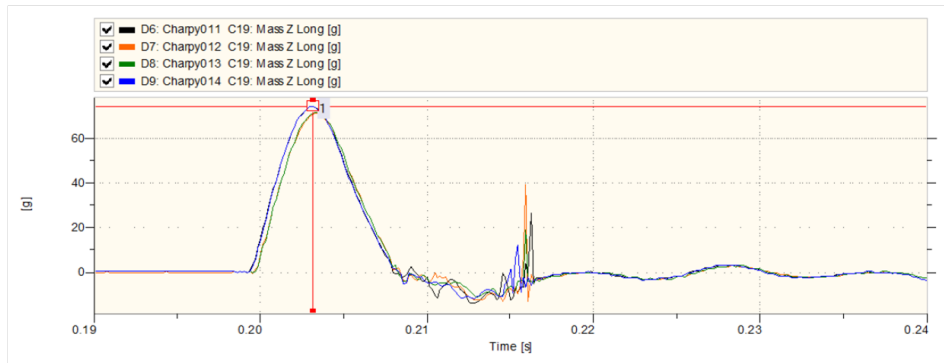


Figure 3.16: Acceleration-time diagram in z-axis direction, 5J

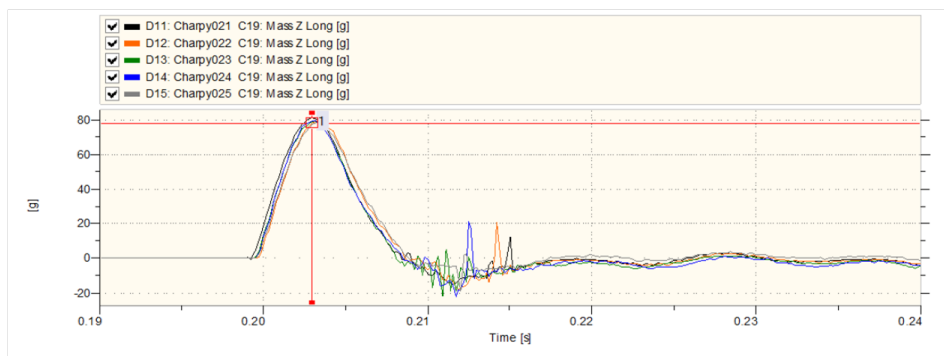


Figure 3.17: Acceleration-time diagram in z-axis direction, 6J

3.1.5 Compression After Impact Tests

The specimens which were later tested with Compression After Impact (CAI) tests were divided as reported in Table 3.2.

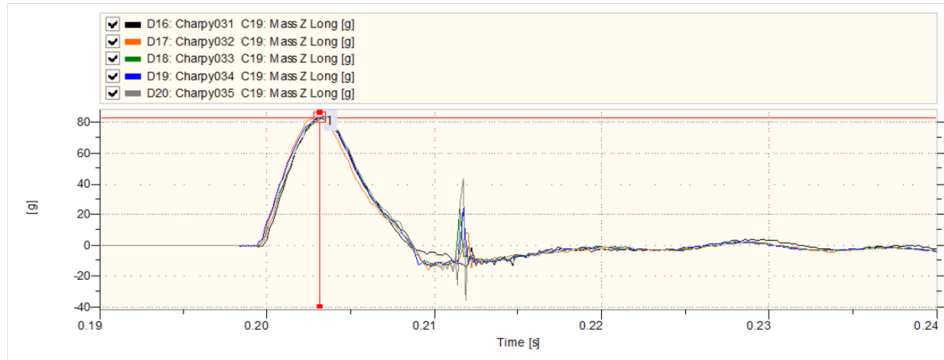


Figure 3.18: Acceleration-time diagram in z-axis direction, 7J

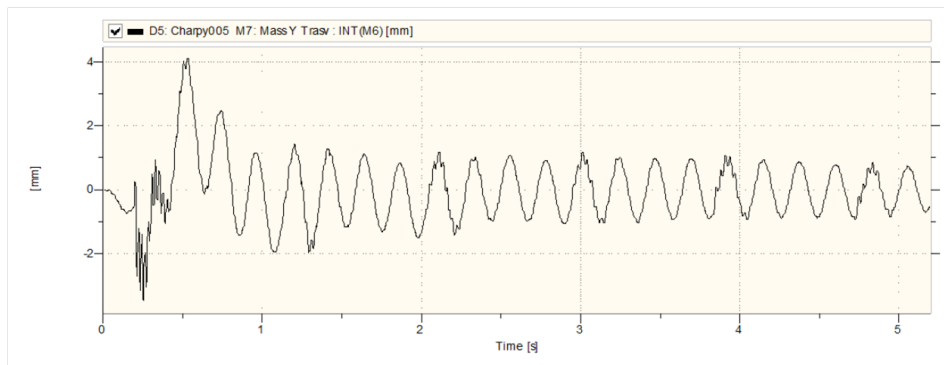


Figure 3.19: Displacement-time diagram in y-axis direction, 4J

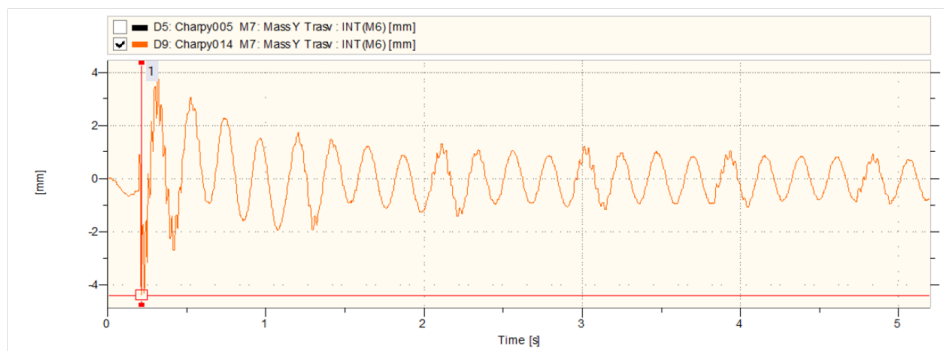


Figure 3.20: Displacement-time diagram in y-axis direction, 5J

The non-impacted specimen and central impacted specimens were used in order to obtain a baseline value, against which the near edge impacts are compared.

By knowing the initial releasing angle of the pendulum, and the spring-

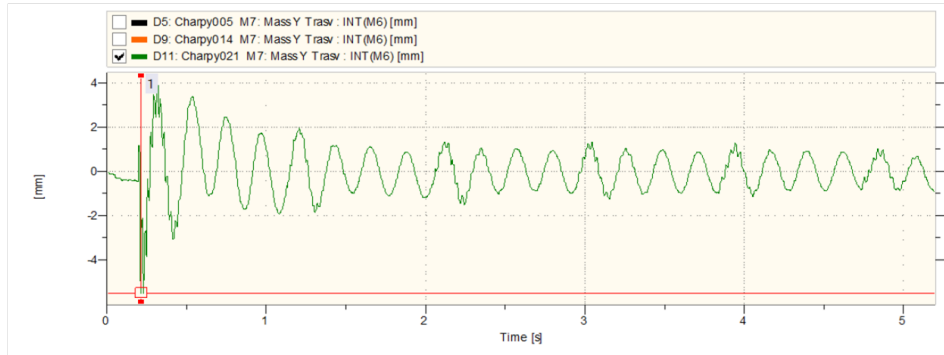


Figure 3.21: Displacement-time diagram in y-axis direction, 6J

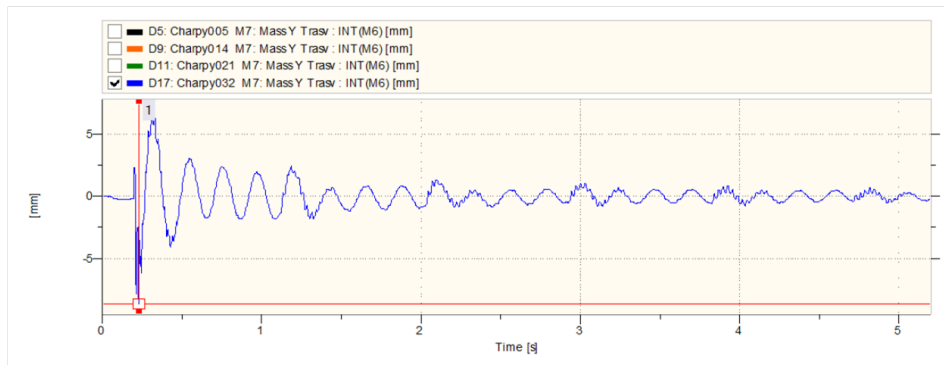


Figure 3.22: Displacement-time diagram in y-axis direction, 7J

back of the pendulum, Table 3.3, it was possible to determine the amount of energy absorbed by the specimens. Table 3.4 gives an overview of applied energies on different specimen groups. It is possible to see in both the tables that the impacts performed using the energy level of 4 J showed uniform results. The observed spring back angle and calculated absorbed energies are indeed of a comparable magnitude for the case of 4 J impacts. This is not the case for the impact with 6 J energy level. In this case, two distinct result groups can be seen, relative to the level of absorbed energies. After the examination of data, this discrepancy is most likely to be attributed to the execution of the impact itself, rather than to the differences in material properties of the tested CFRP laminates.

The fixing rig used for the CAI tests was designed and realized in order to be able to contain the specimens. A 3D visualisation of the rig is given in

Impact Energy [J]	Maximum	Maximum
	Acceleration [m/s ²]	Deformation [mm]
4	63.28 g	4.11
5	74.66 g	-4.39
6	81.54 g	-5.47
7	83.35 g	-8.65

Table 3.1: Accelerometer data for different energy levels

Specimen Group	Amount	Impact Position	Impact Energy [J]
A	1	Not impacted	-
B	1	Central	4
C	1	Central	6
D	6	Near edge	4
E	6	Near edge	6

Table 3.2: Specimens division - calibration testing campaign

Figure 3.23. In Figure 3.24, a specimen mounted inside the CAI testing rig can be seen.

The initial calibration has put in evidence a typical issue encountered during compression testing of composite materials. Due to the nature of the fixing of the specimen, the specimen itself is able to deform freely in its central part, resulting in failures which are not accepted by the prescribed CAI testing standards, Ref. [23]. In Figure 3.25, an undesirable failure mode is illustrated.

According to [23], this test method can be used to test undamaged polymer matrix composite plates, but historically such tests have demonstrated a relatively high incidence of undesirable failure modes. As alternative, test method described in [24] is recommended for obtaining compressive properties of undamaged polymer matrix composites. The testing method from [24] has been applied in the second experimental campaign described in Section 3.2.3. For the CAI testing of the specimens described in Table 3.2, another testing standard was applied, described in Ref. [25], for which the

Specimen	Impact	Nominal	Initial	Spring-back
Group	position	energy [J]	angle [deg]	angle [deg]
B	Central	4	50	35
D1	Near Edge	4	48	32
D2	Near Edge	4	48	32
D3	Near Edge	4	48	32
D4	Near Edge	4	48	32
D5	Near Edge	4	48	32
D6	Near Edge	4	48	32
C	Central	6	63	40
E1	Near Edge	6	61	38
E2	Near Edge	6	63	25
E3	Near Edge	6	63	39
E4	Near Edge	6	65	23
E5	Near Edge	6	65	24
E6	Near Edge	6	63	39

Table 3.3: Overview of nominal energies, initial and spring-back angles on different specimen groups

already existing testing rigs present in the laboratory were adapted for the tests. This CAI testing setup can be seen in Figure 3.26 and Figure 3.27.

Specimen Group	Impact position	Effective energy [J]	Residual energy [J]	Absorbed energy [J]
B	Central	4.095	2.073	2.022
D1	Near Edge	3.793	1.742	2.052
D2	Near Edge	3.793	1.742	2.052
D3	Near Edge	3.793	1.742	2.052
D4	Near Edge	3.793	1.742	2.052
D5	Near Edge	3.793	1.742	2.052
D6	Near Edge	3.793	1.849	1.944
C	Central	6.259	2.682	3.577
E1	Near Edge	5.906	2.430	3.476
E2	Near Edge	6.259	1.074	5.185
E3	Near Edge	6.259	2.555	3.705
E4	Near Edge	6.619	0.911	5.708
E5	Near Edge	6.619	0.991	5.628
E6	Near Edge	6.259	2.555	3.705

Table 3.4: Overview of applied energies on different specimen groups

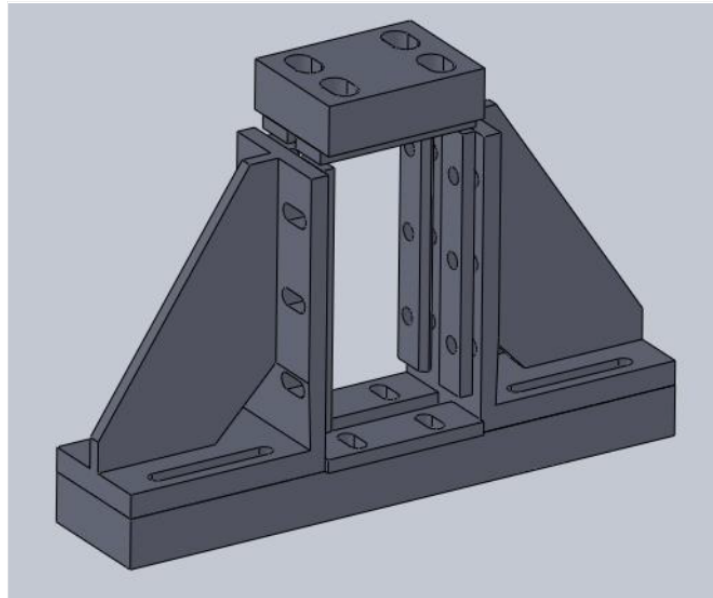


Figure 3.23: CAI testing rig, 3D visualisation

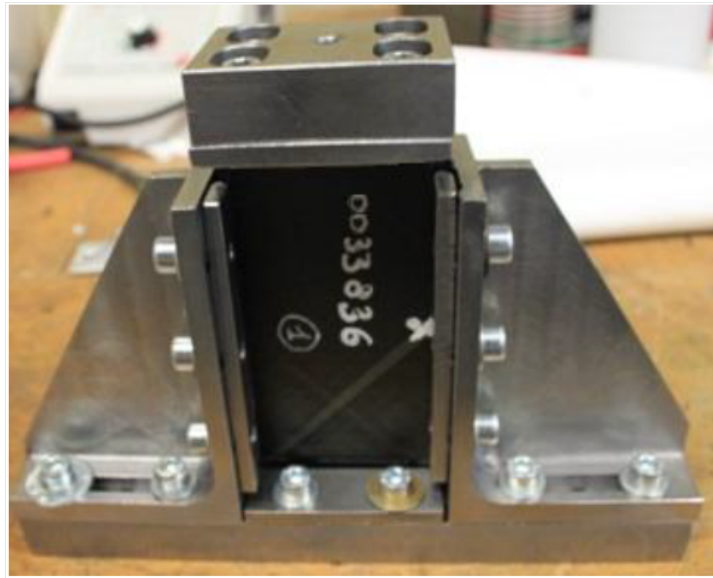


Figure 3.24: CAI testing rig with specimen mounted inside



Figure 3.25: Undesired failure mode close to the extremity of the specimen

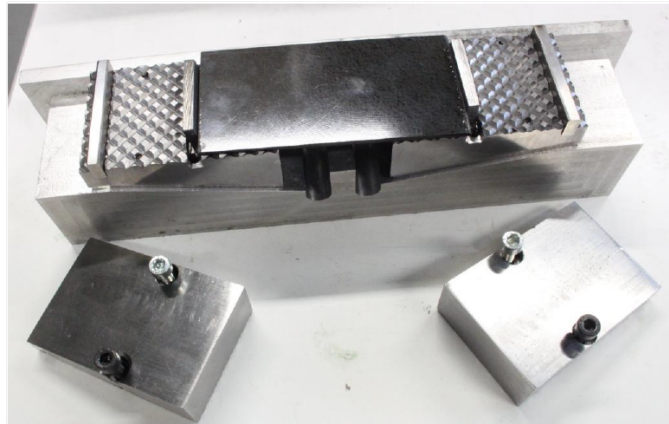


Figure 3.26: Specimen mounted in the testing rig, standard [25]

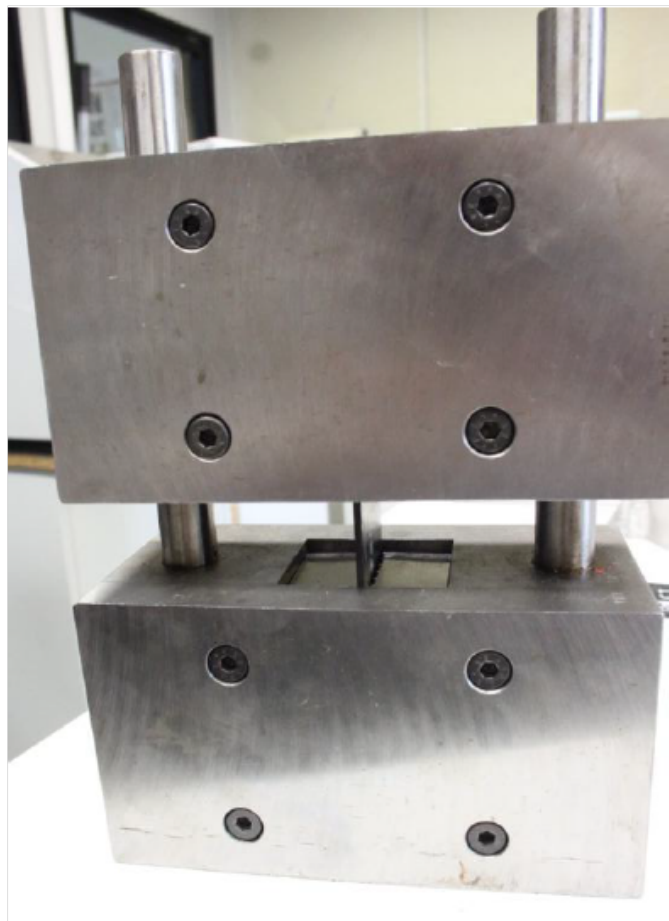


Figure 3.27: Completely mounted testing rig, standard [25]

In Table 3.5, an overview of the measured forces at the failure of the specimen is provided. It is interesting to observe that there is no significant difference in maximum applied force necessary to induce failure in the specimen. This finding might be explained with the fact that relatively low energy levels were inserted in the structure. However, the maximum force level is consistent with the measurements of absorbed and residual energy, demonstrating the lowest residual strength in specimens E4 and E5, which are the specimens with the highest absorbed energy after impact, see Table 3.4.

In Figure 3.28, the appearance of a specimen at the end of an CAI test is given, showing a failure mode which is in line with the allowed failures described by the CAI testing standard.

Specimen Group	Impact position	Cross-section [mm ²]	Applied Force [N]	σ_{max} [MPa]
A	-	119.139	-22946	-197.6
B	Central	118.832	-23883	-202.8
D1	Near Edge	121.560	-24870	-207.3
D2	Near Edge	121.367	-24071	-202.2
D3	Near Edge	119.571	-24766	-208.5
D4	Near Edge	119.190	-23410	-197.7
D5	Near Edge	118.632	-24601	-207.1
D6	Near Edge	118.040	-24870	-212.2
C	Central	118.236	-24461	-209.2
E1	Near Edge	120.217	-24714	-209.7
E2	Near Edge	120.312	-24849	-209.2
E3	Near Edge	118.615	-22730	-191.7
E4	Near Edge	116.066	-22872	-198.6
E5	Near Edge	117.220	-22284	-189.2
E6	Near Edge	115.381	-23269	-200.5

Table 3.5: Overview of applied forces at failure for different specimen groups

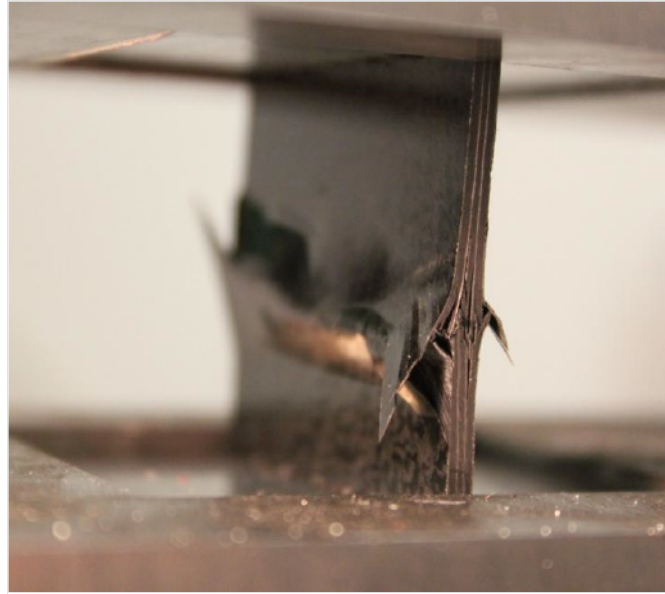


Figure 3.28: Failure of a specimen after the CAI test

3.2 Second Experimental Campaign

Different impact positions (near edge and central) were tested and compared. After initial attempts with different compression after impact testing methods, the compression after impact tests were carried out using the Combined Loading Compression (CLC) test method.

3.2.1 Specimens Preparation

An additional experimental campaign was defined in order to characterize the Compression After Impact (CAI) behaviour of near-edge impacted CFRP specimens, comparing it with the compression strength of the pristine specimens. The specimens used for the experiments are obtained from a rectangular CFRP plate, with the dimensions of 490x420 mm. A total of 25 specimens were produced and used for the experiments, 3.29.

To the best of author's knowledge there is no prescribed standard for compression after edge impact tests. The specimen size was 140x30 mm, with the length of the specimens taken from ASTM D6641/D6641M-14 standard [24], relative to compression testing of composites, and the width chosen

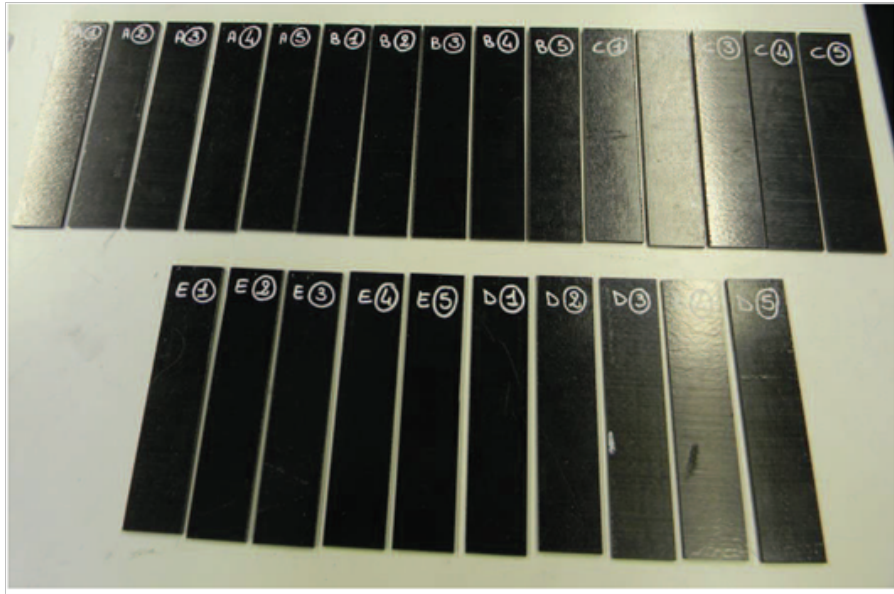


Figure 3.29: CFRP specimens cut from the laminated plate

based on the maximum size that could fit into test equipment prescribed by the same standard. The specimens were produced out of 9 plies of cross-ply prepreg fibres, produced by DeltaPreg, with ply thickness of 0.32 mm. The used stacking was $[90/0_2/90/90]_s$, with the total nominal thickness of the specimens of 2.76 mm.

The specimens were divided in 5 groups, as described in Table 3.6.

Group	Impact Position	Impact Energy [J]
A	Not impacted	-
B	Near edge	3
C	Near edge	5
D	Central	3
E	Central	5

Table 3.6: Specimens division

It is important to note that the used fixing rig is the same for the near edge and the central impacts. This boundary condition is not realistic for the central impact since in this case, the constraint should be applied on all

4 edges of the specimen. The decision to apply the same boundary condition to both types of impact was taken in order to have a measurement of the difference in static residual strength based only on the position of the impact. It is safe to assume that if the more realistic boundary condition were to be applied this difference would be even greater than the measured one during this experimental campaign. The FEM results that simulate these two cases are presented in Chapter 6 and, as expected, the laminated area is higher in the case in which one free edge is present, in respect to the case in which all four edges are blocked.

3.2.2 Near Edge Impacts

The same Charpy pendulum of the first experimental campaign was used in order to introduce low energy impacts in the specimens. The previously described impacting element of the pendulum (steel cylinder, having a sphere of 7 mm in diameter at its end), was used, Figure 3.30. The impacts were performed by appropriately inclining the pendulum, introducing impact energies of 3 J and 5 J.

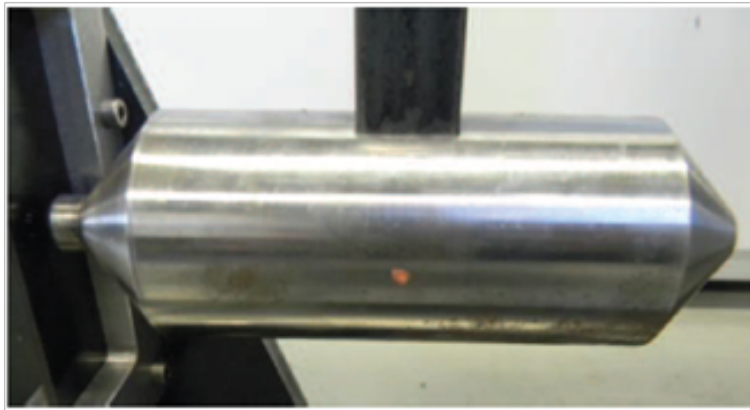


Figure 3.30: Impacting element

Also, the previously designed and produced fixing mechanism, Figure 3.1 and Figure 3.31, was used to maintain in an appropriate position the specimen in respect to the impacting element and to be able to contain the specimen itself.

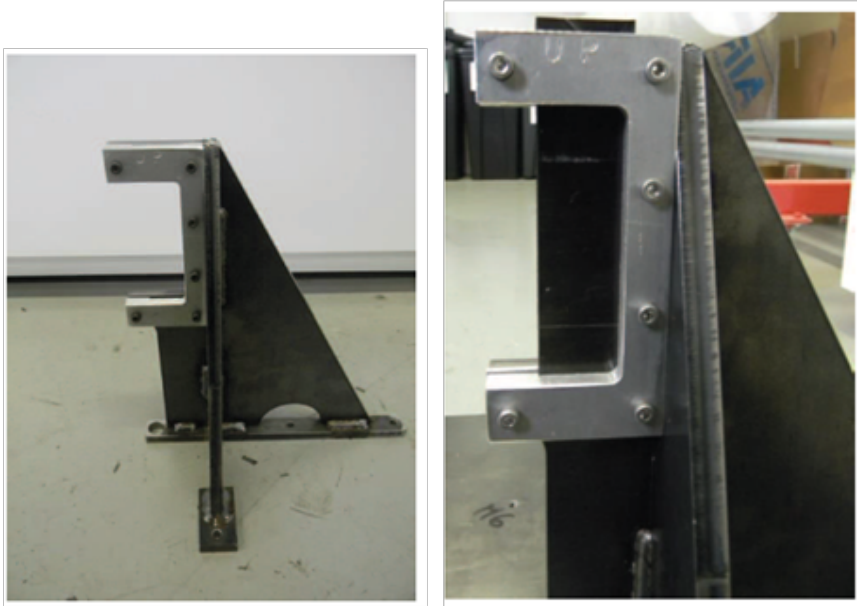


Figure 3.31: Fixing mechanism (left) and with the specimen mounted (right)

3.2.3 Compression After Impact Tests

The compression tests were carried out according the ASTM D6641 standard [24]. The CLC fixing mechanism is composed of four steel blocks that allow fixing of standard size specimens of 140 mm length and of a maximum width of 30 mm, used for this experimental campaign, Figure 3.32. The CLC tests allow introducing both normal and shear loads in the structure, with the possibility of changing appropriately their ratio, by changing the fixing force of the mechanism.

An MTS hydraulic press machine, Figure 3.33, was used for the CLC tests [26], with the maximum nominal loading of 100 kN. In the same figure, a detail showing the mounted CLC fixing at the beginning of the compression test can be seen.

3.2.4 Experimental results

The impacts were observed via a camera and the recordings were inspected after the tests. This was necessary in order to establish the angle of the spring-back of the pendulum and to determine the amount of energy absorbed

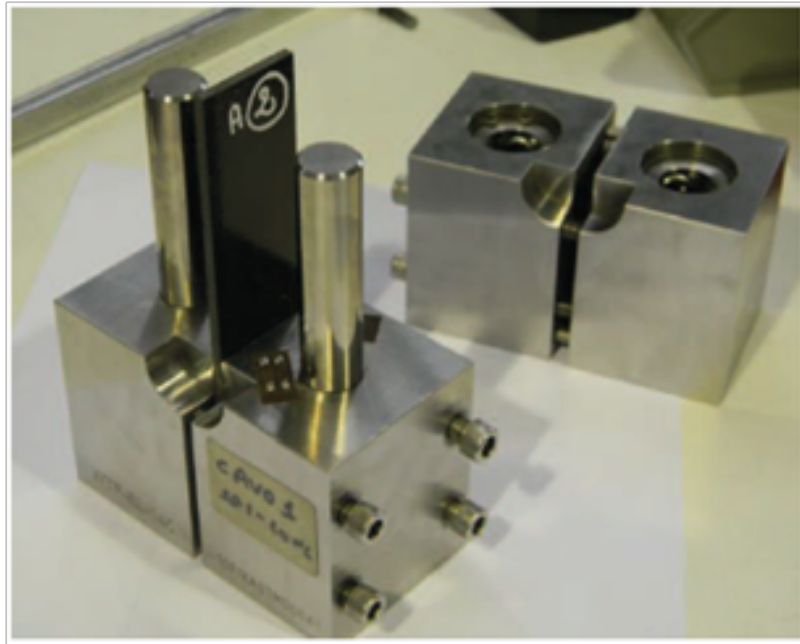


Figure 3.32: Specimen mounted in the CLC fixing

by the specimens, by knowing the initial releasing angle of the pendulum.

Table 3.7 gives an overview of applied energies on different specimen groups.

The typical surface condition of the specimens, after the impact, is illustrated in Figure 3.34. The images a) and b) show the impacted area for near edge impacts, with the energy levels of 3 J and 5 J, while images c) and d) show central impact for the matching energy level, 3 J and 5 J respectively.

Subsequently, the impacted specimens, together with the baseline (not impacted specimens), were subjected to CLC tests. The readings of the hydraulic press, relative to the applied force at the compression failure of the specimens, for each of the specimen group, are given Table 3.8.



Figure 3.33: Hydraulic press machine, left and with the CLC fixing mounted, right

Specimen	Effective energy [J]	Residual energy [J]	Absorbed energy [J]
B1	3.342	0.907	2.435
B2	3.065	0.831	2.234
B3	3.065	1.244	1.821
B4	3.342	1.244	2.098
B5	3.202	1.336	1.866
C1	4.704	0.907	3.797
C2	4.866	1.244	3.622
C3	4.866	1.069	3.797
C4	4.704	0.986	3.724
C5	4.543	0.831	3.712
D1	3.342	1.155	2.187
D2	3.342	1.069	2.273
D3	3.484	1.069	2.415
D4	3.202	1.069	2.133
D5	3.202	0.986	2.216
E1	5.029	1.431	3.598
E2	5.196	1.529	3.667
E3	4.866	1.336	3.53
E4	4.543	1.244	3.299
E5	4.866	1.431	3.435

Table 3.7: Overview of applied energies on different specimen groups

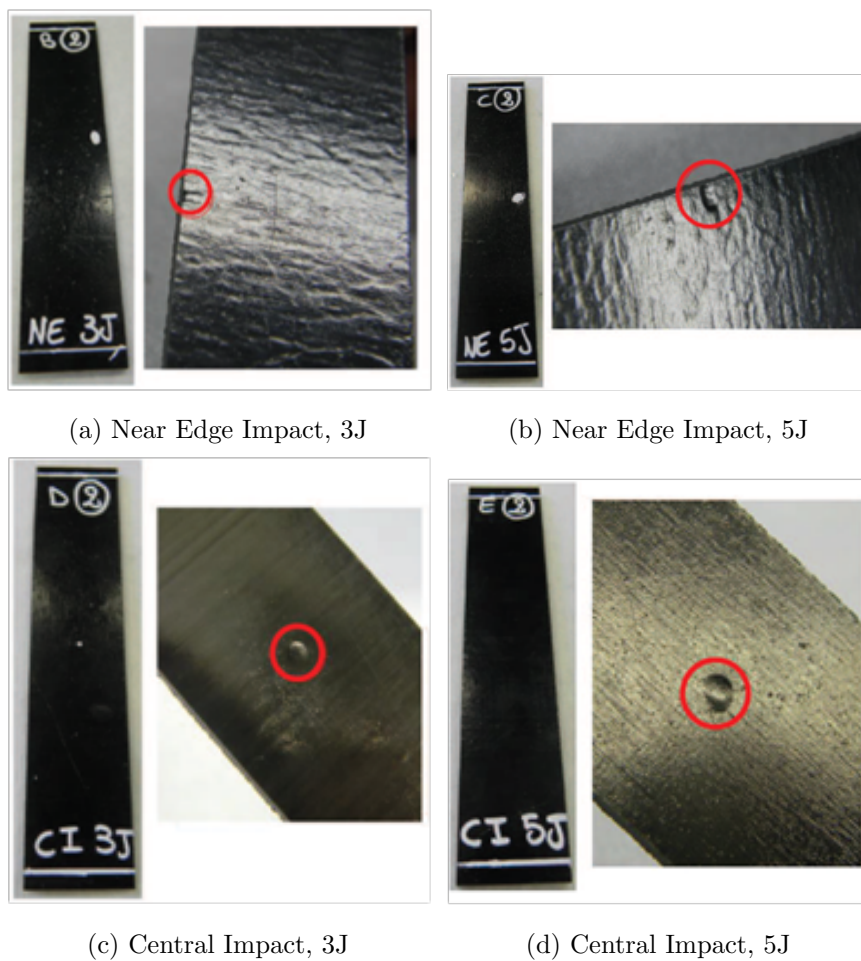


Figure 3.34: Visual inspection of the specimens after impact, typical surface condition

Group	Spec.	Nominal Cross Section [mm ²]	Max Applied Force [N]	Max Stress [MPa]	Average Difference %
Baseline	A1	82.03	-34172	-416.58	—
	A2	87.94	-32845	-373.49	
	A3	87.31	-34216	-391.89	
	A4	85.87	-32593	-379.56	
	A5	84.00	-31091	-370.13	
Near edge 3J	B1	69.76	-23913	-342.79	11.36%
	B2	81.87	-20118	-245.73	
	B3	84.52	-29537	-349.47	
	B4	89.13	-38055	-426.96	
	B5	88.12	-30601	-347.27	
Near edge 5J	C1	84.11	-20473	-243.41	31.31%
	C2	84.94	-20684	-243.51	
	C3	84.36	-29630	-351.23	
	C4	86.78	-26366	-303.83	
	C5	87.14	-16114	-184.92	
Central 3J	D1	68.67	-21924	-319.27	10.40%
	D2	81.16	-30936	-381.17	
	D3	72.44	-22220	-306.74	
	D4	81.67	-30050	-367.94	
	D5	71.01	-25746	-362.57	
Central 5J	E1	81.42	-26725	-328.24	14.24%
	E2	84.8	-24547	-289.47	
	E3	83.58	-31050	-371.5	
	E4	84.23	-35774	-424.72	
	E5	82.11	-19922	-242.63	

Table 3.8: Maximum applied force at failure for different specimen groups

CHAPTER 4

Modelling Failure in Composite Structures

An introduction to failure modelling in composite structures is given in this chapter. There are several numerical models available in the literature that define the failure of composite structures after external damage, such as impacts, and they are discussed briefly.

4.1 Failure Models of Composite Structures

In this section a summary of most commonly used failure models is given, reported from Ref. [27] and [28]. It is important to state that there are several other failure models proposed by different authors, which refine the existing models for specific applicability range, which are in closer agreement with experimental results. A good overview of these models can be found in [29].

Many of them are relatively simple models that draw inspiration from the analysis of isotropic metallic components, in which a failure is defined once a certain level of stress or strain is reached within the structure. Alternatively, additional failure models were developed and proposed in which different levels of complexity are taken into account. Some of them, like Tsai-Hill or Tsai-Wu models tend to define a failure in a way analogue to Von-Mises stress in metallic structures.

However, even if these relatively simple models are able to capture the behaviour of composite structures in simpler cases, the real nature of composite material, in which two distinct constituents exist, fiber and the matrix, is not taken into account through application of these models.

Additional, more complex failure models were introduced by Hashin and Rotem or Puck, in which more physically realistic damage and failure mechanisms are taken into account. In the current thesis, the failure model developed by Hashin and Rotem was considered for the analysis of damage in CFRP structure after near-edge impact and it will be presented in more detail in the next sections.

The main failure modes of laminated fiber-reinforced composites are, reported from [35]:

Delamination

Composite materials made of different plies stacked together tend to delaminate. The bending stiffness of delaminated panels can be significantly reduced, even when no visual defect is visible on the surface or the free edges.

Matrix compression failure

What is commonly referred to as matrix compression failure is actually shear matrix failure. Indeed, the failure occurs at an angle with the loading

direction, which is evidence of the shear nature of the failure process.

Fiber compression failure

This failure mode is largely affected by the resin shear behaviour and imperfections such as the initial fiber misalignment angle and voids. Typically, kinking bands can be observed at a smaller scale, and are the result of fiber micro-buckling, matrix shear failure or fiber failure.

Matrix tensile failure

The fracture surface resulting from this failure mode is typically normal to the loading direction. Some fiber splitting at the fracture surface can usually be observed. In the current work, it is the matrix tensile damage initiation that is used as an index of predicting the delamination in the impacted component.

Fiber tensile failure

This failure mode is explosive. It releases large amounts of energy, and, in structures that cannot redistribute the load, it typically causes catastrophic failure.

According to the data from some 20 years ago, presented in Ref.[30], the frequency of usage of the most commonly applied failure models is given in Figure 4.1. What this figure shows is that models with lower degree of complexity are most widely used, specially in industrial environment, according to Ref. [28] and [30]. The author of this work can only confirm from her own experience, that maximum strain failure model (with necessary corrections) is indeed used in the industry. Other more complex models, which try to capture the interaction behaviour between fiber and the matrix are mostly applied in the academic environment, and this trend can be easily seen by performing an overview of the open literature.

An excellent overview of different failure criteria under in-plane (2D) loadings is presented in Ref. [31]. The authors of *The First World-Wide Failure Exercise*, coordinated and reported between 1996 and 2004, dealt with benchmarking of different failure criteria used for fiber reinforced plastics and they report the effectiveness of different models, comparing the experimental results with the model predictions. Since the end of this exercise, two more failure exercises were carried out by the same authors (WWFE-II [32] [33], concluded in 2012 and WWFE-III [34] started in 2013) with the intention of

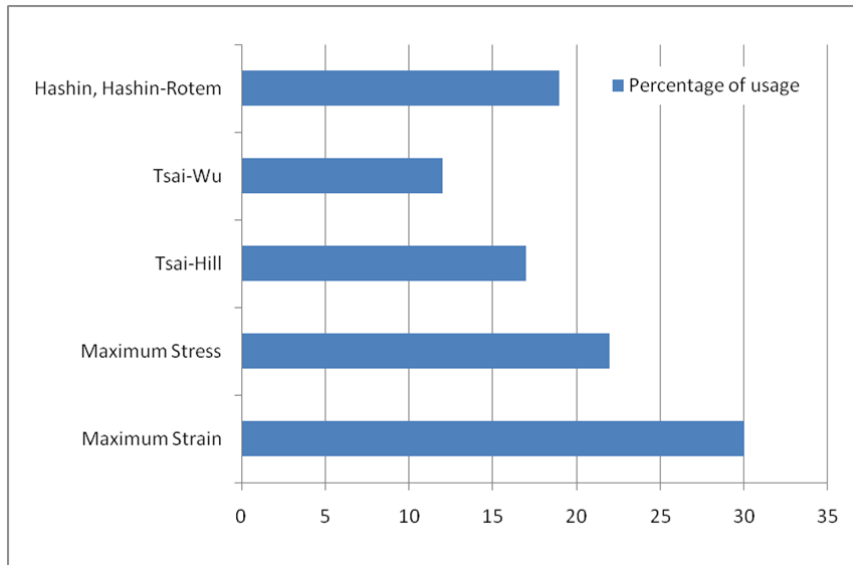


Figure 4.1: Lamina failure criteria by frequency of usage

advancing further the knowledge on failure criteria in composite materials.

4.1.1 Maximum Stress Failure Model

For a unidirectional ply, the following failure modes are usually recognized:

- Tension failure along the fibres (X_t)
- Compression failure along the fibres (X_c)
- Tension failure transverse to the fibres (Y_t)
- Compression failure transverse to the fibres (Y_c)
- Pure shear failure of a ply (S)

In the case of maximum stress failure model, the principal stresses in each ply are compared with their corresponding strength values X_t , X_c , Y_t , Y_c and S . The maximum stress failure criterion can be expressed as:

- $\sigma_x < X_t$ or X_c depending on whether σ_x is tensile or compressive
- $\sigma_y < Y_t$ or Y_c depending on whether σ_y is tensile or compressive

- $|\tau_{xy}| < S$

where σ_x , σ_y and τ_{xy} are ply stresses in the ply coordinate system (x parallel to fibres and y perpendicular to fibres, Figure 4.2).

Failure occurs as soon as one (or more) of the left-hand sides equals the right-hand side. The failure mode is the one for which the equation is met.

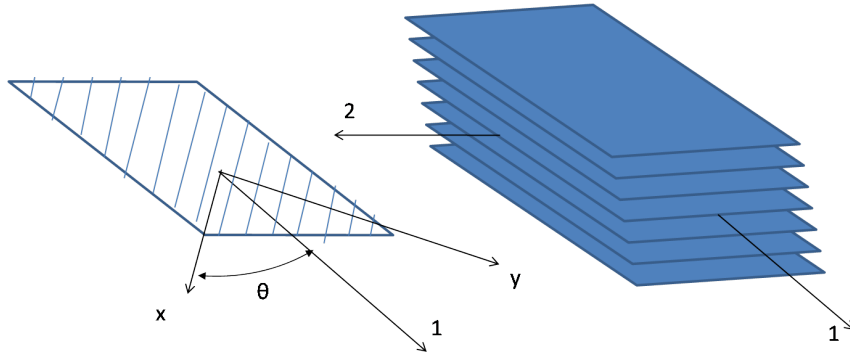


Figure 4.2: Ply (left) and laminate (right) coordinate systems

4.1.2 Maximum Strain Failure Model

Similar to the maximum stress failure model, the maximum strain failure criterion is expressed as:

- $\epsilon_x < \epsilon_{xu}^t$ or ϵ_{xu}^c depending on whether ϵ_x is tensile or compressive
- $\epsilon_y < \epsilon_{yu}^t$ or ϵ_{yu}^c depending on whether ϵ_y is tensile or compressive
- $|\gamma_{xy}| < \gamma_{xyu}$

where ϵ_x , ϵ_y and γ_{xy} are ply strains in the ply coordinate system (x parallel to fibres and y perpendicular to fibres). Also, ϵ_{xu}^t , ϵ_{xu}^c , ϵ_{yu}^t , ϵ_{yu}^c and γ_{xyu} are allowable strains in the corresponding direction and loading (tensile or compressive).

In the industrial practice, these allowable strains are usually reduced with the coefficients that take into account the environmental effects, as well as the possible presence of initial defects. Indeed, the necessity of considering initial defects in the CRRP structure subjected to fatigue loads are discussed in Chapter 2.

If all left-hand sides of the equation are less than the right-hand sides there is no failure. Failure occurs, in a specific failure mode, as soon as one (or more) of the left-hand sides equals the right-hand side.

4.1.3 Tsai-Hill Failure Model

In the two previous failure criteria, each stress or strain is individually compared with its respective allowable. In general, however, stresses (or strains) may interact with each other and lead to failure, even if each compared individually with its respective allowable suggests that there is no failure.

Hill [36] proposed a combined failure criterion for composite materials. For a single ply under plane stress, with ply axes xy as shown in Figure 4.1, the criterion has the form:

$$F_x\sigma_x^2 + F_y\sigma_y^2 + F_{xy}\sigma_x\sigma_y + F_s\tau_{xy}^2 = 1$$

The form of this equation is analogous to the von Mises yield criterion in isotropic materials.

In fact, the equation was proposed for a three-dimensional state of stress as a model of yielding in anisotropic materials. For composite materials, where the concept of macroscopic yielding (at the laminate or the ply level) is not really valid, failure replaces yielding.

The equation recognizes the fact that the failure strengths of a composite ply are different in different directions. Tsai [37] determined the stress coefficients F in the previous equation by considering three simple loading situations:

- only σ_x acts on a ply with corresponding strength X
- only σ_y acts with corresponding strength Y
- only τ_{xy} acts with corresponding strength S

The final form of the TsaiHill failure criterion is:

$$\frac{\sigma_x^2}{X^2} - \frac{\sigma_x\sigma_y}{X^2} + \frac{\sigma_y^2}{Y^2} + \frac{\tau_{xy}^2}{S^2} = 1$$

4.1.4 Tsai-Wu Failure Model

The Tsai-Wu failure criterion [38] is a generalization of the Tsai-Hill failure criterion, creating a curve fit based on tensor theory and accounting for the fact that composites have different strengths in tension and compression. This means that the Tsai-Wu failure theory is not entirely based on physical phenomena, but includes a curve-fitting aspect.

One of the unknown coefficients in the Tsai-Wu failure model is obtained by requiring that the von Mises yield criterion be recovered if the material were isotropic. The distortional energy theory on which the von Mises criterion is based, is not applicable to composites so the Tsai-Wu criterion should be viewed as a useful curve fit more than a physics-based model of failure.

4.1.5 Puck Failure Model

Failure criteria based on the failure behaviour of brittle materials are expected to more accurately describe fracture of composite materials. Puck and Schürmann in Ref. [39] introduce inter fibre fracture criteria, which are based on the brittle failure behaviour of composites. Their criteria makes a distinction between different fracture modes (A, B and C), and they are illustrated in Figure 4.3, reported from Ref. [39].

The ability of the model to describe physical phenomena that occur during the fibre and inter-fiber fracture is can explain it relative high complexity. As already shown in Figure 4.1, the failure models preferred by industry environment tend to be more simple, which on one hand reduces its accuracy, but increases the speed of their evaluation.

4.1.6 Hashim-Rotem Failure Model

The failure model proposed by Hashin and Rotem is described in Ref. [40] and [41].

The authors describe a quadratic failure criteria, pointing out that their choice of quadratics is based on curve fitting considerations and not on physical reasoning.

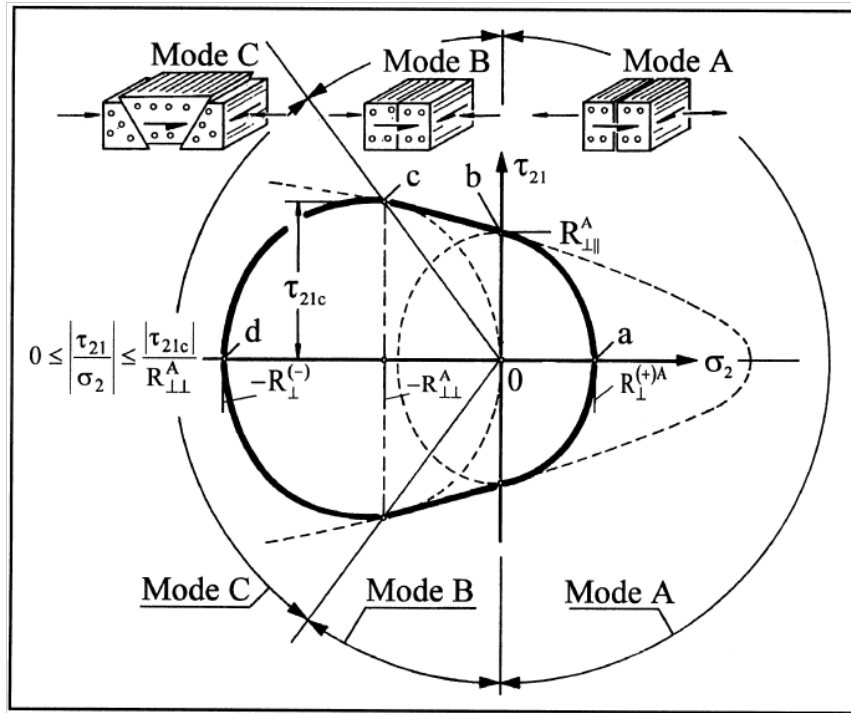


Figure 4.3: Representation of three different fracture modes: A, B and C, from [39]

The simplest approximation of a failure surface is by planes parallel to coordinate planes, e.g., rectangular parallelepiped in three-dimensional stress space. Such representations have their uses for constant stress criteria in fixed directions with respect to material axes, but are in general of insufficient accuracy due to neglecting of stress interaction effects. The next approximation would consist of oblique planes which intersect the stress axes at the appropriate one-dimensional ultimate stresses. This linear approximation underestimates the strength of the material and is therefore inscribed within the actual failure surface.

As an illustrative example, in Figure 4.4, adapted from Ref. [35], are given the failure surfaces in Compression - Shear plane, obtained by applying several different failure models (including the ones described in [40] and [41]). These failure surfaces are compared with the experimental data from [42].

The authors report that there are two primary failure modes inside a fiber reinforced plastic: a fiber mode in which the composite fails due to

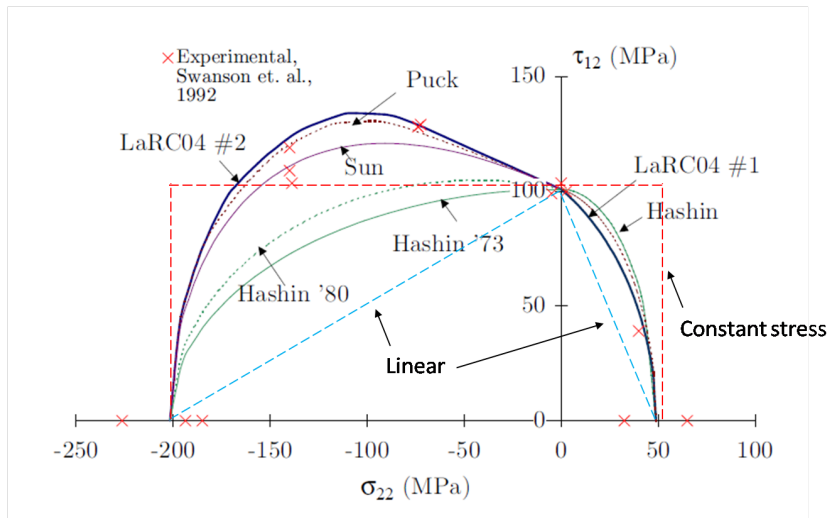


Figure 4.4: Failure envelopes and test data in Compression - Shear plane, for T800/3900-2 composite, from [35] and [42]

fiber rupture in tension or because of fiber buckling in compression and a matrix mode in which a plane crack parallel to the fibers occurs.

In Figure 4.5, the failure modes for the unidirectional ply due to stresses σ_1 , σ_2 , and τ_{12} are illustrated, [43]. When σ_1 is tensile the ply fails by failure of both the fibers and matrix, Figure 4.5a. For compression loading by σ_1 , the ply fails due to a fiber instability mode which often leads to broken fibers in a narrow zone (kink band) (Figure 4.5b). For any other applied stress, Figure 4.5c-e shows that the failure is governed by matrix and fiber/matrix interface failure and no broken fibers.

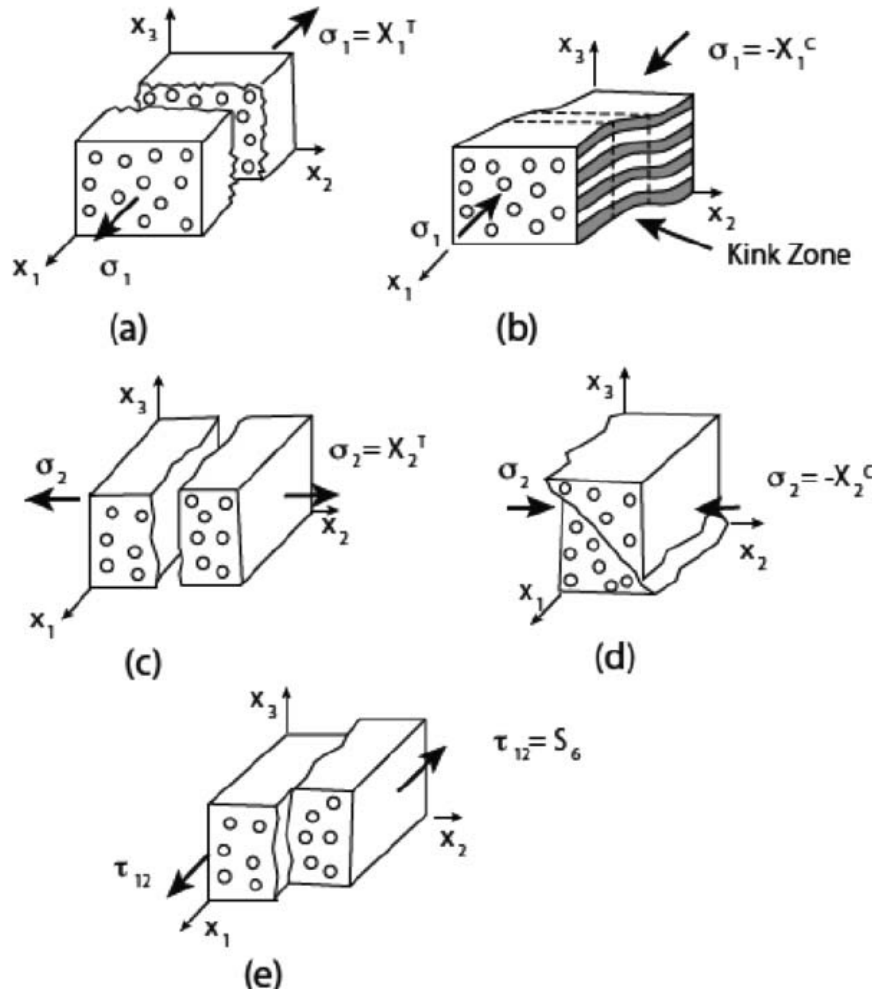


Figure 4.5: Failure modes of unidirectional composite under plane stress, from [43]

CHAPTER 5

Setup of Numerical Analysis using Abaqus Explicit

In this chapter the model set-up of the composite laminates using Abaqus is described. The definition of the geometry and the material properties is provided. The content of this chapter is mainly reported from Ref. [44], in which the background theory and the numerical implementation of composite laminates modelling is described in detail.

5.1 Model Setup

5.1.1 Model Geometry

The size of the modelled laminate has been chosen based on the height and the width of the fixing rig. The inner side of the fixing rig, which holds the specimen that needs to be impacted, is 90 mm high. The width of the modelled specimen is measured from the testing configuration, in which the width between the clamped edge to the free edge side was 26.5 mm.

This 26.5 mm \times 90 mm specimen was composed of 9 layers of 0.32 mm thick prepreg material. The layers of the laminate, which are modelled as 3D shell elements, were interchanged with layers of cohesive elements, modelled as 3D solid elements with thickness of 0.5×10^{-3} mm.

5.1.2 Model Materials and Properties

The names and the properties of the materials which are defined in Abaqus analysis are given in Table 5.1. The elastic properties, as well as the damage behaviour of the laminate material and of the cohesive material will be described in detail further in this chapter. The section properties, which are assigned to elements with different materials are also provided in the same table.

Material	Elastic Properties	Density	Damage Properties	Section Properties
Laminate	Lamina	1500 kg/m ³	Hashin damage	Shell homogeneous
Cohesive	Traction	10 ⁻⁶ kg/m ³	Quads damage	Cohesive
Steel	Isotropic	7890 kg/m ³	-	Solid homogeneous

Table 5.1: Overview of defined material and section properties in Abaqus

5.1.3 Building of the Laminate

The laminate is defined in the Abaqus assembly module using 9 layers of the pre-preg and 8 cohesive element layers. The shell property assigned to the laminae defines the thickness of each pre-preg layer of 0.32 mm. The laminate-cohesive layup is illustrated in Figure 5.1.

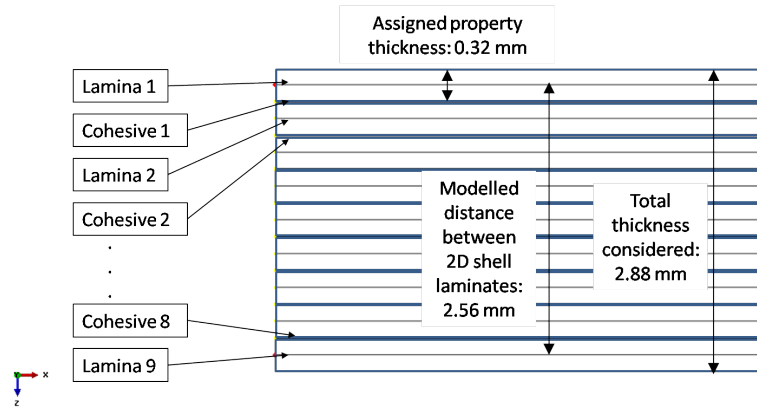


Figure 5.1: Assembly of the laminate in Abaqus

The layers of D shell laminae are connected with 3D solid cohesive elements using the surface-based tie constraint option in Abaqus. A surface-based tie constraint is used to make the translational and rotational motion as well as all other active degrees of freedom equal for a pair of surfaces. An additional constraint was defined on the impactor element, considering it as a rigid body. This rigid body is associated with a node, called the rigid body reference node, whose motion governs the motion of the entire rigid body. In the current analysis, this reference node is defined at the hemispherical impactor tip. The relative positions of the nodes and elements that are part of the rigid body remain constant throughout the simulation.

The contact between each ply of the laminate was modelled using the general contact algorithm, defining a tangential behaviour of the interface with the penalty friction formulation. The assumed friction coefficient is used to evaluate the shear stress τ of the surface traction with contact pressure p , which can be represented as $\tau = \mu p$ [47]. As reported in [47], the friction coefficient is mainly determined by the material property and the surface quality and it is defined as a function of fibre orientation. It varies from 0.2

for interfaces between two 0 degree plies to 0.8 for interfaces between two 90 degree plies. For the 0°/90° interfaces, a friction coefficient of 0.5 was assumed, [47].

Additional interaction property is defined between the first prepreg layer and the impactor element, using the tangential behaviour contact property, with the friction coefficient μ equal to 0.3, also reported in [47].

The definition of this contact property option in Abaqus is illustrated in Figure 5.2.

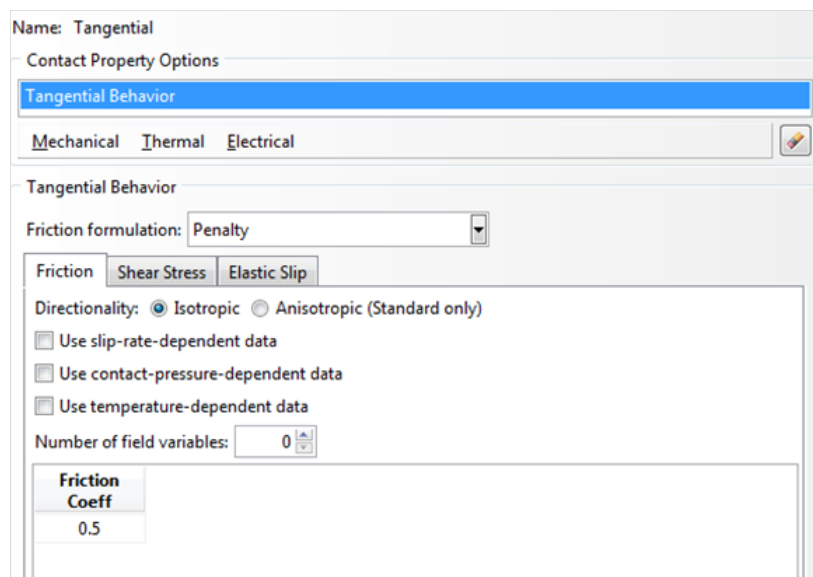


Figure 5.2: Contact property - tangential behaviour definition in Abaqus

5.1.4 Meshing of the Model

The type and number of elements used for the analysis is summarized in Table 5.2. The impacted area is modelled with a more refined mesh, with element size of 0.5 mm. The element shape used was “hex” element (for cohesive elements) and “quad” (for prepreg elements), both with “advancing front” meshing algorithm. The element shape used for the impactor was “tet” element.

Component	Element type	Number of elements	Number of nodes	Element size in impact area
Laminate	S4R	9724	9925	0.5 mm
Cohesive	COH3D8	9720	19842	0.5 mm
Impactor	C3D4	11524	2409	5mm

Table 5.2: Mesh attributes overview

5.1.5 Boundary Conditions and Loads

The boundary conditions which were introduced in the analysis corresponded to the tested configuration, in which the specimen was blocked inside the fixing rig on three sides, with one side free (where the near-edge impact is introduced, Figure 5.3, left). This blocking inside the fixing rig was simulated using the encastre boundary conditions, on the edges of the model, as indicated in Figure 5.3, right.

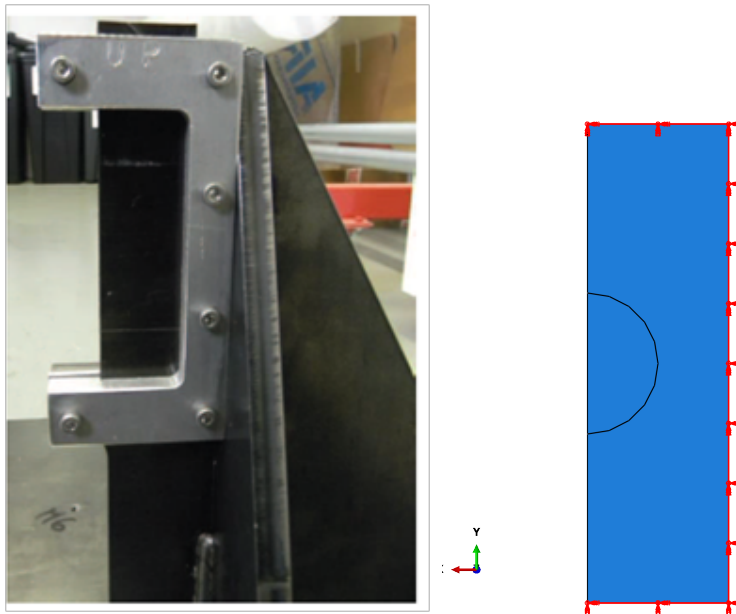


Figure 5.3: Specimen in impact test rig (left); FEM representation of the specimen (right)

Additional boundary conditions were defined on the impactor element,

defined, as already discussed, as a rigid body. The boundary conditions applied on its reference point allow the motion of the impactor in z direction only (perpendicular to the laminate plane). All other translations and rotations of the reference point are set to zero ($U_1=U_2=UR_1=UR_2=UR_3=0$, $U_3 \neq 0$).

5.2 Modelling of Composite Laminates

Considering the thin-walled nature of the aeronautical components, it can be assumed within reasonable accuracy that the CFRP structures of interest will be in the plane stress conditions. This loading condition allows using 3D shell elements, for which only the values of $E_1, E_2, \nu_{12}, G_{12}, G_{13}$ and G_{23} are required to define an orthotropic material, or a lamina. In all of the plane stress elements in Abaqus the surface is the surface of plane stress, so that the plane stress condition is $\sigma_{33} = 0$. The shear moduli G_{13} and G_{23} are included because they may be required for modelling transverse shear deformation in a shell. The Poissons ratio ν_{21} is implicitly given as $\nu_{21} = (E_2/E_1)\nu_{12}$. In this case the stress-strain relations for the in-plane components of the stress and strain are of the form:

$$\begin{Bmatrix} \epsilon_1 \\ \epsilon_2 \\ \gamma_{12} \end{Bmatrix} = \begin{bmatrix} 1/E_1 & -\nu_{12}/E_1 & 0 \\ -\nu_{12}/E_1 & 1/E_2 & 0 \\ 0 & 0 & 1/G_{12} \end{bmatrix} \begin{Bmatrix} \sigma_{11} \\ \sigma_{22} \\ \tau_{12} \end{Bmatrix}$$

The properties of the unidirectional prepreg which are used in the experimental campaign are extracted from the data provided by the fiber manufacturer (Toho Tenax, fiber UTS50 F13 12K) and by resin manufacturer (DeltaPreg, epoxy resin DT120) and by using the well-known textbook models for evaluation of mechanical properties of unidirectional composites: rule of mixtures and inverse rule of mixtures.

The rule of mixtures states that the mechanical properties in the fiber direction will be directly dependent on the weighted average of fiber and resin properties, based on their respective volume fractions. In the current work, a volume fraction of 50% for fibers and resin was assumed, which is

within lower ranges of typical commercially available prepregs (e.g. Hexcell reports in its data sheets a fiber volume of about 57%).

$$E_{1,prepreg} = fE_f + (1 - f)E_m$$

where

$$f = \frac{V_f}{V_f + V_m}$$

is the volume fraction of the fibers and E_f and E_m are the Young's moduli in the direction parallel to fibers.

For the investigated case, the fiber tensile modulus E_f is 246 GPa and the fiber tensile strength is 4.93 GPa, while the tensile modulus of the neat epoxy resin E_m is estimated, based on the data available in the literature, to be 4 GPa, with estimated tensile strength of 0.1 GPa. Similarly, the density of the prepreg can be calculated based on the rules of mixtures, and by knowing the density of the fibers $\rho_f = 1780\text{kg}/\text{m}^3$ and of the neat resin $\rho_m = 1220\text{kg}/\text{m}^3$.

In order to evaluate the tensile modulus in the direction perpendicular to the fiber, the inverse rule of mixtures was applied, which states:

$$E_{2,prepreg} = \left(\frac{f}{E_f} + \frac{1 - f}{E_m} \right)^{-1}$$

The prepreg properties obtained are given in Table 5.3.

The properties of the analysed laminate are compared with the ones available in the literature, given in Table 5.4 and 5.5, showing an overall similar data for the carbon fiber/epoxy laminates. The properties which were not available for the current investigation were assumed similar to the ones available in the open literature, basing this assumption on similar tensile strengths and moduli of reviewed carbon fiber/epoxy prepregs.

These properties were inserted in the Abaqus analysis using Material, Elastic, Laminate option, given in Figure 5.4. Unit consistent values are used for the analysis, using the SI units (kg, J, s, m).

Fiber tensile modulus [GPa]	246
Resin tensile modulus [GPa]	4
Prepreg tensile modulus E11 [GPa]	125
Prepreg tensile modulus E22 [GPa]	7.8
Fiber tensile strength [GPa]	4.92
Resin tensile strength [GPa]	0.1
Prepreg tensile strength [GPa]	2.51
Fiber density [kg/m ³]	1780
Resin density [kg/m ³]	1220
Prepreg density [kg/m ³]	1500

Table 5.3: Mechanical properties of the modelled laminate, assumed $V_f=50\%$

Material	HTA/6376C	HTS40/977-2	HTA/EH24
Reference	[45], [46]	[47], [48]	[49]
E11 [GPa]	145	153	143
E22 [GPa]	10.3	10.3	-
E33 [GPa]	12.1	10.3	-
G12 [GPa]	5.30	6	5.1
G13 [GPa]	5.27	6	-
G23 [GPa]	3.95	3.7	-
ν_{12}	0.301	0.3	0.29
ν_{13}	0.5	0.3	-
ν_{23}	0.495	0.4	-
Xt [MPa]	2000	2537	-
Xc [MPa]	1600	1580	-
Yt [MPa]	64	82	-
Yc [MPa]	290	236	-
S12 [MPa]	98	90	-
ρ [kg/m ³]	1590	1600	-

Table 5.4: Mechanical properties of carbon fiber/epoxy laminates from the literature, part 1

Material	XAS/913C	T300/977-2	UTS50/DT120
Reference	[50]	[51]	Current
E11 [GPa]	115	150	125
E22 [GPa]	8.5	11	7.8
E33 [GPa]	8.5	11	7.8
G12 [GPa]	4.5	6	-
G13 [GPa]	-	6	-
G23 [GPa]	-	3.7	-
ν_{12}	0.29	0.25	-
ν_{13}	0.29	0.25	-
ν_{23}	0.3	0.45	-
Xt [MPa]	-	2690	2510
Xc [MPa]	-	1580	-
Yt [MPa]	-	-	-
Yc [MPa]	-	-	-
S12 [MPa]	-	-	95.6
ρ [kg/m ³]	-	-	1500

Table 5.5: Mechanical properties of carbon fiber/epoxy laminates from the literature, part 2

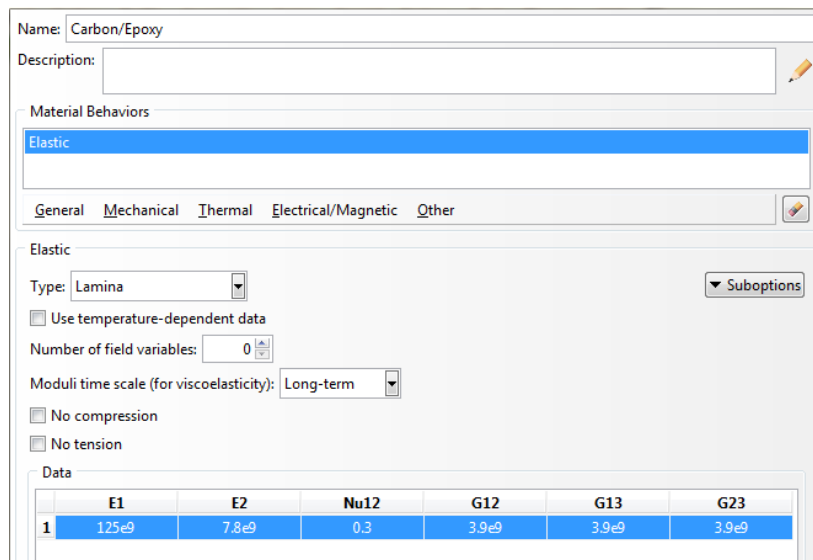


Figure 5.4: Definition of the elastic properties of the laminate in Abaqus

5.3 Modelling of Cohesive Elements

Abaqus has integrated in its elements library cohesive elements, used to model, among other structures, the behaviour of interfaces in composite materials. The modeling of these bonded interfaces in composite materials often involves situations where the intermediate glue material is very thin and for all practical purposes may be considered to be of zero thickness. In this case the macroscopic material properties are not relevant directly, and the analysis needs to use concepts derived from fracture mechanics, such as the amount of energy required to create new surfaces. The cohesive elements model the initial loading, the initiation of damage, and the propagation of damage leading to eventual failure at the bonded interface. The behaviour of the interface prior to initiation of damage is often described as linear elastic in terms of a penalty stiffness that degrades under tensile and/or shear loading but is unaffected by pure compression. The way the reduced stiffness is modelled in composite structures using models available in Abaqus is described in the next section.

The cohesive elements can be used in areas of the model where cracks are expected to develop. However, the precise locations, among all areas modeled with cohesive elements, where cracks initiate, as well as the evolution characteristics of such cracks, are determined as part of the solution. The cracks are restricted to propagate along the layer of cohesive elements and will not deflect into the surrounding material. In two-dimensional problems, such are the ones studied in this work, the traction-separation-based model assumes two components of separation: one normal to the interface and the other parallel to it.

Figure 5.5 demonstrates the geometrical features that are used to define cohesive elements. The connectivity of cohesive elements is like that of continuum elements, but they should be rather considered as being composed of two faces separated by a thickness. The relative motion of the bottom and top faces measured along the thickness direction represents opening or closing of the interface. The relative change in position of the bottom and top faces measured in the plane orthogonal to the thickness direction quantifies the transverse shear behavior of the cohesive element. Stretching

and shearing of the midsurface of the element are associated with membrane strains in the cohesive element. Figure 5.6 shows the different deformation modes of a cohesive element.

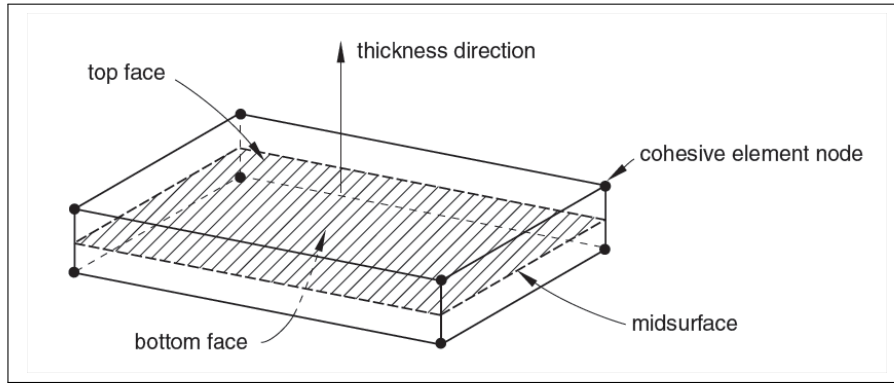


Figure 5.5: Spatial representation of a 3D cohesive element, reported from [44]

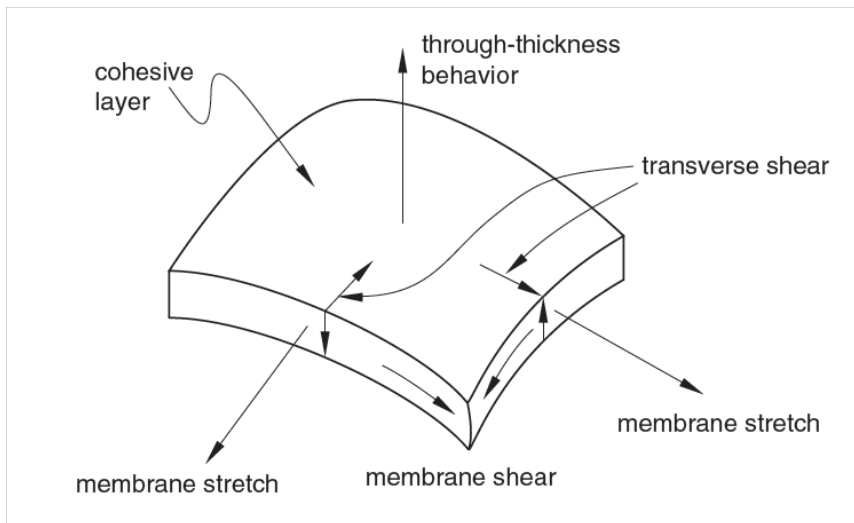


Figure 5.6: Deformation modes of a cohesive element, reported from [44]

The cohesive zone must be discretized with a single layer of cohesive elements through the thickness. If the cohesive zone represents an adhesive material with a finite thickness, the continuum macroscopic properties of this material can be used directly for modeling the constitutive response of the cohesive zone. Alternatively, if the cohesive zone represents an infinitesimally

thin layer of adhesive at a bonded interface, it may be more relevant to define the response of the interface directly in terms of the traction at the interface versus the relative motion across the interface.

At least one of either the top or the bottom face of the cohesive element must be constrained to another component. In most applications it is appropriate to have both faces of the cohesive elements tied to neighbouring components. When the mesh in the cohesive zone is not matched to the mesh of the adjacent components, cohesive elements can be tied to other components, using the tie constraint, which is the modelling strategy used in the current work.

The constitutive behaviour of the cohesive elements can be defined in terms of a material model provided in Abaqus. When cohesive elements are used in applications involving a finite-thickness adhesive, any available material model in Abaqus, including material models for progressive damage, can be used. For applications in which the behavior of cohesive elements is defined directly in terms of traction versus separation, the response can be defined only in terms of a linear elastic relation (between the traction and the separation) along with progressive damage. In the current work, the cohesive elements are used to model bonded interfaces where the interface thickness is negligibly small (matrix between layers of CFRP material), therefore the constitutive response of the cohesive layer is defined directly in terms of traction versus separation, as recommended by Abaqus manual, Ref. [44].

The following are the features of Cohesive behaviour defined directly in terms of a traction-separation law:

- It can be used to model the delamination at interfaces in composites directly in terms of traction versus separation
- It allows specification of material data such as the fracture energy as a function of the ratio of normal to shear deformation (mode mix) at the interface
- It assumes a linear elastic traction-separation law prior to damage
- It assumes that failure of the elements is characterized by progressive degradation of the material stiffness, which is driven by a damage

process

- It allows multiple damage mechanisms

The available traction-separation model in Abaqus assumes initially linear elastic behaviour, followed by the initiation and evolution of damage. The elastic behaviour is written in terms of an elastic constitutive matrix that relates the nominal stresses to the nominal strains across the interface. The nominal stresses are the force components divided by the original area at each integration point, while the nominal strains are the separations divided by the original thickness at each integration point. The default value of the original constitutive thickness is 1.0, if traction-separation response is specified, which ensures that the nominal strain is equal to the separation (i.e., relative displacements of the top and bottom faces). The constitutive thickness used for traction-separation response is typically different from the geometric thickness (which is typically close or equal to zero).

The nominal traction stress vector, t , consists of three components (two components in two-dimensional problems): t_n , t_s , and (in three-dimensional problems) t_t , which represent the normal (along the local 3-direction in three dimensions and along the local 2-direction in two dimensions) and the two shear tractions (along the local 1- and 2-directions in three dimensions and along the local 1-direction in two dimensions), respectively. The corresponding separations are denoted by δ_n , δ_s , and δ_t . Denoting by T_o the original thickness of the cohesive element, the nominal strains can be defined as:

$$\epsilon_n = \frac{\delta_n}{T_o}, \epsilon_s = \frac{\delta_s}{T_o}, \epsilon_t = \frac{\delta_t}{T_o}$$

The elastic behaviour can then be written as:

$$t = \begin{Bmatrix} t_n \\ t_s \\ t_t \end{Bmatrix} = \begin{bmatrix} K_{nn} & K_{ns} & K_{nt} \\ K_{ns} & K_{ss} & K_{st} \\ K_{nt} & K_{st} & K_{tt} \end{bmatrix} \begin{Bmatrix} \epsilon_n \\ \epsilon_s \\ \epsilon_t \end{Bmatrix} = \mathbf{K}\epsilon$$

The elasticity matrix provides fully coupled behaviour between all components of the traction vector and separation vector and can depend on temperature and/or field variables.

Abaqus/Explicit allows modelling of progressive damage and failure in cohesive layers whose response is defined in terms of traction-separation. Damage of the traction-separation response allows the combination of several damage mechanisms acting simultaneously on the same material. Each failure mechanism consists of three ingredients: a damage initiation criterion, a damage evolution law, and a choice of element removal (or deletion) upon reaching a completely damaged state.

The initial response of the cohesive element is assumed to be linear. However, once a damage initiation criterion is met, material damage can occur according to a user-defined damage evolution law.

Figure 5.7 shows a typical traction-separation response with a failure mechanism. If the damage initiation criterion is specified without a corresponding damage evolution model, Abaqus will evaluate the damage initiation criterion for output purposes only; there is no effect on the response of the cohesive element (i.e., no damage will occur). The cohesive layer does not undergo damage under pure compression.

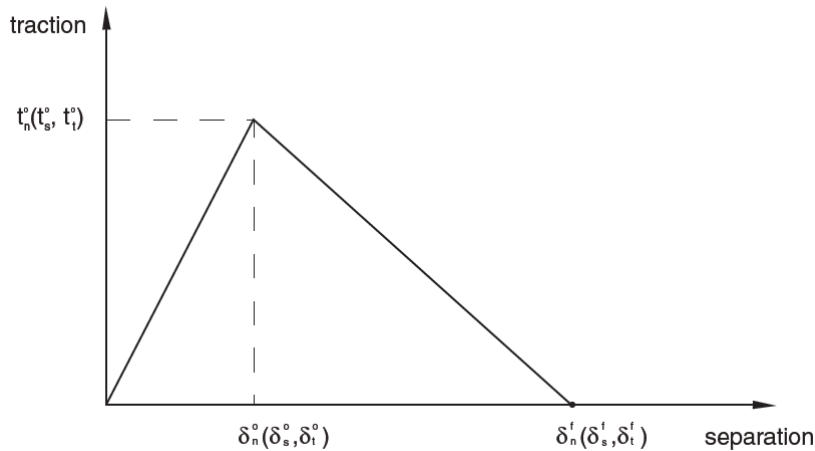


Figure 5.7: Typical traction-separation response, reported from [44]

Damage initiation refers to the beginning of degradation of the response of a material point. The process of degradation begins when the stresses and/or strains satisfy certain specified damage initiation criteria. Each damage initiation criterion also has an output variable associated with it to indicate whether the criterion is met. A value of 1 or higher indicates that

the initiation criterion has been met.

In the current work, the Quadratic nominal stress damage criterion has been applied. In this case, the damage is assumed to initiate when a quadratic interaction function involving the nominal stress ratios reaches a value of one. This criterion can be represented as:

$$\left\{ \frac{\langle t_n \rangle}{t_n^o} \right\}^2 + \left\{ \frac{t_s}{t_s^o} \right\}^2 + \left\{ \frac{t_t}{t_t^o} \right\}^2 = 1$$

Where t_n^o , t_s^o and t_t^o represent the peak values of the nominal stress when the deformation is either purely normal to the interface or purely in the first or the second shear direction, respectively. The symbol $\langle \rangle$ is used to signify that a pure compressive deformation or stress state does not initiate damage.

The damage evolution law describes the rate at which the material stiffness is degraded once the corresponding initiation criterion is reached. A scalar damage variable, D , represents the overall damage in the material and captures the combined effects of all the active mechanisms. It initially has a value of 0. If damage evolution is modelled, D monotonically evolves from 0 to 1 upon further loading after the initiation of damage. The stress components of the traction-separation model are affected by the damage according to:

$$t_n = \begin{cases} (1 - D)\bar{t}_n, & \bar{t}_n \geq 0 \\ \bar{t}_n, & \text{otherwise (no damage to compressive stiffness)} \end{cases}$$

$$t_s = (1 - D)\bar{t}_s$$

$$t_t = (1 - D)\bar{t}_t$$

where \bar{t}_n , \bar{t}_s and \bar{t}_t are the stress components predicted by the elastic traction-separation behaviour for the current strains without damage.

The mode mix of the deformation fields in the cohesive zone quantifies the relative proportions of normal and shear deformation. The energy based mode mix is the one chosen for the current analysis.

Figure 5.8 is a schematic representation of the dependence of damage initiation and evolution on the mode mix, for a traction-separation response with isotropic shear behaviour. The figure shows the traction on the vertical axis and the magnitudes of the normal and the shear separations along the two horizontal axes. The unshaded triangles in the two vertical coordinate planes represent the response under pure normal and pure shear deformation, respectively. All intermediate vertical planes (that contain the vertical axis) represent the damage response under mixed mode conditions with different mode mixes. The dependence of the damage evolution data on the mode mix can be defined either in tabular form or, in the case of an energy-based definition, analytically.

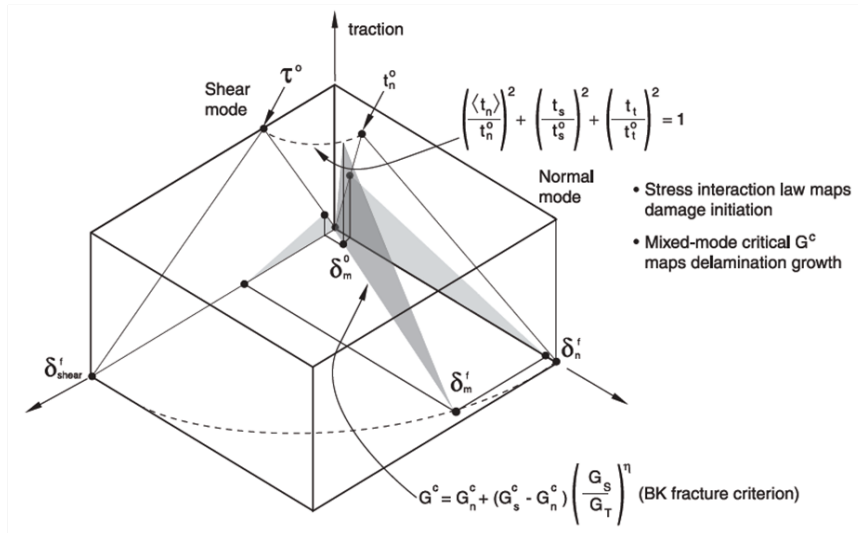


Figure 5.8: Illustration of mixed-mode response in cohesive elements, reported from [44]

Damage evolution can be defined based on the energy that is dissipated as a result of the damage process, also called the fracture energy. The fracture energy is equal to the area under the traction-separation curve. The fracture energy is specified in Abaqus as a material property and an exponential softening behaviour has been selected in the current work. The dependence of the fracture energy on the mode mix is specified by using the analytical BK (Benzeggagh Kenane) form, Ref. [54]. The definition of the fracture energy as a function of the mode mix using the analytical BK fracture criterion is

the following:

$$G_n^C + (G_s^C - G_n^C) \frac{G_s^\eta}{G_T} = G^C$$

Where $G_S = G_s + G_t$, $G_T = G_n + G_S$, and η is a material parameter. In Abaqus, G_n^C , G_s^C and η must be specified.

Additional parameter that needs to be defined when modelling with cohesive elements is its thickness. The characteristic element length of a cohesive element is equal to its constitutive thickness. If the geometric thickness of the cohesive element is very small compared to its surface dimensions, the thickness computed from the nodal coordinates may be inaccurate. In such cases it is possible to specify a constant thickness directly when defining the section properties of these elements.

When the response of the cohesive elements is based on a traction-separation approach, Abaqus assumes by default that the constitutive thickness is equal to one. This default value is motivated by the fact that the geometric thickness of cohesive elements is often equal to (or very close to) zero for the kinds of applications in which a traction-separation-based constitutive response is appropriate. This default choice ensures that nominal strains are equal to the relative separation displacements. It is possible, however, to override this default value by specifying another value or specifying that the constitutive thickness should be equal to the geometric thickness.

The properties of the interface between the carbon fiber prepreg plies were taken from the open literature, usually reported together with the properties of the carbon fiber/epoxy lamina.

The data that needs to be provided for the delamination analysis after impact is relative to the thickness of the cohesive layer, fracture toughness of the interface, elastic properties of the cohesive layer and its density. The thickness of the cohesive layer in the case of composite laminate modelling is indeed close to zero, so the assumed thickness in the Abaqus model was 0.005 mm.

The elastic modulus assigned to the cohesive zone element is normalised by its thickness when introduced in Abaqus. This elastic modulus is usually referred to as an arbitrary initial penalty stiffness (denoted as K) which is

defined in different ways in the literature. According to Ref. [51], K assumes the value of $10^9 N/m$. Alternatively, according to Ref. [52] this value is close to the ratio of the adjacent ply stiffness in thickness direction, E_{33} , and the assumed thickness of the cohesive layer, so $K_I = E_{33}/t$. Similarly, for shear modulus, $K_{II}=G_{12}/t$.

Given the properties used for the current numerical analysis (see Table 5.5 and Figure 5.4) the normalized stiffness assumes the value of :

$$K_I = \frac{7.8GPa}{5 \times 10^{-6}m} = 1.57 \times 10^{15}[N/m]$$

$$K_{II} = K_{III} = \frac{3.9GPa}{5 \times 10^{-6}m} = 0.78 \times 10^{15}[N/m]$$

For the current analysis, the interface data were taken from Ref. [47] and presented in Table 5.6. As already mentioned previously in the text, the Quadratic nominal stress damage criterion has been applied, for which peak normal and shear stress values need to be defined, as well as the fracture energy necessary for the definition of the damage evolution. The BK model for damage evolution was applied, with the value $\eta = 1.45$, based on the data presented in [51].

	Normal Mode	Shear Mode First Direction	Shear Mode Second Direction
Normalised elastic modulus $\times 10^{15}$ [N/m]	1.57	0.78	0.78
Inter-laminar strength [MPa]	62.3	92.3	92.3
Inter-laminar fracture energy [J/m ²]	280	790	790

Table 5.6: Material parameters of the cohesive elements

The way these material parameters are introduced in Abaqus analysis are illustrated in Figure 5.9 and 5.10.

Name: Cohesive

Description:

Material Behaviors

Quads Damage

Damage Evolution

General Mechanical Thermal Electrical/Magnetic Other

Quads Damage

Direction relative to local 1-direction (for XFEM): Normal Parallel

Tolerance: 0.05

Use temperature-dependent data

Number of field variables: 0

	Nominal Stress Normal-only Mode	Nominal Stress First Direction	Nominal Stress Second Direction
1	62.3e6	92.3e6	92.3e6

Figure 5.9: Input definition for Quadratic nominal stress damage criterion in Abaqus

5.4 Modelling of Damage and Failure of fiber-reinforced materials

The description of the damage model given in this section is reported from Abaqus manual, [44] in which the Abaqus implementation of the Hashin-Rotem model, introduced in Chapter 4.1.6, is explained in more detail.

Abaqus offers a damage model enabling to predict the onset of damage and to model damage evolution for elastic-brittle materials with anisotropic behavior, such as fiber-reinforced materials.

Damage is characterized by the degradation of material stiffness and the damage model requires specification of the following:

- the undamaged response of the material, which must be linearly elastic
- a damage initiation criterion
- a damage evolution response, including a choice of element removal

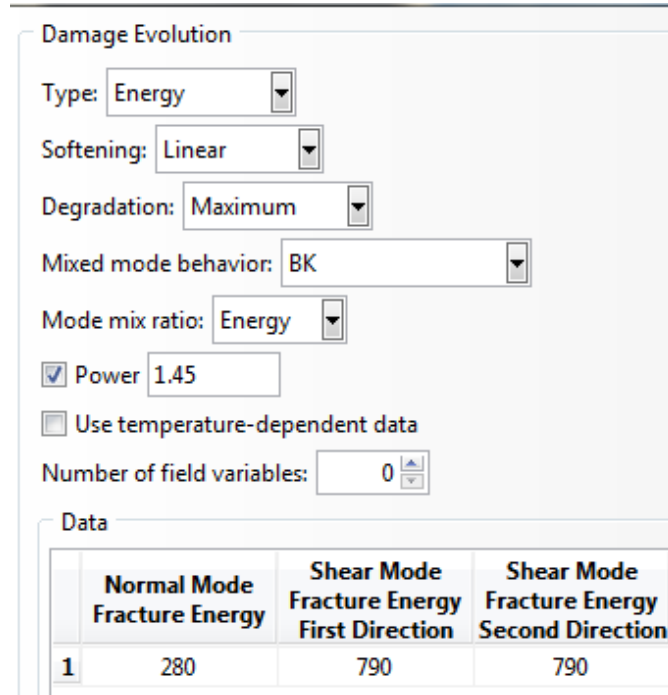


Figure 5.10: Definition of damage evolution in cohesive elements in Abaqus using BK criterion

The Abaqus anisotropic damage model is based on the work reported in Refs. [40], [41], [55] and [51].

Four different modes of failure are considered:

- fiber rupture in tension
- fiber buckling and kinking in compression
- matrix cracking under transverse tension and shearing
- matrix crushing under transverse compression and shearing

The onset of damage is determined by the initiation criteria proposed in Ref. [40] and [41], in which the failure surface is expressed in the effective stress space (the stress acting over the area that effectively resists the force).

These criteria consider four different damage initiation mechanisms: fiber tension, fiber compression, matrix tension, and matrix compression. The initiation criteria have the following general forms:

Fiber tension ($\hat{\sigma}_{11} \geq 0$):

$$F_f^t = \left(\frac{\hat{\sigma}_{11}}{X^T} \right)^2 + \alpha \left(\frac{\hat{\tau}_{12}}{S^L} \right)^2$$

Fiber compression ($\hat{\sigma}_{11} < 0$):

$$F_c^t = \left(\frac{\hat{\sigma}_{11}}{X^C} \right)^2$$

Matrix tension ($\hat{\sigma}_{22} \geq 0$):

$$F_m^t = \left(\frac{\hat{\sigma}_{22}}{Y^T} \right)^2 + \left(\frac{\hat{\tau}_{12}}{S^L} \right)^2$$

Matrix compression ($\hat{\sigma}_{22} < 0$):

$$F_m^c = \left(\frac{\hat{\sigma}_{22}}{2S^T} \right)^2 + \left[\left(\frac{Y^C}{2S^T} \right)^2 - 1 \right] \frac{\hat{\sigma}_{22}}{Y^C} + \left(\frac{\hat{\tau}_{12}}{S^L} \right)^2$$

In the above equations

X^T denotes the longitudinal tensile strength

X^C denotes the longitudinal compressive strength

Y^T denotes the transverse tensile strength

Y^C denotes the transverse compressive strength

S^L denotes the longitudinal shear strength

S^T denotes the transverse shear strength

α is a coefficient that determines the contribution of the shear stress to the fiber tensile initiation criterion

$\hat{\sigma}_{11}, \hat{\sigma}_{22}, \hat{\tau}_{12}$ are components of the effective stress tensor, $\hat{\sigma}$, that is used to evaluate the initiation criteria and which is computed from:

$$\hat{\sigma} = \mathbf{M}\sigma$$

where σ is the true stress and \mathbf{M} is the damage operator:

$$\mathbf{M} = \begin{bmatrix} \frac{1}{(1-d_f)} & 0 & 0 \\ 0 & \frac{1}{(1-d_m)} & 0 \\ 0 & 0 & \frac{1}{(1-d_s)} \end{bmatrix}$$

d_f , d_m and d_s are internal damage variables that characterize fiber, matrix and shear damage, which are derived from damage variables d_f^t , d_f^c , d_m^t and d_m^c , corresponding to the four, previously discussed modes:

$$d_f = \begin{cases} d_f^t & \text{if } \hat{\sigma}_{11} \geq 0 \\ d_f^c & \text{if } \hat{\sigma}_{11} < 0 \end{cases}$$

$$d_m = \begin{cases} d_m^t & \text{if } \hat{\sigma}_{22} \geq 0 \\ d_m^c & \text{if } \hat{\sigma}_{22} < 0 \end{cases}$$

$$d_s = 1 - (1 - d_f^t)(1 - d_f^c)(1 - d_m^t)(1 - d_m^c)$$

Prior to any damage initiation and evolution the damage operator, \mathbf{M} , is equal to the identity matrix, so $\hat{\sigma} = \sigma$. Once damage initiation and evolution has occurred for at least one mode, the damage operator becomes significant in the criteria for damage initiation of other modes.

The damage initiation criteria presented above can be specialized to obtain the model proposed in Ref. [40] by setting $\alpha = 0.0$ and $S^T = Y_C/2$ or the model proposed in Ref. [41] by setting $\alpha = 1.0$.

An output variable is associated with each initiation criterion (fiber tension, fiber compression, matrix tension, matrix compression) to indicate whether the criterion has been met. A value of 1.0 or higher indicates that the initiation criterion has been met. If additionally, a damage evolution model is defined, maximum value of this variable does not exceed 1.0. However, if a damage evolution model is not defined, this variable can have values higher than 1.0, which indicates by how much the criterion has been exceeded.

The response of the material in which the damaging has occurred can be calculated from:

$$\sigma = C_d \epsilon$$

where ϵ is the strain and C_d is the elasticity matrix, which reflects any damage and has the form

$$\mathbf{C}_d = \frac{1}{D} \begin{bmatrix} (1 - d_f)E_1 & (1 - d_f)(1 - d_m)\nu_{21}E_1 & 0 \\ (1 - d_f)(1 - d_m)\nu_{12}E_2 & (1 - d_m)E_2 & 0 \\ 0 & 0 & (1 - d_s)GD \end{bmatrix}$$

where:

$$D = 1 - (1 - d_f)(1 - d_m)\nu_{12}\nu_{21}$$

d_f reflects the current state of fiber damage

d_m reflects the current state of matrix damage

d_s reflects the current state of shear damage

E_1 is the Youngs modulus in the fiber direction

E_2 is the Youngs modulus in the direction perpendicular to the fibers

G is the shear modulus

ν_{12} and ν_{21} and are Poissons ratios

The evolution of the elasticity matrix due to damage for fiber-reinforced materials is therefore described in Abaqus as follows:

- It assumes that damage is characterized by progressive degradation of material stiffness, leading to material failure
- It requires linearly elastic behavior of the undamaged material
- It takes into account four different failure modes: fiber tension, fiber compression, matrix tension, and matrix compression
- It uses four damage variables to describe damage for each failure mode
- It must be used in combination with Hashins damage initiation criteria
- It is based on energy dissipation during the damage process

Abaqus introduces the concept of the specific length in the calculation of the damage evolution, allowing to present the damage using the stress-displacement behaviour. The damage variable will evolve such that the stress-displacement behaves as shown in Figure5.11 in each of the four failure modes. The positive slope of the stress-displacement curve prior to damage initiation corresponds to linear elastic material behavior; the negative slope

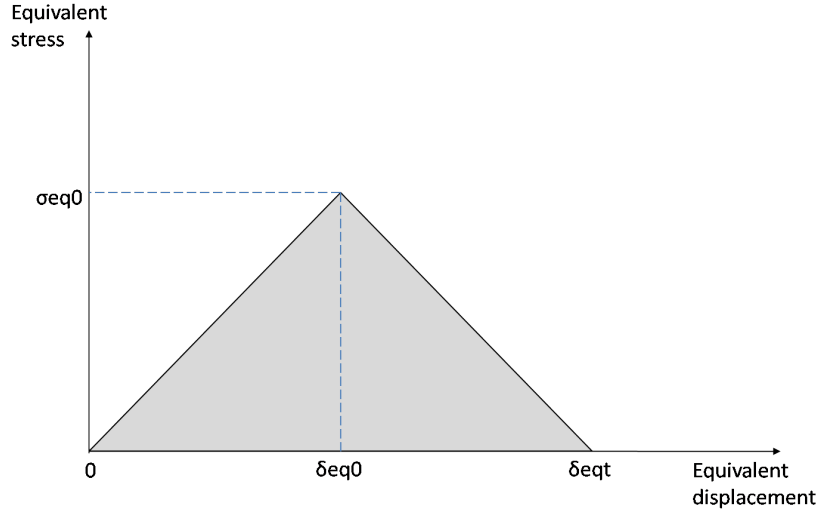


Figure 5.11: Equivalent stress versus equivalent displacement, reported from [44]

after damage initiation is achieved by evolution of the respective damage variables according to the equations shown below.

Equivalent displacement and stress for each of the four damage modes are defined as follows:

Fiber tension ($\hat{\sigma}_{11} \geq 0$):

$$\delta_{eq}^{ft} = L^c \sqrt{\langle \epsilon_{11} \rangle^2 + \alpha \epsilon_{12}^2}$$

$$\sigma_{eq}^{ft} = \frac{\langle \sigma_{11} \rangle \langle \epsilon_{11} \rangle + \alpha \tau_{12} \epsilon_{12}}{\delta_{eq}^{ft} / L^c}$$

Fiber compression ($\hat{\sigma}_{11} < 0$):

$$\delta_{eq}^{fc} = L^c \langle -\epsilon_{11} \rangle$$

$$\sigma_{eq}^{fc} = \frac{\langle -\sigma_{11} \rangle \langle -\epsilon_{11} \rangle}{\delta_{eq}^{fc} / L^c}$$

Matrix tension ($\hat{\sigma}_{22} \geq 0$):

$$\delta_{eq}^{mt} = L^c \sqrt{\langle \epsilon_{22} \rangle^2 + \epsilon_{12}^2}$$

$$\sigma_{eq}^{mt} = \frac{\langle \sigma_{22} \rangle \langle \epsilon_{22} \rangle + \tau_{12} \epsilon_{12}}{\delta_{eq}^{mt} / L^c}$$

Matrix compression ($\hat{\sigma}_{22} < 0$):

$$\delta_{eq}^{mc} = L^c \sqrt{\langle -\epsilon_{22} \rangle^2 + \epsilon_{12}^2}$$

$$\sigma_{eq}^{mc} = \frac{\langle -\sigma_{22} \rangle \langle -\epsilon_{22} \rangle + \tau_{12} \epsilon_{12}}{\delta_{eq}^{mc} / L^c}$$

The characteristic length, L^c , is based on the element geometry and formulation. For and shell elements it is a characteristic length in the reference surface, computed as the square root of the element area. The symbol $\langle \rangle$ is an operator, defined as $\langle \alpha \rangle = (\alpha + |\alpha|) / 2$.

In the setup of the current model, the damage initiation part was of interest for the analysis, and all the values higher than 1.0 coming from the output results when using Hashin criteria were considered as damaged. This was of particular interest when trying to determine the damaged area of the matrix directly under the impactor. As presented in the open literature [47], [53], it is the matrix plasticity that governs the creation of permanent indentations. The hypothesis brought forward in this analysis is that the matrix tension damage is a good indicator of the area in which the permanent indentation can occur. This is discussed more in detail in Chapter 6.

The input data which are necessary to be inserted in the Abaqus analysis in order to define the Hashin damage initiation criterion are already illustrated in Table 5.4 and 5.5. From these tables, the typical mechanical properties of the carbon fiber/epoxy prepreg were extracted and assumed applicable for the currently analysed configuration.

Figure 5.12 gives an overview on how these data are inserted in Abaqus as Hashin damage initiation criterion. Parameter Alpha has been set to 1, corresponding to the Hashin criterion from paper [41].



Figure 5.12: Definition of Hashin damage initiation criterion in Abaqus

5.5 Running of the Analysis

The analysis was carried out using a default initial step, used for definition of boundary conditions and initial predefined fields - velocity and one analysis step, in which the impact event is simulated. The duration of the impact event of 0.008 s was selected based on results measured with the accelerometer, described in Chapter 3.

CHAPTER 6

Numerical Results

To understand the numerical results presented in this chapter it is necessary to illustrate the main goal of the current work. Given the nature of composite structures, finding and assessing damages is not an easy task and it requires both time and special inspections. For this reason it is imperative for the aeronautical industry to develop methods to speed up the composite material inspections and to make them as standard and safe as possible.

From this consideration the idea of the developed numerical model was born. The main goal of this numerical work is that to have a model which is capable of predicting the delamination size and hence the residual static strength of the damaged structure simply from the indentation left on the surface.

The model developed in this work is only an initial step of a much bigger effort which is necessary in order to obtain a complete and solid numerical model, which could be used in real life application. Indeed, considering the vast variety of laminate stacking sequences and orientation angles, a reliable numerical model which could be used in every situation would come a long way in reducing the need of extensive and costly experimental campaigns. The final result would be to use the proposed model for the creation of a damage mapping for the complete composite made aircraft structure.

The numerical models presented in this chapter are developed using Abaqus Explicit and created using 3D shell and 3D cohesive elements. The results of near edge impacts are presented and a correlation between the size and shape of impacted area with the delamination area is assumed. This assumptions is based on data presented in [56] and it is adapted by considering the Hashin matrix compression damage initiation criterion as an index of the size of surface indentation and, as a consequence, of a delamination present in a composite structure.

The contents of this chapter are based on data presented in:

V. Ristori, E. Troiani, M.P. Falaschetti, G. Ivetic, Damage Tolerance in CFRP Structures - Numerical and Experimental Analysis of Low Energy Near Edge Impacts, Abstract accepted, 29th Symposium of the International Committee on Aeronautical Fatigue, Nagoya, Japan, June 2017.

6.1 Numerical output

The comparison of the obtained numerical results with the experimental data is illustrated in this chapter. This comparison is necessary in order to understand if the modelling assumptions considered during the analysis are valid and if the developed model is indeed validated for the investigated configuration.

6.1.1 Impact energy level

Based on the data presented in Table 3.7, a comparison between the energy history following an impact event between the experimentally measured data and the data obtained using the numerical model described in detail in Chapter 5 is illustrated in Figure 6.1. It can be observed that the numerically obtained residual energy is of slightly higher magnitude than the experimentally measured data. Based on the data presented in the literature [47], an inverse trend after the rebound of the impactor was reported, in which the experimentally measured values were slightly higher than the numerical results. This difference was explained by the inaccuracy in modelling of the rebound phase of the impact, which might lead to inaccuracy in the final value of energy absorbed. However, it is important to remember that the material data used for the modelling itself is composed of a large number of interdependent variables and that exact capturing of experimental data is often difficult, if not even impossible.

In Figure 6.2 the contact force plot has been provided, between the impactor and the first ply of the laminate. Considering that the contact occurs by translation of the impactor in z-direction only, the force resultant, illustrated in the image, corresponds to the z-component of the force. The entity of this force at its peak is 1670 N, and this value is in relatively good correspondence with the experimentally measured contact force, for which accelerometer data on maximum acceleration (Table 3.1) was used together with the known mass of the impactor.

The measured force was calculated as:

$$\text{Maximum contact force} = 1.817 \text{ [kg]} \times 74.7 \times 9.81 \text{ m/s}^2 = 1331 \text{ [N]}$$

It is important to highlight that the specimen used used for impact

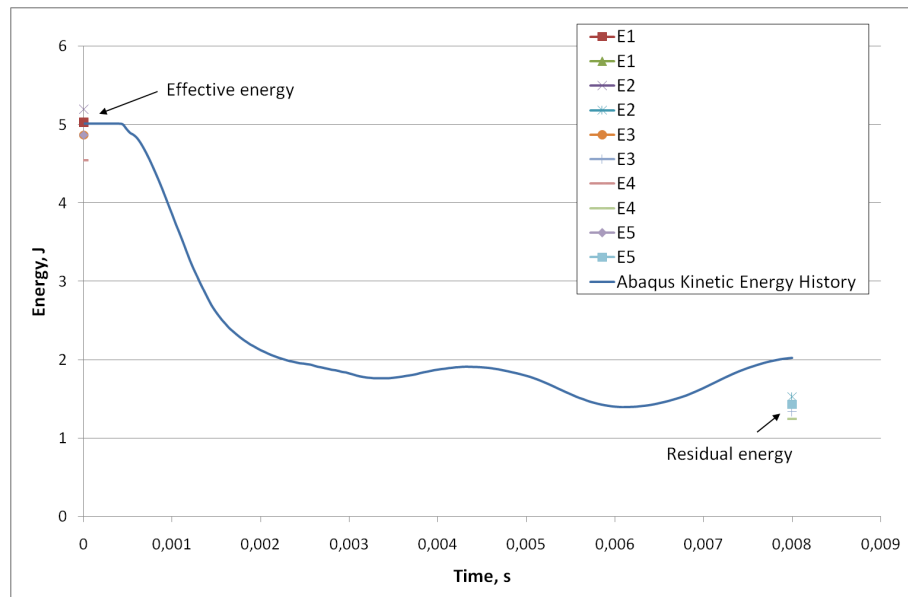


Figure 6.1: Comparison between Abaqus numerical and experimental results

tests with accelerometer readings was the one from the first experimental campaign used for calibration of the experimental equipment, while the modelled specimen corresponds to the one from the second experimental campaign.

Using classical laminate theory considerations, it was possible to estimate the flexural stiffness of the two laminates. Open source program eLamX² [57], was used for this calculation.

The comparison shows that stiffness of the laminate from the first experimental campaign is approximately 10% lower than the one used for the second experimental campaign (and modelled numerically).

Considering the 10% higher stiffness of the numerically analysed laminate, the numerical result of 1670 N and experimental result of 1331 N can be more easily correlated.

So, it was considered acceptable to make comparisons between the experimental and numerical results, even if there are based on two different investigated laminates.

Besides the peak impact force value obtained numerically or experimentally, it is important to observe the results in the force history diagram,

presented in Figure 6.3. Even if there is a reasonably good correlation of the calculated peak stress, the time shift in the occurrence of this value is clearly visible. It is important to remember, though, that we are dealing with relatively small time scales (order of magnitude of milliseconds), so such a shift could be explained with small variations in laminate stiffness that could cause the seemingly large differences in results. It would be possible to additionally calibrate the material parameters of the laminate in order to match more closely the experimentally observed behaviour, but, as previously mentioned, the large number of interdependent variables does not allow to change, even within physically reasonable ranges, the material parameters which would capture one observed behaviour of the structure, without influencing other aspects of the analysis which are also of interest in current work.

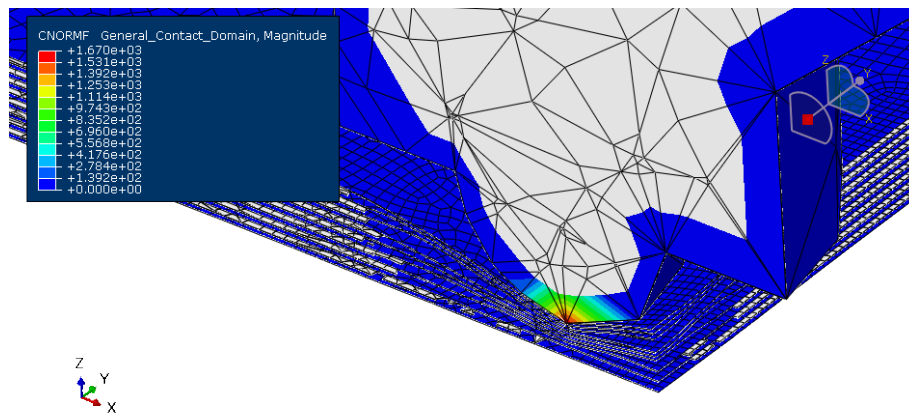


Figure 6.2: Maximum contact force between the impactor and the laminate

The maximum displacement which was measured experimentally for the impact energy level of 5 J was -4.39 mm, Table 3.1. The result of the numerical analysis provides a similar value, the maximum displacement, present at the impacting position is of -4.05 mm, and it occurs at the 0.006 s analysis step time, while the experimentally measured maximum displacement occurred instances after the maximum measured acceleration, at about 0.004 seconds after the initiation of the contact. The numerically calculated displacement plot, in the impacting direction (z-direction in the plot) is illustrated in Figure 6.4. This difference in displacements needs also

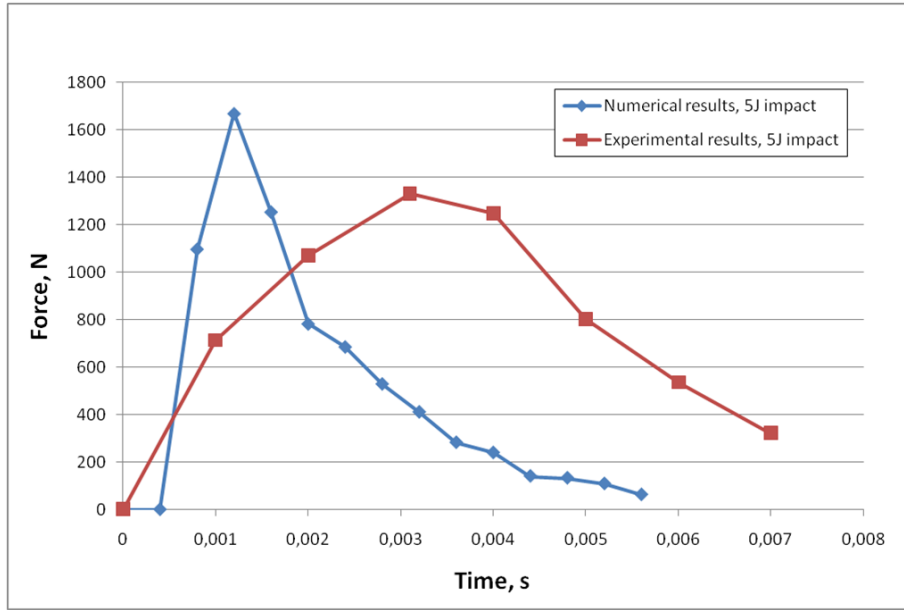


Figure 6.3: Impact force vs. time for numerical and experimental analysis

the be observed considering already mentioned difference in flexural stiffness between the experimental measurement and numerical data.

An overall conclusion is that the numerically obtained data is able to capture within engineering accuracy the behaviour of the impacted structure.

6.1.2 Delamination

Based on the good correlation between experimental and numerical results concerning the energy levels (see previous paragraph), the hypothesis that the delamination analysis results of the same model correspond sufficiently to the real structure is put forward. In order to validate this hypothesis, open literature data was used as a basis, coming from [47]. By using the same model setup described in detail in Chapter 5, the geometry, loading and boundary conditions from [47] were re-run and the obtained results indeed match sufficiently the ones reported in the article [47], as illustrated in Figure 6.5.

As visible in Figure 6.5 despite the coarse mesh used, the obtained numerical delamination matches within engineering accuracy the experimental one. This run served as a validation of the used numerical model, showing that it

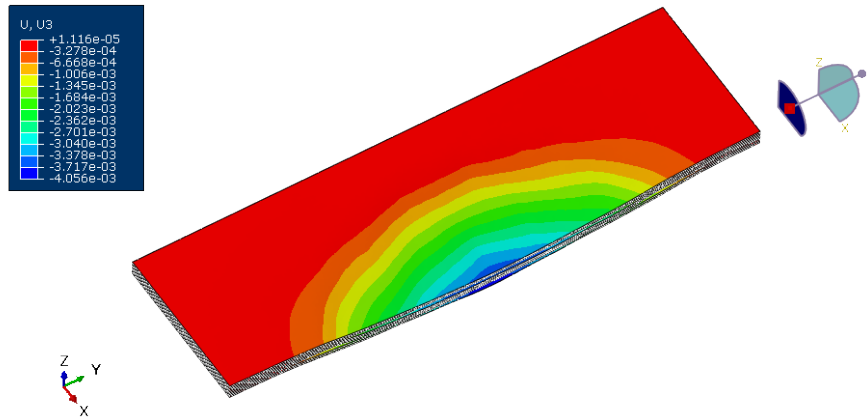


Figure 6.4: Displacement plot in impacting direction

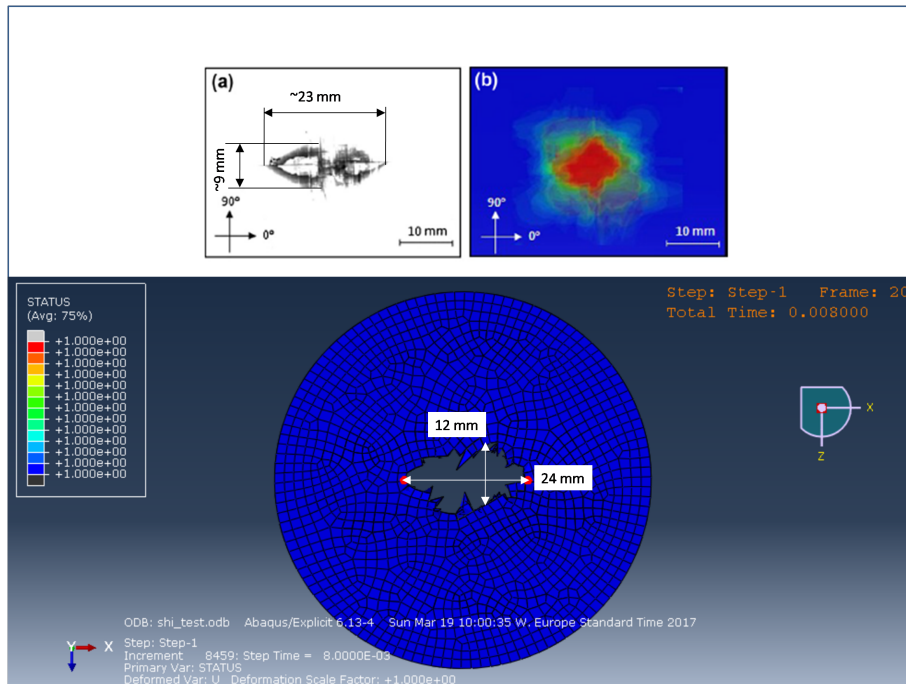


Figure 6.5: Delaminations results - top [47]: a) - experimental x-ray radiograph, b) numerical; bottom: obtained using the current model

is able to predict with sufficient accuracy the delaminations introduced in the composite structure after an impact event.

6.2 Delamination size

In this chapter, the numerical results relative to the observed delamination in the analysed specimens are presented. The results are given for the experimentally analysed configurations, visible in Figure 3.34. In order to assess more easily the delaminated surface between each lamina, the cohesive layer was, for this purpose only, additionally meshed with a uniformly sized mesh, with specific size of 0.45 mm. What this meshing approach allows is to estimate the total delaminated area based on the number of deactivated cohesive elements only. In fact, one of the outputs of Abaqus analysis is the STATUS result, which indicates the still active cohesive elements with 1 (no delamination) and the deactivated ones with 0 (delamination occurred). By simply multiplying the number of delaminated elements with the area of a single element, it was possible to estimate the delamination size between each lamina, and to compare these delaminations for different impact energy levels and boundary conditions. These comparisons are presented in Table 6.1- 6.3.

5J impact, delamination area [mm ²]		
Cohesive layer	Near Edge	Central
1	797	921
2	933	891
3	1118	1069
4	1059	925
5	1086	871
6	1287	1002
7	1252	893
8	534	551

Table 6.1: Delamination area for 5J impact for each lamina interface, near edge vs. central

The Abaqus plots showing the delaminated area at the end of the analysis, for different energy levels and impact positions are given in Figure 6.6 to 6.9. These plots are relative to delamination data provided in Table 6.1 and 6.2.

3J impact, delamination area [mm ²]		
Cohesive layer	Near Edge	Central
1	675	787
2	756	769
3	920	810
4	884	793
5	824	774
6	967	812
7	879	726
8	482	441

Table 6.2: Delamination area for 3J impact for each lamina interface, near edge vs. central

Energy [J]	Position	Delamination area [mm ²]
3	Near Edge	798
3	Central	739
5	Near Edge	1008
5	Central	890

Table 6.3: Average delamination area for different energy levels and impact positions

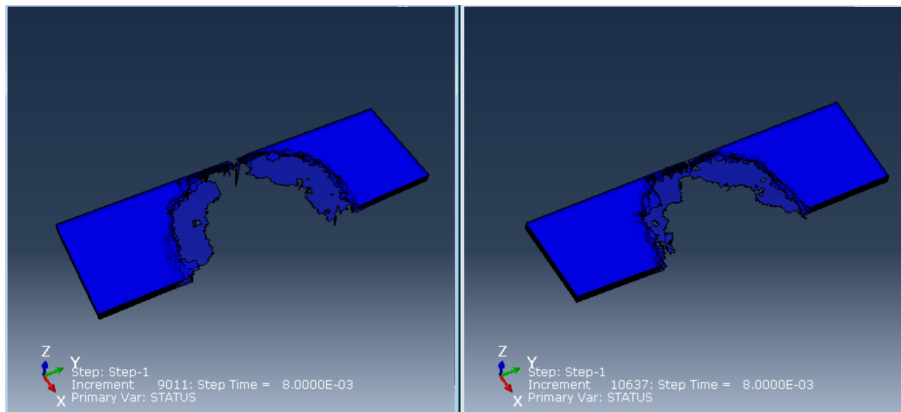


Figure 6.6: Delamination area central impact - 5J vs. 3J

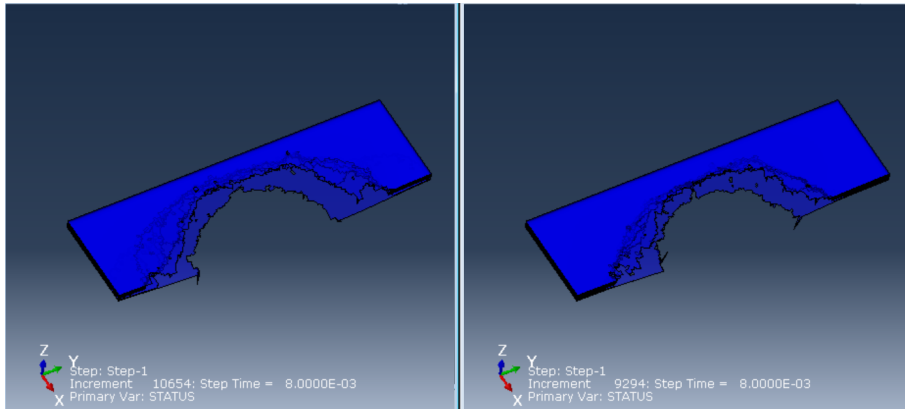


Figure 6.7: Delamination area near edge impact - 5J vs. 3J

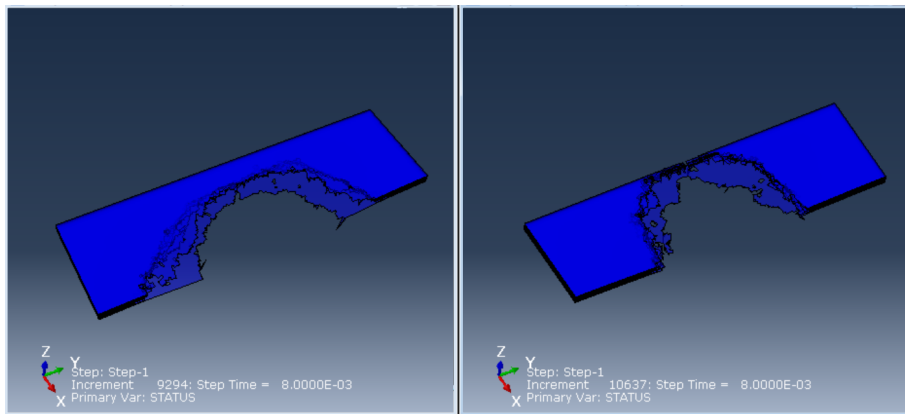


Figure 6.8: Delamination area 3J - near edge vs. central impact

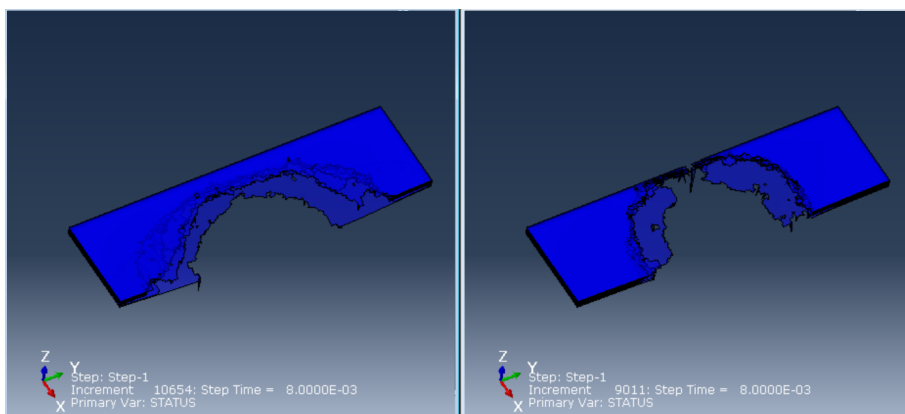


Figure 6.9: Delamination area 5J - near edge vs. central impact

An additional evaluation was carried out, relative to the effect of the impacting boundary conditions. As already mentioned in Chapter 3, the tested conditions of the central impact still had one edge of the specimen completely free, having the impacting point as the only difference between the near edge and central impact position. When modelling the case in which all four sides of the specimen are blocked, the obtained delamination would be as presented in Figure 6.10 and Figure 6.11.

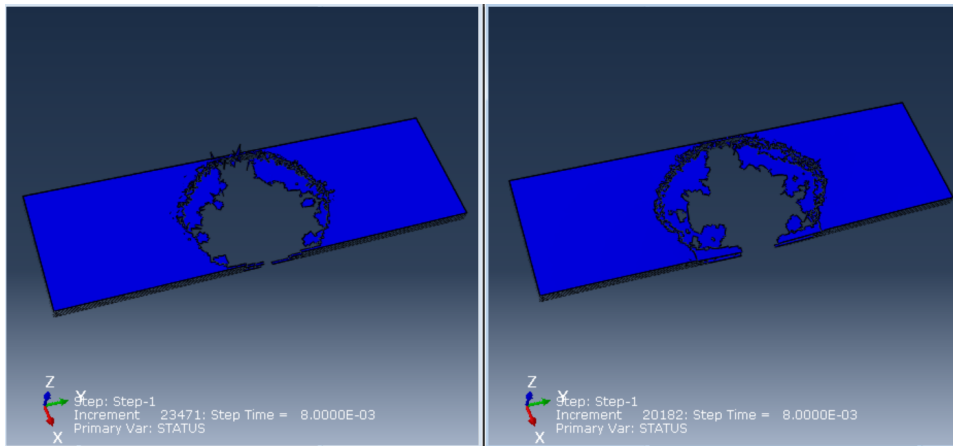


Figure 6.10: Delamination area 3J central impact - 4 sides vs. 3 sides blocked

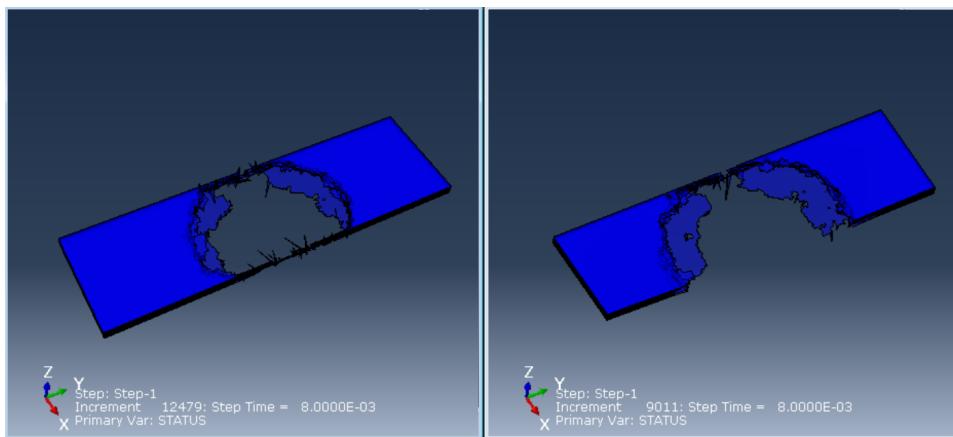


Figure 6.11: Delamination area 5J central impact - 4 sides vs. 3 sides blocked

6.3 Correlation of experimental and numerical delaminations

As already known from open literature and again confirmed with the current study, the near edge impacts introduce damage with greater extent inside the laminate. This was shown indirectly by experimental residual strength tests, with results illustrated in Chapter 3, Table 3.8 and directly by numerical analyses, where bigger delamination was introduced in the laminate for near edge impact cases, Table 6.3.

Energy [J]	Position	Delamination area [mm ²]	Residual strength reduction respect to pristine [%]	RSR/Delam
3	Near Edge	798	-11.36	0.014
3	Central	739	-10.40	0.014
5	Near Edge	1008	-31.31	0.031
5	Central	890	-14.24	0.016

Table 6.4: Comparison of numerical and experimental results

For the 3J impact case, it is possible to observe a linear correlation between the induced delaminations and experimentally measured residual strength, see ratio between the residual strength reduction and delaminated area in Table 6.8.

In Chapter 3 was already mentioned that the difference between residual strength data for near edge and central impact for 3J impact case is not as big as the one for the 5J impact case. It was argued that there should exist a certain threshold level under which the difference in residual strength between the two impact positions are not so evident and by increasing the impact energy, this difference becomes greater. This was exactly the case with the numerical analysis, in which the difference between the 3J impact cases (near edge and central) are minimal, while for the 5J impact cases this difference becomes more visible.

An additional explanation for this result could be that the experimental and numerical central impact specimens had unrealistic boundary conditions

(3 encastered edges only). In real life central impacts, in fact, the more realistic boundary condition for the structure is to be constrained on all four edges. For this reason, an additional numerical simulation was performed to simulate this case and the result can be seen in Table 6.5.

3J impact			
	Central 4 enc	Central 3 enc	Near Edge 3 enc
Average delamination, mm ²	682	739	798
Residual strength reduction, %	9.5*	10.4	11.4
*Calculated value			

Table 6.5: Comparison of numerical results, 3J impact case

Since no residual strength experimental data are available for this case, the decrease in residual static strength (-9.5% respect to pristine specimen) has been linearly extrapolated from the available results. The correlation between the delamination size and the static residual strength reduction for each impact type can be seen in Figure 6.12.

For the 5J impact case, the correlation between delamination and the reduction of residual static strength does not follow the same linear correlation observed in the 3J impact case, see Table 6.8. It is possible that the mere size of the delaminated area alone cannot account for the very high drop in residual strength, in respect to pristine specimen.

It can be argued that for this energy level, the delamination phenomenon itself is not able to absorb all the energy introduced by the impact, so additional mechanisms, like fiber breakage must have occurred. Similar behaviour has been observed with the first experimental campaign, in which it was shown that there is an almost linear correlation between applied impact energy, deformation and the acceleration of the impacting element, until certain threshold value after which this correlation is no longer valid, see Chapter 3.

An ulterior confirmation of this hypothesis comes from an additional numerical result. For energy level of 5J, the induced delamination in the case

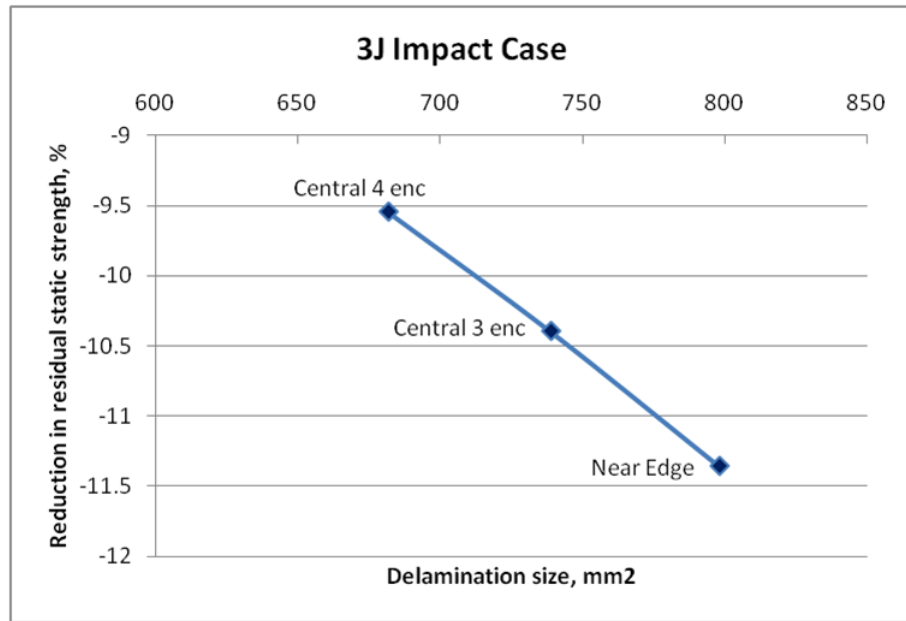


Figure 6.12: 3J - RSR reduction versus induced delamination size

of a central impact with a four edge encastre has been numerically evaluated, as well. The results are visible in Table 6.6.

	5J impact		
	Central 4 enc	Central 3 enc	Near Edge 3 enc
Average delamination, mm ²	793	890	1008
Residual strength reduction, %	11.3*	14.2	31.3
*Calculated value			

Table 6.6: Comparison of numerical results, 5J impact case

The numerically obtained delamination size is similar to the one of the 3J near edge case, for this reason a similar residual strength reduction has been assumed and calculated through the same linear slope (-11.3% in respect to the pristine specimen). The result of this study for the 5J cases is visible in Figure 6.13 where the non linearity is extremely clear and it is most likely due, as already mentioned, to other mechanism like fiber breakage.

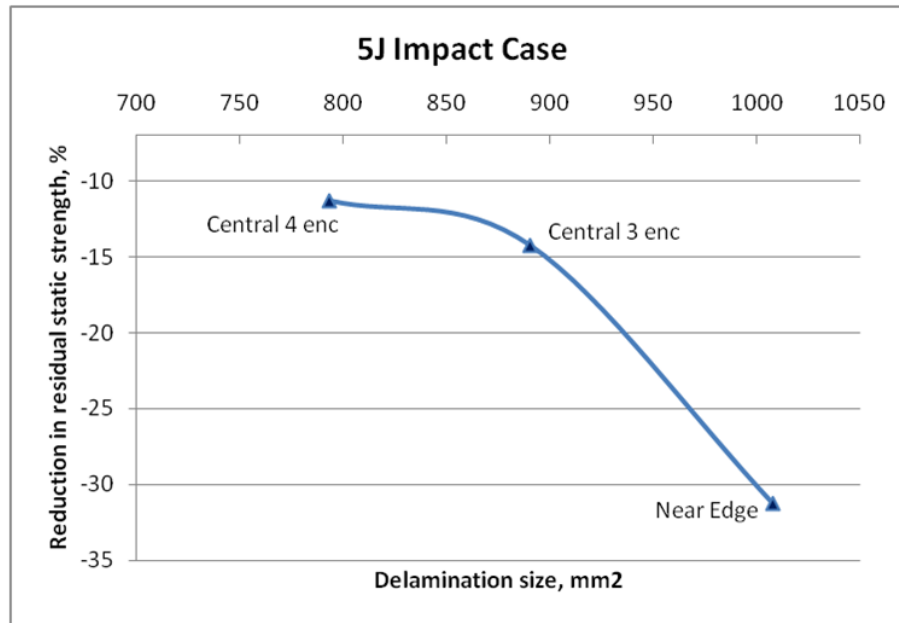


Figure 6.13: 5J - RSR reduction versus induced delamination size

6.3.1 Surface Indentation

The matrix plasticity governs the creation of external indentations on the surface of the impacted laminate but used Hashin model does not consider this phenomenon. For this reason a different approach needs to be developed when trying to evaluate numerically the dimension of the indentation. The working hypothesis is that the Hashin's matrix tension damage initiation criterion can be used as an indicator of the surface indentation size and of the delaminated area. What is shown in the following images is the extension of the area in which this criterion has been reached, and comparison between results obtained for different energy levels and boundary conditions is given.

The simple measurement of the indentation size for the impacted specimens with different impact energies and impact positions has shown the values given in Table 6.7.

Approximating the size of the area in which Hashin matrix tension damage initiation criterion has been met with the indented area in the experimentally tested specimens would indeed be the missing step which would validate the hypothesis in which the (invisible) delamination present in a laminate could

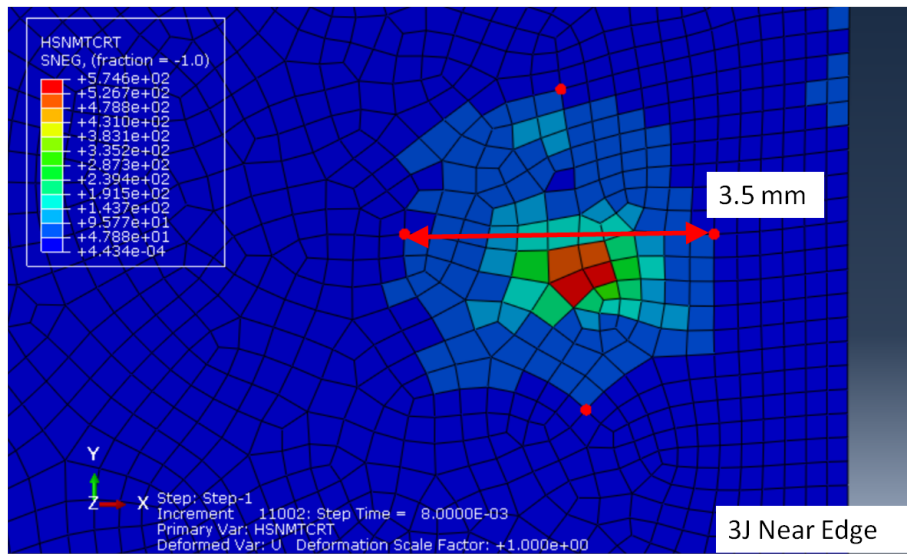


Figure 6.14: Matrix tension damage initiation criterion - 3J near edge impact

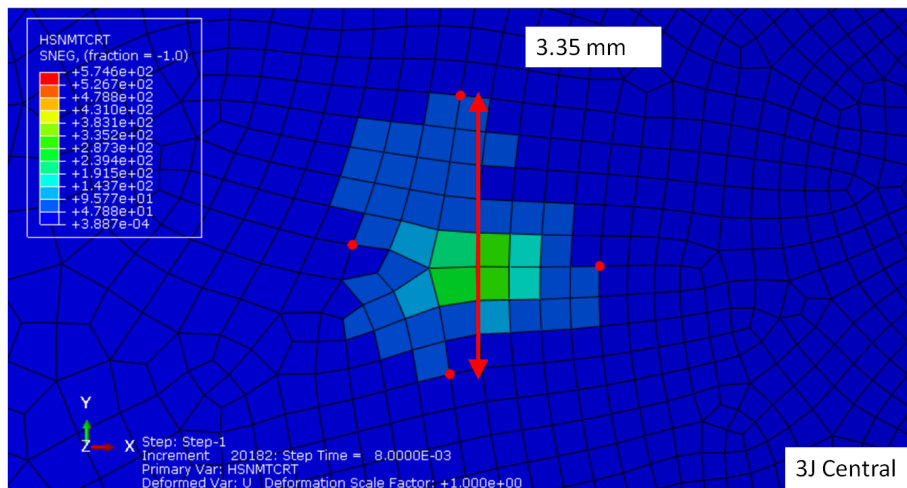


Figure 6.15: Matrix tension damage initiation criterion - 3J central impact

be assessed by inspection of the (visible) external indentation.

It is important to repeat that investigations on correlation of surface indentations and delamination size has already been reported in [56]. In current work, this assumptions has been extended to near-edge impact, with the Hashin matrix tensile damage initiation criterion used as an index of the surface indentation.

Considering already mentioned empirical match of this hypothesis, an

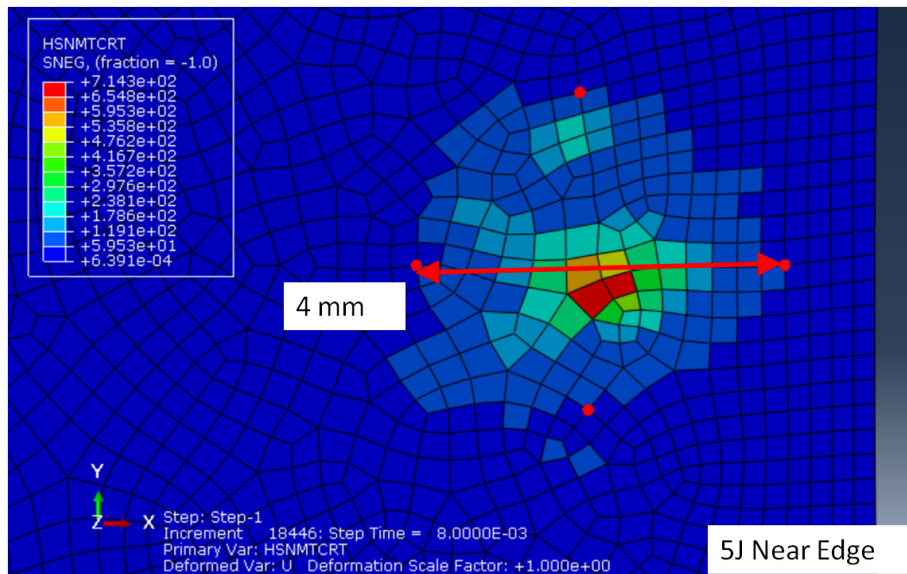


Figure 6.16: Matrix tension damage initiation criterion - 5J near edge impact

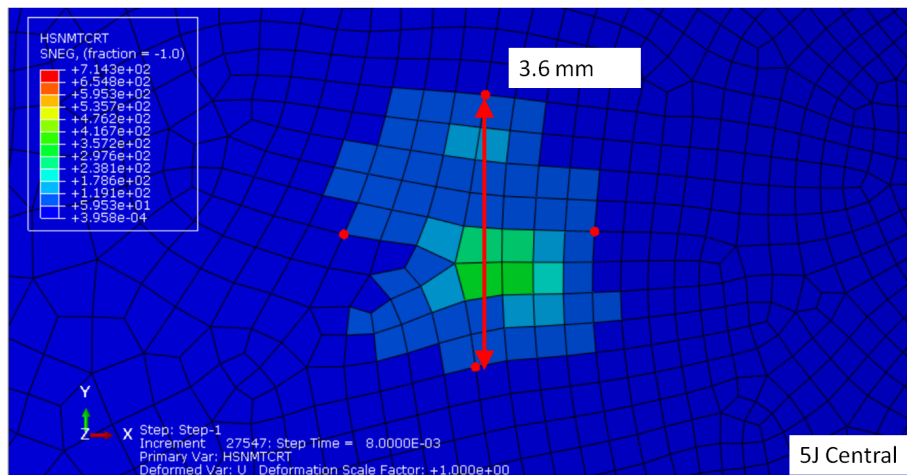


Figure 6.17: Matrix tension damage initiation criterion - 5J central impact

additional confirmation comes from [47], in which the surface indentation is assessed numerically using a matrix non-linear shear plasticity model. In this paper, numerical results relative to Hashin matrix tensile damage are presented together with the non-linear shear model and it can be observed that numerical predicted damage match closely, as illustrated in Figure 6.18, coming from [47].

In addition, it is important to consider that the non-linear shear plasticity

Energy [J]	Position	Size across dent [mm]
3	Near Edge	3.6
3	Central	3.4
5	Near Edge	4.3
5	Central	3.8

Table 6.7: Average experimental indentation size

model uses a failure criterion which is similar to Hashin’s criterion [53] (shear damage is a part of Hashin’s matrix tensile damage initiation), making the results of these two damage models comparable.

This is why it is possible to state that the proposed method of evaluating the extension of delamination based on the indentation size assessed from the Hashin’s matrix tensile damage initiation is based on a real physical similarity between the two phenomena (matrix shear plasticity and tensile damage) and not just on empirical observations. Table 6.8 shows the comparison between the measured indentation size on the impacted specimens and the size of the extension of the area of the Hashin’s matrix tensile damage initiation. Similarly to the data presented in Figure 6.18 from [47], the indentation size estimated using the matrix tensile damage initiation criterion is slightly smaller than the actual indentation size, and this observations would need to be taken into account when attempting to defining correlations between the delamination and surface indentation size.

Energy [J]	Position	Delamination area [mm ²]	Size across dent, measured [mm]	Size across “dent”, Abaqus [mm]
3	Near Edge	798	3.6	3.5
3	Central	739	3.4	3.35
5	Near Edge	1008	4.3	4.0
5	Central	890	3.8	3.6

Table 6.8: Comparison of numerical and experimental dent size measurement

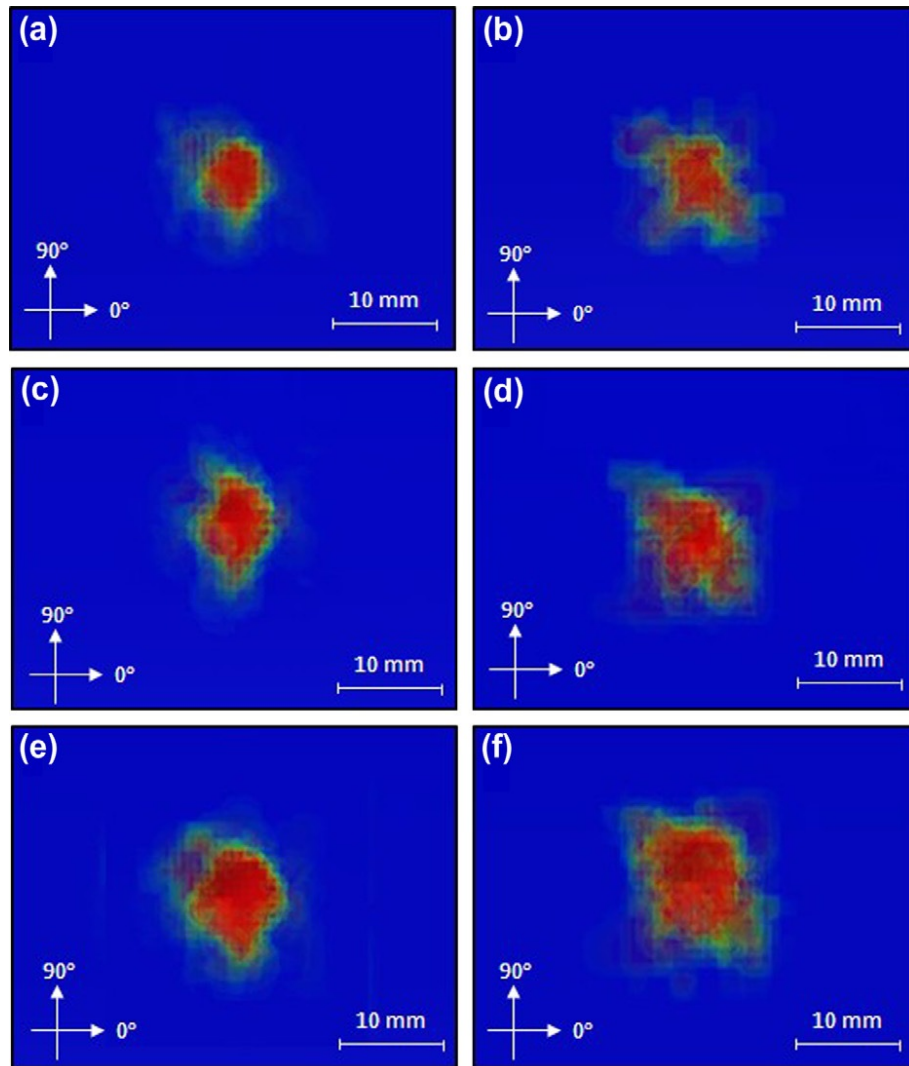


Figure 6.18: Numerically predicted damage from [47] in the form of matrix tensile failure, (a, c and e) and non-linear shear damage, (b, d and f) for different impact energies

6.3.2 Depth estimation of the surface indentation

As an independent attempt to assess the measured depth of the indentation using the experimental data and analytical models at hand, the Hertzian Contact Law was considered.

The Contact Law introduced by Hertz [58] was originally used for contact of two elastic isotropic spheres. When considering the contact between an

elastic sphere and an elastic flat plate, such as the case investigated in the current work, it qualifies as a special case in which the radius of one sphere is infinite.

Based on modified Hertz contact theory relative to impacts of hemispherical bodies to CFRP plates [59], [60], it is possible to analytically evaluate the depth of the surface indentation (dent) remaining after an impact event.

The relation between the contact force F and indentation x in this case is given by the equation:

$$F = Kx^{\frac{3}{2}}$$

For contact between isotropic and composite materials, K can be determined from the modified contact law [59], [60]:

$$K = \frac{4}{3}R^{\frac{1}{2}} \left(\frac{1 - \nu^2}{E} + \frac{1}{E_p} \right)^{-1}$$

In this equation, E and ν are the Young's modulus and Poisson's ratio of the impactor, E_p is the Young's modulus of the CFRP target in the direction normal to the contact plane (defined as E_{33} in Table 5.5).

The maximum measured acceleration for the case of 5J impact was 74.7g, Figure 3.16, and this information was used in order to calculate the maximum impact force, by knowing the impactor mass.

The input presented in Table 6.9 is used in order to assess analytically the indentation depth.

Description	Symbol	Value and unit
Impactor radius	R	3.5 mm
Young's Modulus impactor	E	210 [GPa]
Poisson's ratio impactor	ν	0.3 [-]
Young's Modulus of the CFRP target	E_p	7.8 [GPa]

Table 6.9: Input data for evaluation of indentation depth

After solving the equation using the defined input data, the obtained displacement relative to the indentation is then $x = 0.171$ mm (considering already calculated maximum contact force of 1331 N).

What is important to highlight is that this model is based on linear elastic assumptions, but it is still able to give a good orientation on the entity of the measured permanent damage (≈ 0.2 mm for the 5J near edge impact).

CHAPTER 7

Conclusions

Based on the results presented in this work, the following conclusions can be drawn:

- Satisfying Damage Tolerance requirements in composite aeronautical structures is a challenging task
- In order to be able to guarantee the damage tolerant capability of the composite structures, it is important to be able to detect damages introduced in the structure and to be able to predict what is their influence on the residual strength carrying capability
- Experimental and numerical comparison were made - either using the directly measured data or consulting the data in the open literature - and it was concluded that they match sufficiently to allow the use of numerical model to evaluate additional considerations
- After concluding that the numerical model is able to predict the delamination behaviour of composite structures after impact and to give an indication of the surface indentation, the next step was to correlate these two phenomena

- The possibility of correlation of surface indentation and introduced delamination after an impact has already been considered in the past in the open literature
- Quick and reliable evaluation of the damage extent needs to be carried out in aeronautical composite structures for in-service conditions. The contribution made by this work, to correlate the Hashin matrix tension damage initiation criterion with the indentation size, and finally with the delamination extension, could be applied for this scope
- Based on this proposed simplified methodology, it would be possible to predict a series of different scenarios, in which different fiber orientations, number of layers, boundary and loading conditions could be taken into account when assessing the after-impact behaviour of a composite structure
- It is however, important to highlight the limited extension of applicability of the current results - the correlation was done for hemispherical impacting element only, while in real-life applications, the impacting elements will have various shapes and sizes
- As a future development of this work, an experimental confirmation of the data extracted from the established correlations between Impact Energy - Dent size - Delamination size is recommended. A more extensive experimental campaign would serve to obtain the data for more ample impact events, thus confirming the applicability of the proposed approach

Bibliography

- [1] U.S. Department of Transportation, Federal Aviation Administration, Advisory Circular 20-107B, Composite Aircraft Structure, 2009. 2, 11, 14
- [2] EASA, AMC 20-29, 2010. 2, 11, 14
- [3] D. S. Li, Airbus Damage Tolerance Methodologies for Composite Structures, Proceedings of the 17th International Conference on Composite Materials, Edinburgh, United Kingdom, 2009. 2, 14
- [4] C. Breen, F.J. Guild, M.J. Pavier, Impact Damage to Thick Carbon Reinforced Plastic Composite Laminates, *J. Mater Sci.*, vol. 41, n. 20, p. 6718-6725, 2006. 2, 3
- [5] A.T. Rhead, D.Marchant, R.Butler, Compressive strength of composite laminates following free edge impact, *Composites: Part A*, vol. 41, n. 9 p. 1056-1065, 2010. 3, 4
- [6] A. Malhotra, F.J.Guild, M.J. Pavier, Edge impact to composite laminates: experiments and simulations, *J. Mater Sci.*, vol. 43, n. 20, p. 6661-6667, 2008. vi, 2, 3, 4, 5
- [7] B. Ostré, C. Bouvet, F. Lachaud, C.Minot, J. Aboissière, Edge impact damage scenario on stiffened composite structure, *J. Comp. Mater.* 0021998314537325, DOI: 10.1177/0021998314537325, 2014. 4

Bibliography

- [8] M. Guillaume, The Challenge of large Composite Transport Airplanes, Proceedings of the COMPTTEST - 5th International Conference on Composites Testing and Model Identification, Lausanne, Switzerland, 2011. 7
- [9] M. N. van Beijnen, M.J.L. van Tooren, Th. de Jong, A. Beukers, Damage Tolerance Aspects of a Full Composite Airplane Fuselage, Report LR-728, TU Delft, The Netherlands, 1993. 8
- [10] P.K. Mallick , Composites Engineering Handbook, CRC Press, 1997. 8
- [11] EASA. CS-25, Book 1, Airworthiness Code, Amendment 16, 2015. 11
- [12] U.S. Department of Transportation, Federal Aviation Administration, Advisory Circular 20-107, Composite Aircraft Structure, 1978. 11
- [13] U.S. Department of Transportation, Federal Aviation Administration, Advisory Circular 20-107A, Composite Aircraft Structure, 1984. 11
- [14] SAE International, Composite Materials Handbook 17, vol 3, 2012. 12
- [15] Damage Tolerance of Composite Structures in Aircraft Industry, http://www.carbon-composites.eu/sites/carbon-composites.eu/files/anhaenge/gruppen/12/08/30/02_ag_mpe_050310_schadenstoleranz_14062011.pdf vi, 15
- [16] R. Thévenin, Aircraft Composite Repair Management Forum, Madrid, Spain. <http://events.aviationweek.com/html/compos11/4-Roland%20Thevenin.pdf>, 2011. vi, 16
- [17] C. Fualdes, Composites @ Airbus - Damage Tolerance Methodology, FAA/EASA/Industry Workshop for Composite Damage Tolerance and Maintenance, Chicago, USA, 2006. vi, 16, 17
- [18] Materials & Structures testing for Korean Air, <http://www.appluslaboratories.com/en/> 17
- [19] A. Chiocchini, Valutazione del comportamento di materiali compositi sottoposti ad impatti "near-edge", <http://amslaurea.unibo.it/7972/>, 2014. 19

Bibliography

- [20] V. Agostinelli, Caratterizzazione sperimentale di materiali compositi soggetti ad impatto sul bordo, <http://amslaurea.unibo.it/8517/>, 2015. 19
- [21] D. Donati, Valutazione numerica del comportamento di materiali compositi sottoposti ad impatti "near edge", <http://amslaurea.unibo.it/9773/>, 2016. 19
- [22] T.W. Shyr, Y.H. Pan, Impact resistance and damage characteristics of composite laminates, *Composite Structures*, 62(2), pp. 193-203, 2003. vii, 23, 27
- [23] ASTM D7137/D7137M-12, Standard Test Method for Compressive Residual Strength Properties of Damaged Polymer Matrix Composite Plates, DOI: 10.1520/D7137-D7137M-12, 2012. 32
- [24] ASTM D6641/D6641M-16, Standard Test Method for Compressive Properties of Polymer Matrix Composite Materials Using a Combined Loading Compression (CLC) Test Fixture, DOI: 10.1520/D6641D6641M-16, 2016. 32, 38, 41
- [25] ASTM D3410/D3410M-16, Standard Test Method for Compressive Properties of Polymer Matrix Composite Materials with Unsupported Gage Section by Shear Loading, DOI: 10.1520/D3410D3410M-16, 2016. vii, 32, 36
- [26] M. Scafè, G. Raiteri, A. Brentari, R. Dlacic, E. Troiani, M.P. Falaschetti, E. Besseghini, *Frattura ed Integrità Strutturale*, vol. 29, p. 399-409, DOI: 10.3221/IGF-ESIS.29.35, 2014. 41
- [27] C. Kassapoglou, *Design and Analysis of Composite structures*, 2nd Edition, Wiley, 2013. 48
- [28] <https://web.fe.up.pt/~stpinho/teaching/feup/y0506/fcriteria.pdf>, accessed on 15 January 2017. 48, 49
- [29] F. Paris, *A Study of Failure Criteria of Fibrous Composite Materials*, NASA/CR-2001-210661, 2001. 48

Bibliography

- [30] C.T.Sun, B.J. Quinn, J. Tao, D.W. Oplinger, Comparative Evaluation of Failure Analysis Methods for Composite Laminates, NASA, DOT/FAA/AR-95/109, 1996. 49
- [31] M.J. Hinton, A.S Kaddour, P.D. Soden, Failure criteria in fibre reinforced polymer composites: The World-Wide Failure Exercise. Oxford, UK: Elsevier Science Ltd, 2004. 49
- [32] A.S. Kaddour and M.J. Hinton (Editors), Evaluation of Theories for Predicting Failure in Polymer Composite Laminates Under 3-D States of Stress: Part A of the Second World- Wide Failure Exercise (WWFE-II), Special issue of J. Composite Material, Vol. 46, No. 19-20, 2012.
- [33] A.S. Kaddour and M.J. Hinton (Editors), Evaluation of Theories for Predicting Failure in Polymer Composite Laminates Under 3-D States of Stress: Part B of the Second World- Wide Failure Exercise (WWFE-II), Special issue of J. Composite Materials, Vol. 47, No. 6-7, 2013.
- [34] A.S. Kaddour, M.J. Hinton, P.A. Smith, S. Li (Editors), Damage, Matrix cracking Criteria for Fibre Reinforced Polymer Composites, Part A of the 3rd World-Wide Failure Exercise, Special issue of J. Composite Materials, Vol. 47, No. 20-21, 2013. 49
- [35] S.T. Pinho, C.G. Dávila, P.P. Camanho, L. Iannucci, P. Robinson, Failure Models and Criteria for FRP Under In-Plane or Three-Dimensional Stress States Including Shear Non-Linearity, NASA/TM-2005-213530, 2005. 49
- [36] R. Hill, The Mathematical Theory of Plasticity, Oxford University Press, London, 1950. 49
- [37] S.W. Tsai, Strength Theories of Filamentary Structures, in Fundamental Aspects of Fiber Reinforced Plastic Composites, Wiley, New York, pp 311, 1968. viii, 48, 54, 55
- [38] S.W. Tsai, E.M. Wu, A General Theory of Strength for Anisotropic Materials, Journal of Composite Materials, 5, pp 58-80, 1971. 52

Bibliography

- [39] A. Puck, H. Schürmann, Failure Analysis of FRP Laminates by Means of Physically Based Phenomenological Models, *Composites Science and Technology*, 58, 1045-1067, 1998. 52
- [40] Z. Hashin, A. Rotem, A Fatigue Criterion for Fiber-Reinforced Materials, *Journal of Composite Materials*, vol. 7, pp. 448-464, 1973. 53
- [41] Z. Hashin, Failure Criteria for Unidirectional Fiber Composites, *Journal of Applied Mechanics*, vol. 47, pp. 329-334, 1980. viii, 53, 54
- [42] S. R. Swanson, A micro-mechanical model for in-situ compression strength of fiber composite laminates, *Transactions of the ASME. Series H, Journal of Engineering Materials and Technology* 114, 812, 1992. 53, 54, 76, 78
- [43] L.A. Carlsson, D.F. Adams, R. B. Pipes, Basic Experimental Characterization of Polymer Matrix Composite Materials, *Polymer Reviews*, 53 (2), pp. 277-302, 2013. 53, 54, 76, 78, 81
viii, 54, 55
viii, 55, 56
- [44] Abaqus 6.12, Analysis User's Manual, (24.3 Damage and failure for fiber-reinforced composites, 32.5 Cohesive Elements) viii, 57, 67, 68, 70, 72, 75, 80
- [45] A. Faggiani, B.G. Falzon, Predicting low-velocity impact damage on a stiffened composite panel, *Composites Part A*, vol. 41, pp. 737-749, 2010. 64
- [46] E. Greenhalgh, C. Meeks, A. Clarke, J. Thatcher, The effect of defects on the performance of post-buckled CFRP stringer-stiffened panels, *Composites Part A*, vol. 34 (7), pp. 623-633, 2003. 64
- [47] Y. Shi, T. Swait, C. Soutis, Modelling damage evolution in composite laminates subjected to low velocity impact, *Composite Structures*, vol. 94, pp. 2902-2913, 2012. ix, 59, 60, 64, 74, 81, 85, 88, 89, 99, 100, 101

- [48] A. Jumahat, C. Soutis, A. Hodzic, A graphical method predicting the compressive strength of toughened unidirectional composite laminates, *Appl Compos Mater*, vol. 18, pp. 6583, 2011. 64
- [49] C. Bouvet, B. Castanié, M. Bizeul, J.-J. Barrau, Low velocity impact modelling in laminate composite panels with discrete interface elements, *International Journal of Solids and Structures*, vol. 46, 28092821, 2009. 64
- [50] G. Alfano, M. A. Crisfield, Finite element interface models for the delamination analysis of laminated composites: mechanical and computational issues, *Int. J. Numer. Meth. Engng*, vol. 50, pp. 1701-1736, 2001. 65
- [51] P.P. Camanho, C. G. Dávila, Mixed-Mode Decohesion Finite Elements for the Simulation of Delamination in Composite Materials, NASA/TM-2002211737, pp. 137, 2002. 65, 74, 76
- [52] O. Allix, L. Blanchard, Mesomodeling of delamination: towards industrial applications, *Composites Science and Technology*, vol. 66, pp. 731744, 2006. 74
- [53] C. Bouvet, S. Rivallant, J.J. Barrau, Low velocity impact modeling in composite laminates capturing permanent indentation, *Composites Science and Technology*, vol. 72, pp. 19771988, 2012. 81, 100
- [54] M.L. Benzeggagh, M. Kenane, Measurement of Mixed-Mode Delamination Fracture Toughness of Unidirectional Glass/Epoxy Composites with Mixed-Mode Bending Apparatus, *Composites Science and Technology*, vol. 56, pp. 439-449, 1996. 72
- [55] A. Matzenmiller, J. Lubliner, R.L. Taylor, A Constitutive Model for Anisotropic Damage in Fiber-Composites, *Mechanics of Materials*, vol. 20, pp. 125152, 1995. 76
- [56] H. Kondo, Y. Aoki, K. Hiraoka, H. Hatta, Residual Indentation, Delamination Area and CAI Strength of CFRP Laminates under Low Velocity Impact, *Proceedings of the 16th International Conference on Composite Materials*, Tokyo,

Bibliography

- Japan. <http://www.iccm-central.org/Proceedings/ICCM16proceedings/contents/pdf/TueH/TuHA1-02gekondoh222812p.pdf> 84, 98
- [57] <https://tu-dresden.de/ing/maschinenwesen/ilr/lft/elamx2/elamx> 86
- [58] H. Hertz, ber die Berhrung fester elastischer Krper, Journal fr die reine und angewandte Mathematik, vol. 92, pp. 156-171, 1881. 101
- [59] C. T. Sun, S. H. Yang, Contact Law and Impact Response of Laminated Composites, NASA-CR-159884, 1980. 102
- [60] S.S. Pang, Y. Zhao, C. Yang, S.A. Griffin, Impact Response of Composite Laminates With a Hemispherical Indenter, Polimer Engineering and Science, vol. 31 (20), pp. 1461-1466, 1991. 102

Publications List

The author of this PhD thesis has used the following own works as its basis:

1. **V. Ristori**, E. Troiani, M.P. Falaschetti, G. Ivetic, Damage Tolerance in CFRP Structures - Numerical and Experimental Analysis of Low Energy Near Edge Impacts, Abstract accepted, 29th Symposium of the International Committee on Aeronautical Fatigue, Nagoya, Japan, June 2017.
2. **V. Ristori**, E. Troiani, M.P. Falaschetti, M. Montemurro, A. Baeten, G. Ivetic, G. Molinari, Damage Tolerance assessment of Edge impacts in CFRP structures, 28th Symposium of the International Committee on Aeronautical Fatigue, Helsinki, Finland, June 2015, ISBN: 978-9513874421
3. G. Ivetic, **V. Ristori**, Composites Fatigue - an Airbus Perspective, 1. Thementag "CFK in Maschinenbau", Augsburg, Germany, April 2015
4. G. Ivetic, **V. Ristori**, Composite Fatigue Airbus A350, 5. Technik-Kolloquium Augsburg-Regensburg, Augsburg, Germany, March 2015
5. **V. Ristori**, E. Troiani, G. Ivetic, Fatigue and Damage Tolerance in Composite Primary Aeronautical Structures, AIDAA 2013 - XXII Conference of Italian Aeronautic and Aerospace Association, Naples, Italy, September 2013